

¹ Muon tagging using a Match- χ^2 based Soft Muon
² Tagger in top quark analyses using data from the
³ ATLAS detector

⁴ Jacobo Ezequiel Blanco

⁵ Department of Physics
⁶ Royal Holloway, University of London



⁷ A thesis submitted to the University of London for the
⁸ Degree of Doctor of Philosophy

⁹ May 20, 2014

10

DECLARATION

11

12 I confirm that the work presented in this thesis is my own. Where information has been
13 derived from other sources, I confirm that this has been indicated in the document.

14 Jacobo Ezequiel Blanco

¹⁵

Abstract

¹⁶ This is an abstract

¹⁸ Preface

¹⁹ This thesis describes the calibration and utilization of a soft muon tagger for the purposes
²⁰ of

²¹ Contents

²²	1 Introduction and motivation	13
²³	2 The Standard Model of Particle Physics	14
²⁴	2.1 Quantum Electrodynamics	16
²⁵	2.2 Quantum Chromodynamics	18
²⁶	2.3 Weak Interactions	20
²⁷	2.3.1 Electroweak Unification and the Higgs mechanism	24
²⁸	3 Top-quark physics	27
²⁹	3.1 Top quark production	28
³⁰	3.2 Top quark decay modes	30
³¹	3.2.1 Motivations for selecting the ℓ +jets channel	33
³²	3.3 Latest developments in top physics	33
³³	4 The LHC and the ATLAS Detector	38
³⁴	4.1 The Large Hadron Collider	38
³⁵	4.1.1 Pileup	42
³⁶	4.2 The ATLAS detector	43
³⁷	4.2.1 Inner Detector	45
³⁸	4.2.2 Calorimetry	48
³⁹	4.2.3 Muon system	53
⁴⁰	4.2.4 Triggering and DAQ	53
⁴¹	4.3 Athena Control Framework and ROOT Framework	53

42	5 Calibration of the Soft Muon Tagger for 2012 ATLAS Data	55
43	5.0.1 Software, Collision Data and Simulated samples	56
44	5.1 Tag and Probe Selection	57
45	5.1.1 Trigger requirements	58
46	5.1.2 Selection Cuts	58
47	5.2 Invariant mass fitting	60
48	5.2.1 Uncertainty Measurement	62
49	5.3 Efficiencies	64
50	5.3.1 Isolation dependence	64
51	5.3.2 2011 Calibration	66
52	5.3.3 Efficiency Binning	66
53	5.3.4 Results	66
54	6 $t\bar{t}$ cross-section measurement in the $\ell+$jets channel using SMT	79
55	6.1 Soft Muon Tagger	79
56	6.2 Data and Monte Carlo samples	79
57	6.3 Object selection and event selection	79
58	6.4 Background estimation	80
59	6.4.1 Multijet in the electron channel	80
60	6.5 Systematic uncertainties	83
61	6.6 Results and conclusion	83
62	7 Muon Tagging in a boosted $t\bar{t}$ environment	84
63	7.1 Data samples	85
64	7.2 Boosted event topology	86
65	7.3 Signal muon selection	87
66	7.3.1 Muon selection	87
67	7.4 Efficiency definition	90
68	7.5 Results	93
69	7.5.1 Background	94
70	7.6 B-tagging potential in boosted events	95

⁷¹	8 Conclusions	98
⁷²	Appendices	99
⁷³	A List of triggers used in calibration	100
⁷⁴	B List of combined muon performance (MCP) cuts	103

List of Figures

76	2.1	The interaction vertex described by QED. One can obtain all possible vertex shapes by rotating this basic vertex and assigning the appropriate electric charge and making sure to conserve lepton number across the vertex.	16
77			
78	2.2	LO feynman diagrams of the process $e^+e^- \rightarrow e^+e^-$ allowed in QED. Additional vertices can be added to produce higher-order diagrams of the same process.	18
79			
80	2.3	Diagrams of the fundamental interaction vertices described by quantum chromodynamics. Shown are (a) Gluon emission from a quark, (b) Gluon emission from a gluon and finally (c) the four-gluon vertex.	20
81			
82	2.4	The neutral current and charged current vertices allowed via the weak force. Where f can be an e , μ or τ and ν_ℓ is the corresponding lepton neutrino of the same flavour. One can obtain all possible interaction vertices by rotating these basic vertices and assigning the appropriate electric charge and making sure to conserve lepton flavour across the vertex.	21
83			
84	2.5	Neutral current weak scattering vertex	21
85			
91	3.1	The leading order Feynman diagrams for $t\bar{t}$ production.	29
92			
93	3.2	Example Feynman diagrams for single top quark at leading order.	30
94			
95	3.3	Branching ratios of all possible $t\bar{t}$ decays. These probabilities are based on the branching-ratios of W decay shown in Table 3.2.	32
96			
95	3.4	Example event displays of (a) a dilepton $t\bar{t}$ event recorded by ATLAS and (b) a $\ell+$ jets event recorded at CMS.	33
96			

97	3.5 The feynman diagram of lepton plus jets channel including $t\bar{t}$ production via gluon fusion and decay with a leptonically decaying W^+ . Note that all other production mechanisms are also considered and the final state where the W^- is decayed leptonically is also taken into account.	34
101	3.6 A summary of all $t\bar{t}$ production cross section measurements performed at the LHC at $\sqrt{s} = 7$ TeV. Note the theory prediction shown as a dotted black line with its associated uncertainties as grey bands. The results shown above the black line have been statistically combined, producing the results labelled as combined . Many of these analyses have been superseded and the results are shown below the line. Other analyses performed but not included in the combination are also shown below the line.	35
109	3.7 A summary of the most precise $t\bar{t}$ production cross section measurements performed at the LHC at $\sqrt{s} = 7$ and 8 TeV and the Tevatron at $\sqrt{s} = 1.96$ TeV compared to the theoretical prediction. Note that the Tevatron results should be compared against the prediction for $p\bar{p}$ collisions while the LHC against the pp collision predictions.	36
114	4.1 The layout of CERN complex of experiments, note the main four LHC experiments located at different points around the ring.	39
116	4.2 Shown in (a) is the number of bunches colliding at the LHC and (b) the peak luminosity per unit time.	40
118	4.3 Distribution of the total integrated luminosity delivered by the LHC and the recorded by ATLAS for the 2011 and 2012 pp collision period. Note the \sqrt{s} changing from 7 TeV to 8 TeV between 2011 and 2012.	42
121	4.4 Number of interactions per bunch for the 2012 pp data-taking period at ATLAS per day. Note that both the average number of interactions for all bunches and the maximum number of interactions are shown.	43
124	4.5 An overview diagram of the ATLAS experiment. Shown are all detection and tracking systems and the toroid magnet which encompasses them. Note also the muon system on the outside of the detector.	44

127	4.6	caption	45
128	4.7	An event-display of an event as reconstructed by the ATLAS inner de-	
129		tector. Shown are the results of the vertexing algorithm where each line	
130		represents a track. the purple tracks have been fitted to a secondary vertex.	46
131	4.8	Plan-view of a quarter-section of the ATLAS ID showing the major de-	
132		tector elements with its active dimenstions and envelopes. Note also the	
133		η markers showing the maximum coverage up to $\eta = 2.5$	47
134	4.9	A drawing of in the transverse planeof the ATLAS ID showing all major	
135		detection elements in the barrel regions. Note the charged particle track	
136		marked in red traversing all the detector eleemnts.	47
137	4.10	A cut-away diagram of the ATLAS detector highlighting the calorimetry	
138		system. Shown are the ECal barrel and end-cap, the HCal barrel and	
139		end-cap and the FCal end-cap.	50
140	4.11	Cut-away diagram of the EM calorimeter barrel at $\eta = 0$. Shown are	
141		the three different layers with varying cell structures. The strip section is	
142		designed to enhance particle identification and position measurement in η .	51
143	4.12	Cut-away drawing of the ATLAS muon system.	53
144	4.13	Plan view of quarter-section of the ATLAS muon system.	54
145	5.1	The distribution of $\chi^2_{\text{match}}/N_{\text{dof}}$ for all muon probes for ATLAS collision	
146		data and prompt J/ψ Monte Carlo simulation.	61
147	5.2	A diagram of the various components of the fit procedure. The composite	
148		fit is shown along with the corresponding implied signal and background.	
149		The two variations of the background shape are also shown.	62
150	5.3	Invariant mass distributions of tag and probe pairs at a) probe level and	
151		at b) muon probe level in collision data. Note the various components of	
152		the fit as well as the variations on the background fits and the 3σ and 5σ	
153		integration windows used for systematics. Note the fit parameters and	
154		their respective uncertainties	65
155	5.4	χ^2_{DoF} efficiencies and scale factor with respect to $\sum E_T$	67
156	5.5	χ^2_{DoF} efficiencies and scale factor with respect to $\sum p_T$	68

157	5.6	χ^2_{DoF} efficiencies and scale factor with respect various isolation variables.	69
158	5.7	χ^2_{match} efficiencies and scale factor with respect to the (a) ϕ and (b) η	71
159	5.8	χ^2_{match} efficiencies and scale factor with respect to the transverse momentum of the muon probe	72
160	5.9	χ^2_{match} efficiencies and scale factors in the crack region of the detector for side (a) A and (b) C	73
161	5.10	χ^2_{match} efficiencies and scale factors in the barrel region of the detector for side (a) A and (b) C	74
162	5.11	χ^2_{match} efficiencies and scale factors in the transition region of the detector for side (a) A and (b) C	75
163	5.12	χ^2_{match} efficiencies and scale factors in the endcap region of the detector for side (a) A and (b) C	76
164	5.13	χ^2_{match} efficiencies and scale factors in the forward region of the detector for side (a) A and (b) C	77
165	5.14	χ^2_{match} efficiencies and scale factor with respect to impact parameter d_0 for muon probes with p_T in the range (a) 4-6 GeV, (b) 6-8 GeV and (c) 8-10 GeV. The measurement was carried out only on Period B of 2012 ATLAS collision data.	78
175	6.1	A diagram of the E_T -isolation phase space. Shown are the four regions as defined by the event selection.	81
176	7.1	This figure shows a simple diagram for the possible configuration of final-state objects in a (a) boosted and (b) non-boosted events. Note that in both cases a muon is embedded within the b -jet	86
177	7.2	The angular separation (ΔR) between the truth W muon and the corresponding b -quark for all examined Z' mass points.	87
178	7.3	The transverse momentum of the top/anti-top quarks in the event for all examined Z' mass points.	88
179	7.4	The angular separation (ΔR) between the b and \bar{b} in the event for all examined Z' mass points.	89

186	7.5	This figure shows the distribution of (a) transverse momentum and (b) 187 pseudo-rapidity of muons which pass the SMT selection, the (c) angular 188 separation between those muons and the nearest jet in th event and (d) 189 the χ^2_{match} used in the selection for all tested Z' mass points.	91
190	7.6	This figure shows the (a) transverse momentum and (b) pseudo-rapidity of 191 muons which pass the MI10 selection, the (c) angular separation between 192 those muons and the nearest jet in th event and (d) the cone size used in 193 the selection for all tested Z' mass points.	92
194	7.7	Structure of the efficiency measurement.	93
195	7.8	Efficiency of mini-isolation ($k_T = 10$) and χ^2_{match} muon tagger as a function 196 of the angular separation between the reconstructed muon and the nearest 197 reconstructed jet. Note the dip in the mini-isolation efficiency at low ΔR . 198 In the nominal analysis an overlap removal between the jet and the muon 199 is applied.	94
200	7.9	Efficiency of mini-isolation ($k_T = 10$) and χ^2_{match} muon tagger as a function 201 of the transverse momentum of the muon.	95

²⁰² List of Tables

²⁰³	2.1	A summary of all elementary particles described by the SM [1]. Note the various groupings and divisions including by spin, generation and particle type. Within the fermion sector the quarks are shown in yellow and the leptons are shown in green. These are grouped into three different generations traditionally denoted by roman numerals. The force mediators known as gauge bosons are shown in blue and finally the recently discovered Higgs boson with a spin of zero.	17
²¹⁰	2.2	A summary of the four fundamental forces ordered by relative strength. These are approximate relative strengths for the purpose of demonstrating the hierarchy of forces as a function of their strength. A more accurate determination of the interaction strength depends on the details of the interaction itself. Note however the order-of-magnitude differences in the relative strengths of these forces. Note that the graviton is the theoretical boson responsible for mediating gravitational interactions, it is not part of the SM.	17
²¹⁸	3.1	Summary of the predicted SM single top production [2] and top pair production [3] cross sections at the LHC for $\sqrt{s}=7$ and 8 TeV.	30
²²⁰	3.2	Branching ratios for the decay of W boson. Note that the “hadrons” refers to a possible combination of $q\bar{q}'$ where \bar{q}' denotes the antiquark of a flavour different to that of the first quark.	31

223	4.1	Design energy resolution of all ATLAS calorimeter components. The resolution is made of a sampling term ($1/\sqrt{E}$) associated with the choice of passive and active materials and construction of the layers and a constant term associated with the depth of the detector, cracks and dead material.	50
227	5.1	Pseudorapidity regions of the ATLAS detector	66
228	5.2	Data/MC Scale Factors for 2012 Data in all five regions of the detector as a function of p_T . The uncertainties include systematic and statistical components as described in Section 5.2.1	70
231	6.1	Multijet SMT event taggin-rate(in percent) in regions A) inverted- \cancel{E}_T , non-isolated, B) High- \cancel{E}_T , non-isolated and C) low- \cancel{E}_T , isolated.	82
233	6.2	Multijet estimates in the e+jets obtained by the jet-electron method. The uncertainties are combined statistical and systematics. A systematic uncertainty of 50% is used on the jet-electron pretag event yields [] in addition to e uncertainties obtained on $R_{\text{WGT}}^{\text{SMT}}$	83
237	7.1	Muon reconstruction selection used by Mini-Isolation and by Muon Tagging	90
238	7.2	Efficiency of selecting a muon by using the χ^2_{match} tagger against mini-isolation. Note that ‘MI10 + Overlap’ is the efficiency of applying both the mini-isolation cut and overlap removal.	94
241	7.3	Fake rate of χ^2_{match} tagger, mini-isolation and mini-isolation including overlap removal as measured using all Z' mass points.	96
243	7.4	Summary of the number of muons remaining after each selection cut and the efficiency.	97

²⁴⁵ **Chapter 1**

²⁴⁶ **Introduction and motivation**

²⁴⁷ **Chapter 2**

²⁴⁸ **The Standard Model of Particle
²⁴⁹ Physics**

²⁵⁰ Particle physics, or high-energy physics, is the study of the most fundamental constituents
²⁵¹ of matter and their interactions. The best current description of these interactions is
²⁵² known as The Standard Model of Particle Physics (SM); a group of theories that cover
²⁵³ all currently known particles and their interactions. The SM was developed through-out
²⁵⁴ the latter half of the 20th century and has seen tremendous success in predicting the
²⁵⁵ behaviour of our universe at the most fundamental level. The SM has stood the test
²⁵⁶ of time and rigorous examination by numerous experiments. Additionally many of its
²⁵⁷ parameters have been measured with tremendous precision e.g. the electron magnetic
²⁵⁸ moment g is known to 10^{-13} [4]. The last piece to be confirmed was the existence of the
²⁵⁹ Higgs boson, which in turn points to the existence of the so-called Higgs field. Evidence
²⁶⁰ of the elusive Higgs were observed by the ATLAS and CMS experiments at CERN [5, 6].
²⁶¹ Despite its tremendous success, the SM cannot account and explain for all observed
²⁶² phenomenon in the universe. Firstly, the theory requires many of its parameters to be
²⁶³ measured empirically. The theory does not a priori provide a value for these parameters
²⁶⁴ such as the number of particle generations. Additionally the theory does not describe the
²⁶⁵ most familiar of the forces, gravity. Furthermore, the SM does not provide a candidate for
²⁶⁶ dark matter, which is believed to make up more than 80% of the total energy density in
²⁶⁷ the universe. The asymmetry between matter and antimatter is also not fully explained

268 by the SM. As such there is a strong focus on developing theories which go beyond the
269 standard model (BSM) to provide an answer to these open questions. The discussion in
270 this chapter is largely based on [7] and [8].

271 The SM describes the nature of the interactions of the fundamental constituents
272 of our universe in terms of the three different fundamental forces: strong, weak and
273 electromagnetic each described by a specific theory. As mentioned before, the most
274 familiar of the forces, gravity, is not described by the SM. The SM classifies particles
275 into several categories depending on their properties and allowed interactions. Particles
276 which have a half-integer spins (e.g. $S = \frac{1}{2}, \frac{3}{2}, \dots$) are known as *fermions*, these are the
277 basic constituents of matter. Particles with integer spins (e.g. $S = 0, 1, \dots$) are known as
278 *bosons*, these mediate interactions between fermions and other bosons.

279 Fermions can be divided into two subgroups: quarks, which can interact via the
280 strong, weak and electromagnetic forces and leptons which can only interact by the
281 weak and electromagnetic forces. There are six known leptons: electron e , muon μ and
282 tau τ , which all have electric charge¹ $Q = 1$, and the corresponding electrically neutral
283 neutrino ν_e , ν_μ and ν_τ . Analogously, six quark *flavours* are known: u , c and t , with
284 electric charge $Q = +2/3$ and d , s and b , with electric charge $Q = -1/3$.

285 Quarks and leptons are divided into three generations, which differ only by the
286 mass and flavour of their constituent fermions, each generation being heavier than the
287 previous. A summary of all elementary particles described by the SM can be found in
288 Table 2.1.

289 For every matter fermion (f) there is an equivalent antimatter partner (\bar{f}) which
290 possesses the same characteristics as its matter companion but is opposite in electric
291 charge. Thus 12 matter particles are combined with 12 antimatter partners for a total
292 of 24 elementary particles which form all visible matter in the universe.

293 The interaction between fermions occur via the exchange of spin one particles known
294 as bosons. Each force is mediated by one or more bosons (Table 2.2). The strong force
295 is mediated by a set of massless bosons known as the gluons. The weak force is mediated
296 by a neutral massive boson known as the Z boson and a pair of charged massive bosons
297 known as the W bosons. Finally, the elecromagentic force is mediated by a massless

¹The electric charge is always state in units of elementary charge e

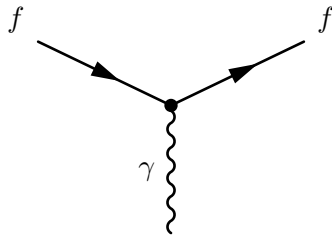


Figure 2.1: The interaction vertex described by QED. One can obtain all possible vertex shapes by rotating this basic vertex and assigning the appropriate electric charge and making sure to conserve lepton number across the vertex.

298 boson known as the photon. Note that each boson has an antimatter partner however
 299 some are indistinguishable from their matter partner. A summary of their properties is
 300 shown in Table 2.1.

301 Each fermion has a set of so-called quantum numbers which dictate the type of
 302 interactions that can occur. For example each lepton has a lepton number associated
 303 with it, electrons have an electron lepton number (L_e) of +1, while the positron has
 304 $L_e = -1$. Muons and taus have their own respective lepton number (L_μ and L_τ). Each
 305 neutrino has lepton number $L_f = 1$ and their anti-matter counterpart have $L_f = -1$.
 306 Each of these lepton numbers is conserved separately across interaction vertices. Another
 307 example of a quantum number is baryon number (B), each quark has $B = \frac{1}{3}$ and anti-
 308 quarks have $B = -\frac{1}{3}$.

309 2.1 Quantum Electrodynamics

310 The interaction of particles via the electromagnetic force is described by Quantum Elec-
 311 trodynamics or QED. These interactions are mediated by the massless neutral boson
 312 known as the photon and the strength of the interaction is characterized by the fine-
 313 structure constant α . All electrically charged fermions are allowed to interact, since the
 314 photon itself is not charged, no self-interaction is allowed within QED. Figure 2.1 shows
 315 the single vertex described by QED, where two fermions interact via a photon. Note
 316 that the electric charge is conserved across the vertex, so for example $\gamma \rightarrow e^+e^+$ is not
 317 allowed within QED.

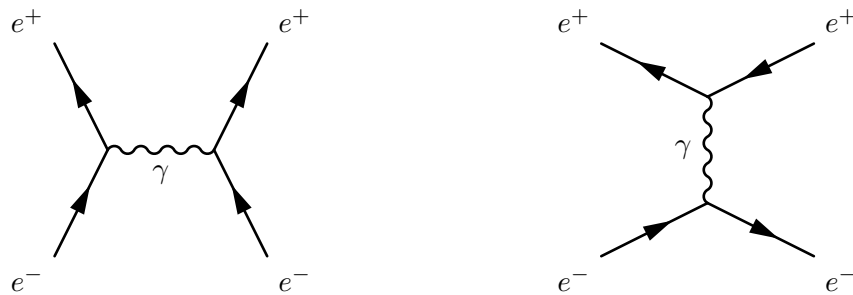
318 By combining different forms of this vertex one can build every possible QED in-
 319 teraction. For example an e^+e^- pair can annihilate to create energy in the form of a

Fermions ($s = \frac{1}{2}$)			Bosons ($s = 0$)	Higgs ($s = 1$)
	I	II	III	
Quarks	$+\frac{2}{3}$ u Up	$+\frac{2}{3}$ c Charm	$+\frac{2}{3}$ t Top	0 γ Photon (EM)
	$-\frac{1}{3}$ d Down	$-\frac{1}{3}$ s Strange	$-\frac{1}{3}$ b Bottom	± 1 W^\pm W boson (Weak)
	-1 e Electron	-1 μ Muon	-1 τ Tau	0 Z Z boson (Weak)
	0 ν_e Electron Neutrino	0 ν_μ Muon Neutrino	0 ν_τ Tau Neutrino	0 g Gluon (Strong)
				symbol
				name (force)

Table 2.1: A summary of all elementary particles described by the SM [1]. Note the various groupings and divisions including by spin, generation and particle type. Within the fermion sector the quarks are shown in yellow and the leptons are shown in green. These are grouped into three different generations traditionally denoted by roman numerals. The force mediators known as gauge bosons are shown in blue and finally the recently discovered Higgs boson with a spin of zero.

Name	Relative Strength	Boson
Strong	10^{38}	Gluons
Electromagnetic	10^{36}	Photon
Weak	10^{25}	W^\pm and Z^0
Gravity	1	Graviton*

Table 2.2: A summary of the four fundamental forces ordered by relative strength. These are approximate relative strengths for the purpose of demonstrating the hierarchy of forces as a function of their strength. A more accurate determination of the interaction strength depends on the details of the interaction itself. Note however the order-of-magnitude differences in the relative strengths of these forces. Note that the graviton is the theoretical boson responsible for mediating gravitational interactions, it is not part of the SM.



(a) Electron-Positron pair annihilation mediated by a photon.
(b) Electron-Positron pair scattering via the emission of a photon.

Figure 2.2: LO Feynman diagrams of the process $e^+e^- \rightarrow e^+e^-$ allowed in QED. Additional vertices can be added to produce higher-order diagrams of the same process.

320 photon as shown in Fig. 2.2a and then subsequently decay into an additional e^+e^- pair.
321 Note this is the simplest form of this diagram or Leading Order (LO) diagram for this
322 interaction. Electrons can scatter by emitting a photon which is then absorbed by a
323 positron as shown in Fig. 2.2b this process is known as Bhabha scattering.

324 2.2 Quantum Chromodynamics

325 Interactions via the strong force are described in the theory of Quantum Chromodynam-
326 ics or QCD. These interactions are mediated by a set of massless neutral bosons known
327 as gluons. QCD introduces the concept of colour, which similarly to electrical charge,
328 determines the possible interactions that can occur via the strong force. Colour can take
329 three states: red (antired), blue (antiblue), green (antigreen):

For example both quarks and gluons possess colour and as a result gluons, unlike photons, can self-interact in a three gluon vertex (Figure 2.3b) or a four gluon vertex (Figure 2.3c). As with electrical charge, colour-charge must also be conserved. Thus in the scattering process $q \rightarrow q + g$ shown in Figure 2.3a the flavour of the quark may not change but the colour-charge does and the gluon carries away the difference in colour. Thus each gluon has two color charges associated with it. Naively one would expect nine different types of gluon that participate in interaction, owing to the nine possible combinations of colour and anticolour, however the SU(3) symmetry on which QCD is

based results in a colour octet:

$$\begin{array}{ll}
 (r\bar{b} + b\bar{r})/\sqrt{2} & -i(r\bar{g} - g\bar{r})/\sqrt{2} \\
 -i(r\bar{b} - b\bar{r})/\sqrt{2} & (b\bar{g} + g\bar{b})/\sqrt{2} \\
 (r\bar{r} + b\bar{b})/\sqrt{2} & -i(b\bar{g} - g\bar{b})/\sqrt{2} \\
 (r\bar{g} + g\bar{r})/\sqrt{2} & (r\bar{r} + b\bar{b} - 2g\bar{g})/\sqrt{6}
 \end{array}$$

³³⁰ and a “colour singlet”:

$$(r\bar{r} + g\bar{g} + b\bar{b})/\sqrt{3} \quad (2.1)$$

³³¹ which is overall colourless.

³³² There are then eight different gluons that can participate in QCD interactions each
³³³ with a different colour-charge combination. Additionally there is a ninth combination
³³⁴ which is overall colorless so it cannot take part in interactions.

³³⁵ In an analogous fashion to screening which occurs with electric charges, quark-
³³⁶ antiquark pairs act like dipoles which screen the true colour charge of the central quark.
³³⁷ However since gluons also carry colour, they cause the opposite effect (anti-screening) to
³³⁸ amplify and change the observed colour of the quark. Which effect wins out depends on
³³⁹ the number of colours in the theory and the number of quark flavours. As it is with three
³⁴⁰ colour states and six different quark flavours, anti-screening is the overall dominant ef-
³⁴¹ fect. As a result the colour potential decreases with distance and quarks experience very
³⁴² little potential when very near to each other. This effect is known as asymptotic freedom
³⁴³ and results in quarks only existing within colorless bound states known as *hadrons*.

³⁴⁴ Hadrons can be divided into two categories: *mesons*, which contain a quark and an
³⁴⁵ antiquark ($q\bar{q}$); and *baryons* which are made of three quarks (or antiquarks) each with
³⁴⁶ a different (anti)colour-charge to result in a colourless composite particle. Common
³⁴⁷ examples of baryons are protons (uud) and neutrons (udd) which are the building blocks
³⁴⁸ of atomic nuclei. While π^0 ($u\bar{u}/d\bar{d}$) is a commonly produced meson in hadron colliders.
³⁴⁹ Note that due to the quark configuration, baryons have baryon number $B = +1$ while
³⁵⁰ mesons have $B = 0$.

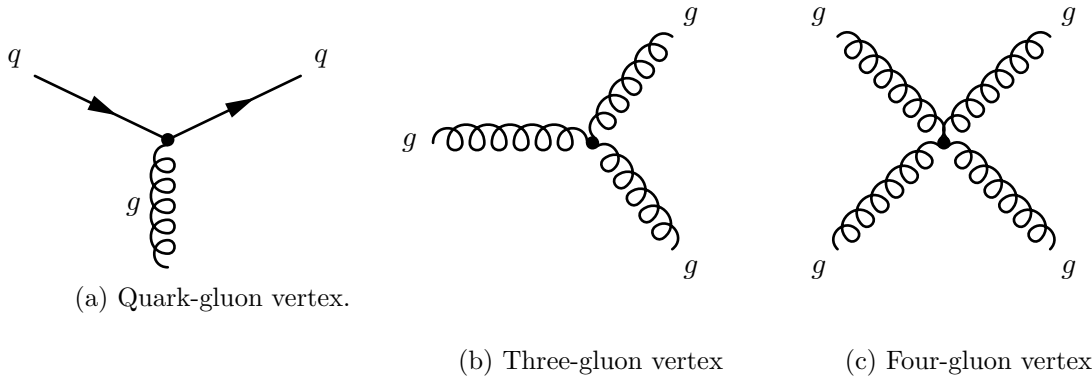


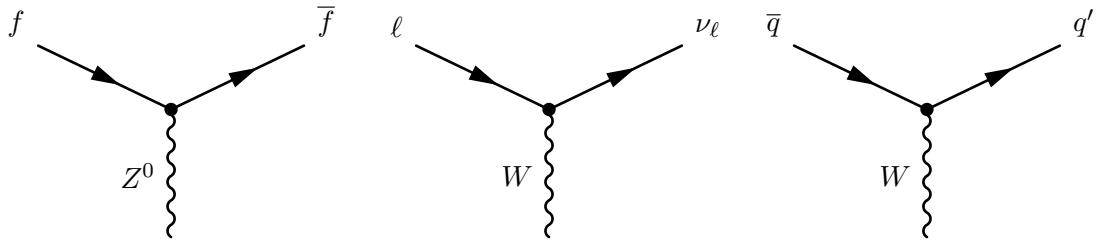
Figure 2.3: Diagrams of the fundamental interaction vertices described by quantum chromodynamics. Shown are (a) Gluon emission from a quark, (b) Gluon emission from a gluon and finally (c) the four-gluon vertex.

351 2.3 Weak Interactions

The final type of interaction involves the so-called weak force. The weak force is responsible for β^- decay ($n \rightarrow p + e^- + \bar{\nu}_e$) and β^+ decay. Interactions via the weak force are mediated by a single neutral massive boson and two charged massive bosons. Since the bosons responsible for weak interactions are massive, the range of interaction is very short, unlike electromagnetic interactions via a massless photon.

All fermions can take part in interactions via the weak force. Let us consider weak interactions involving only leptons. The weak neutral vertex is very similar to the basic vertex seen in QED (2.1) A valid interaction via the weak force is then formed by combining these simple vertices (Figure 2.4) while taking care to conserve electric charge and lepton flavour. An example of a leptonic weak interaction is muon decay ($\mu \rightarrow \nu_\mu W^- \rightarrow \nu_\mu e^- \bar{\nu}_e$) shown in Figure 2.5.

Let us consider weak interactions involving quarks. The neutral vertex is similar to that of the leptonic version, a quark can emit a Z boson or a Z can decay to a quark-antiquark pair. The charged current then changes the flavour of an up-type quark into a down-type quark (or vice-versa) with a W boson of the appropriate charge (Figure 2.4c). Weak interactions can also change the flavour of a quark across generations. A well-known example of such an interaction is Kaon decay ($K^+ \rightarrow \mu^+ \nu_\mu$). In order to account for this interaction and preserve the universality of weak interactions, Nicola Cabibbo postulated [9] that the states that couple to the charged current are really a mixture of



(a) Neutral current weak vertex
(b) Charged current vertex involving leptons
(c) Charged current vertex involving quarks

Figure 2.4: The neutral current and charged current vertices allowed via the weak force. Where f can be an e , μ or τ and ν_ℓ is the corresponding lepton neutrino of the same flavour. One can obtain all possible interaction vertices by rotating these basic vertices and assigning the appropriate electric charge and making sure to conserve lepton flavour across the vertex.

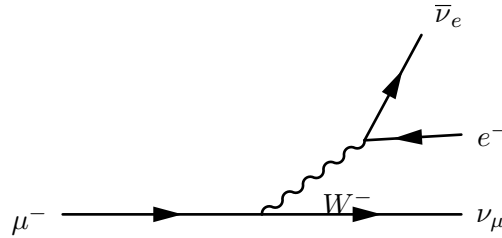


Figure 2.5: Neutral current weak scattering vertex

³⁷¹ 'rotated' quark states:

$$\begin{pmatrix} u \\ d' \end{pmatrix} \begin{pmatrix} c \\ s' \end{pmatrix} \quad (2.2)$$

³⁷² where

$$d' = d \cos \theta_c + s \sin \theta_c \quad (2.3a)$$

³⁷³

$$s' = -d \sin \theta_c + s \cos \theta_c \quad (2.3b)$$

³⁷⁴ This introduces an arbitrary parameter into the theory known as the quark mixing angle or the Cabibbo angle θ_c . The introduction of quark mixing has the effect of attenuating the interaction strength at vertices involving multiple quark generations. ³⁷⁷ Interactions which cross one generation are said to be Cabibbo Suppressed while those ³⁷⁸ that cross two generations are Doubly Cabibbo suppressed.

³⁷⁹ Taking into account the three quark generations, quark mixing can be expressed ³⁸⁰ in matrix notation as shown in Equation 2.4. This unitary matrix is known as the ³⁸¹ Cabibbo-Kobayashi-Maskawa Matrix (CKM Matrix) after Cabibbo which initially pos-

³⁸² tulated quark mixing and Makoto Kobayashi and Toshihide Maskawa who later added
³⁸³ an additional generation, containing the top and bottom quarks, to the matrix [10].

$$\begin{pmatrix} d' \\ s' \\ b' \end{pmatrix} = V_{CKM} \begin{pmatrix} d \\ s \\ b \end{pmatrix} = \begin{pmatrix} V_{ud} & V_{us} & V_{ub} \\ V_{cd} & V_{cs} & V_{cb} \\ V_{td} & V_{ts} & V_{tb} \end{pmatrix} \begin{pmatrix} d \\ s \\ b \end{pmatrix} \quad (2.4)$$

³⁸⁴ Several parameterizations of the CKM matrix exist, the “standard” parametrization
³⁸⁵ uses angles θ_{12} , θ_{23} , θ_{13} and a phase δ_{13} :

$$V_{CKM} = \begin{pmatrix} c_{12}c_{13} & s_{12}c_{13} & s_{13}\exp(-i\delta) \\ -s_{12}c_{23} - c_{12}s_{23}s_{13}\exp(i\delta) & c_{12}c_{23} - s_{12}s_{23}s_{13}\exp(i\delta) & s_{23}c_{13} \\ s_{12}s_{23} - c_{12}c_{23}s_{13}\exp(i\delta) & -c_{12}s_{23} - s_{12}c_{23}s_{13}\exp(i\delta) & c_{23}c_{13} \end{pmatrix} \quad (2.5)$$

³⁸⁶ where $c_{ij} = \cos \theta_{ij}$ and $s_{ij} = \sin \theta_{ij}$ for $i=1,2,3$. This parametrization has the advantage
³⁸⁷ that each angle θ_{ij} relates to a specific transition from one generation to the other. If
³⁸⁸ $\theta_{13} = \theta_{23} = 0$ the third generation is not coupled to the other two and the matrix reduces
³⁸⁹ to the original matrix postulated by Cabibbo. Note that θ_{12} is the Cabibbo angle, θ_c ,
³⁹⁰ described earlier.

³⁹¹ Another parameterization due to Wolfenstein [11] expresses all elements in terms of
³⁹² the Cabibbo angle by defining $\lambda \equiv s_{12} = \sin \theta_{12}$ and then expressing the other elements
³⁹³ in terms of powers of λ :

$$V_{CKM} \approx \begin{pmatrix} 1 - \lambda^2/2 & \lambda & A\lambda^3(\rho - i\eta) \\ -\lambda & 1 - \lambda^2/2 & A\lambda^2 \\ A\lambda^3(1 - \rho - i\eta) & -A\lambda^2 & 1 \end{pmatrix} \quad (2.6)$$

³⁹⁴ where A , ρ and η are all real numbers intended to express the order of magnitude
³⁹⁵ differences between s_{12} and the other elements in the matrix. Of course, all the elements
³⁹⁶ should be the same irrespective of which parametrization is used.

³⁹⁷ The elements of the CKM matrix have been measured and the latest accepted re-
³⁹⁸ sults are summarized in 2.8 [1]. The interaction strength is then proportional to $|V_{ij}|^2$.
³⁹⁹ Including all three generations the sum of all possible transitions from a given quark, q ,

400 is unity:

$$\sum |V_{qi}|^2 = 1 \quad (2.7)$$

401 Note that the term V_{tb} is approximately unity and by far dominates over the other
402 V_{tj} terms. This means that the top-quark transitions almost exclusively into a b -quark
403 ($t \rightarrow Wb$) with transitions $t \rightarrow Ws$ and $t \rightarrow Wd$ being exceedingly rare. The soft muon
404 tagger which is the focus of this thesis relies on weak semileptonic decays of b -quarks.
405 From 2.8 one can see that the transition $b \rightarrow c$ dominates over $b \rightarrow u$. Additionally the
406 focus of this theses is on semileptonic $t\bar{t}$ events, where one of the W bosons in the event
407 decays to quarks as per the magnitude of V_{ij} .

$$V_{CKM} = \begin{pmatrix} 0.97427 \pm 0.00015 & 0.22534 \pm 0.00065 & 0.00351^{+0.00015}_{-0.00014} \\ 0.22520 \pm 0.00065 & 0.97344 \pm 0.00016 & 0.0412^{+0.0011}_{-0.0005} \\ 0.00867^{+0.00029}_{-0.00031} & 0.0404^{+0.0011}_{-0.0005} & 0.999146^{+0.000021}_{-0.000046} \end{pmatrix} \quad (2.8)$$

408 An additional unique feature of weak interactions is that the charge conjugation-
409 parity (CP) symmetry is violated. The operator C denotes the change of a particle
410 by its antiparticle partner and P denotes a reversal of helicity (the projection of spin
411 onto the momentum of a particle). A clear violation of C and P was observed in the
412 radioactive decay of Cobalt-60, where the resulting electrons were preferentially emitted
413 in the opposite direction of the nuclear spin of the Cobalt. Thus weak currents only
414 couple to left-handed neutrinos (or right-handed antineutrinos) this is then a violation
415 of parity. Additionally charge symmetry is also violated since a left-handed neutrino is
416 preferentially picked over a left-handed antineutrino. Finally in 1964 CP violation was
417 observed in the decay of neutral kaon.

418 Thus the probability of $\bar{a} \rightarrow \bar{b}$ is not equal to that of $a \rightarrow b$. The existence of
419 CP violation has interesting consequences for the formation of the early universe. The
420 preferential production of matter over antimatter in CP violating interactions would
421 shift the balance in favour of matter resulting in a universe similar to our own. Finally
422 as with QCD, weak interactions couple weak bosons to each other. Thus the vertex

⁴²³ $Z \rightarrow W^-W^+$ is allowed via the weak force.

⁴²⁴ 2.3.1 Electroweak Unification and the Higgs mechanism

⁴²⁵ The unification of the electromagnetic and weak theories was first proposed by Glashow
⁴²⁶ and later developed by Weinberg and Salam into the electroweak theory. The theory
⁴²⁷ postulates that while at low energies the two forces are to be treated separately, at higher
⁴²⁸ the two can be seen as a single force. Thus the two forces are different manifestation of the
⁴²⁹ same “electroweak” interaction. There were several stumbling blocks to the unification
⁴³⁰ of the forces. Firstly, the boson which drives the electromagnetic interaction, the photon,
⁴³¹ is massless while the weak bosons are both massive. Evidence for the massive nature of
⁴³² these bosons has been established by experimental results from at CERN.

⁴³³ Thus the symmetry of the theory must be spontaneously broken in some way. A mech-
⁴³⁴ anism for ElectroWeak Symmetry Breaking (EWSB) was postulated by Higgs, Brout,
⁴³⁵ Englert and others which introduces masses to the weak bosons and posits the existence
⁴³⁶ of an additional scalar (spin $S = 0$) boson known as the Higgs boson.

⁴³⁷ Gauge Theories

⁴³⁸ Gauge invariance is one of the underlying invariances which underpins the Standard
⁴³⁹ Model. Given the so-called Dirac lagrangian²

$$\mathcal{L} = i\hbar c\bar{\psi}\gamma^\mu\partial_\mu\psi - mc^2\bar{\psi}\psi \quad (2.9)$$

⁴⁴⁰ which describes a free particle of spin- $\frac{1}{2}$ with mass m . Note that it is invariant under
⁴⁴¹ the transformation

$$\psi \rightarrow e^{i\theta}\psi, \text{ where } \theta \text{ is a real number} \quad (2.10)$$

⁴⁴² since the adjoint $\bar{\psi} \rightarrow e^{-i\theta}\bar{\psi}$ and the two terms cancel out. This is known as a (*global*)
⁴⁴³ *gauge transformation*. This is essentially a phase transformation which is constant every-
⁴⁴⁴ where. Meaning the phase change is the same in all points of space-time. A “local” gauge

²A Lagrangian is a mathematical function that describes the underlying dynamics of a system as a function of time and space coordinates (x^μ) and their time derivatives.

445 transformation occurs when the phase is different for different points in space-time:

$$\psi \rightarrow e^{i\theta(x)}\psi \quad (2.11)$$

446 Note that the Dirac lagrangian (Equation 2.9) is then not invariant under a local
 447 gauge transformation since extra terms are created by the derivative. This then implies
 448 that the underlying physics of such a theory depends ones position in space-time. Thus
 449 local gauge invariance must be imposed. In the case of the Dirac lagrangian, this is
 450 done by introducing additional terms to the Dirac lagrangian which will cancel the extra
 451 terms introduced by the local gauge transformation. As it turns out this results in the
 452 introduction of a new massless vector field that couples to ψ .

453 The new lagrangian then describes a spin- $\frac{1}{2}$ particle with mass m that interacts with
 454 a free massless field. This new field can be indentified as the electromagnetic field and
 455 the spin- $\frac{1}{2}$ particles are electrons and positrons. Thus the resulting lagrangian describes
 456 all interactions that form part of quantum electrodynamics.

457 A similar procedure can be applied to the color quark model and obtain a description
 458 of all QCD interactions. However requiring that the weak theory be a gauge theory
 459 (invariant under local gauge transformation) encounters a problem since the weak bosons
 460 are known to be massive. There must be some mechanism via which the W^\pm and Z^0
 461 obtain mass.

462 The Higgs mechanism posits the existence of a complex scalar field doublet that
 463 when introduced into the electroweak Lagrangian results in the weak fields acquiring a
 464 mass term. In other words the W^\pm and Z^0 interact with the Higgs field and obtain
 465 a mass. An additional consequence of introducing the Higgs field is the inclusion of
 466 a scalar boson particle, the the so-called “Higgs boson”. Finally the Higgs field also
 467 couples to fermions via the Yukawa coupling generating gauge invariant mass terms for
 468 the fermions as well.³.

469 The SM Lagrangian in its current form including the Higgs potential is shown in
 470 Equation 2.12. This expression describes all possible particle interactions that form part
 471 of the SM, of particular interest are the fermion mass term which couples the fermion

³For a more complete description of the mathematical procedure see [8].

⁴⁷² field (ψ) to the scalar Higgs field (ϕ) and the Higgs kinetic and potential terms.

$$\begin{aligned} \mathcal{L} = & -\underbrace{\frac{1}{4}W_{\mu\nu}^a W^{\mu\nu a}}_{\text{Weak Field}} - \underbrace{\frac{1}{4}B_{\mu\nu} B^{\mu\nu}}_{\text{EM Field}} - \underbrace{\frac{1}{4}G_{\mu\nu}^a G^{\mu\nu a}}_{\text{Strong Field}} \\ & + \underbrace{\bar{\psi} \not{D}_\mu \psi}_{\text{Fermion Kinetic}} + \underbrace{\lambda \bar{\psi} \psi \phi}_{\text{Fermion Mass}} \\ & + \underbrace{|D_\mu \phi|^2}_{\text{Higgs Kinetic}} - \underbrace{V(\phi)}_{\text{Higgs Potential}} \end{aligned} \quad (2.12)$$

⁴⁷³ **Chapter 3**

⁴⁷⁴ **Top-quark physics**

⁴⁷⁵ The third generation of quarks was first proposed by Kobayashi and Maskawa in a paper
⁴⁷⁶ published in 1973 [10] as a way to explain the CP violation observed in Kaon decays. The
⁴⁷⁷ existence of the third generation was confirmed when the lighter of the two constituents,
⁴⁷⁸ the b quark, was discovered in 1977 [12].

⁴⁷⁹ Due to its large mass, direct confirmation of the existence of the top quark required
⁴⁸⁰ the construction of very powerful accelerators. The top quark was discovered by the
⁴⁸¹ CDF and D0 experiments at Fermilab in 1995 [13, 14] and then observed at CERN in
⁴⁸² 2010 [15, 16].

⁴⁸³ The large mass of the top quark makes it a very interesting object of study. The
⁴⁸⁴ current world average for the mass of the top quark is

$$m_t = 173.07 \pm 0.52 \text{ (stat.)} \pm 0.72 \text{ (syst.) GeV} \quad (3.1)$$

⁴⁸⁵ based on results from Tevatron and the LHC [1].

⁴⁸⁶ Due to its mass the top quark has an extremely short lifetime $\tau \approx 0.5 \times 10^{-24}$ s, too
⁴⁸⁷ short to interact via the strong force and hadronize into a bound state [17]. Instead the
⁴⁸⁸ top quark decays weakly producing a W boson and a b quark almost exclusively. This
⁴⁸⁹ allows experimentalist to directly study the properties of a bare quark. An impossibility
⁴⁹⁰ with the other quarks which bind with other quarks to form hadrons. Measurement
⁴⁹¹ of top quark properties (mass, charge, forward-backward asymmetry, couplings, etc...)
⁴⁹² forms a large part of high energy physics research. Measurement of these properties

493 provide rigorous tests of the SM, point towards the existence of new physics or exclude
494 some BSM theories.

495 From an experimental perspective, top quark decays can produce a very interesting
496 signature which includes leptons, jets and transverse missing energy \cancel{E}_T due to the
497 escaping neutrino¹. The study of top quark decays relies on all parts of a general
498 purpose detector such as ATLAS or CMS. In additional $t\bar{t}$ pair production constitutes a
499 background for many other SM and BSM searches, as such understanding this process
500 well is fundamental for almost all areas of HEP research.

501 3.1 Top quark production

502 Top quarks can be produced in two manners, single top production and $t\bar{t}$ pair produc-
503 tion. In the SM, the dominant top quark pair production mechanism proceeds via the
504 strong force. The production cross-section of $pp \rightarrow t\bar{t}$ depends on the mass of the top
505 m_t , the centre-of-mass energy $s = 4E_{\text{beam}}^2$ and the fraction of the momentum taken by
506 the partons² of the colliding protons.

507 In order to produce a $t\bar{t}$ pair the total energy carried by the interacting partons must
508 be larger than two times the mass of the top. Let us define the effective centre of mass
509 energy \hat{s} which reflects the true amount of energy available for interaction. Given two
510 colliding partons, denoted i and j carrying x_i and x_j fractions of the centre of mass
511 energy \sqrt{s} , then

$$\hat{s} = x_i \sqrt{s} x_j \sqrt{s} = x_i x_j s \quad (3.2)$$

512 assuming that both partons carry the same fraction of the total energy, i.e. $x_i \approx x_j$
513 then the minimum value of x required for $t\bar{t}$ production is

$$x \approx \frac{2m_t}{\sqrt{s}} \quad (3.3)$$

514 At the LHC the minimum threshold at $\sqrt{s} = 7(14)$ TeV is approximately 0.05(0.025).
515 At such low values of x the number of gluons inside the proton is large [18] and thus
516 gluon fusion interactions dominate. Gluon fusion processes represent 80(90)% of the

¹Neutrinos do not interact with the detector material and thus escape without being detected

²Constituents of the hadrons, so quarks and gluons

⁵¹⁷ total cross section at $\sqrt{s} = 7(14)$ TeV, with the remainder contribution coming from
⁵¹⁸ quark pair annihilation. The feynman diagrams for these interactions are shown in
⁵¹⁹ Figure 3.1. The theoretical inclusive $t\bar{t}$ production cross section at the LHC has been
⁵²⁰ calculated at Next-to-Leading Order (NLO) to be $\sigma(t\bar{t}) = 172 \pm 7$ pb at $\sqrt{s} = 7$ TeV
and 246 ± 10 pb for $\sqrt{s} = 8$ TeV.

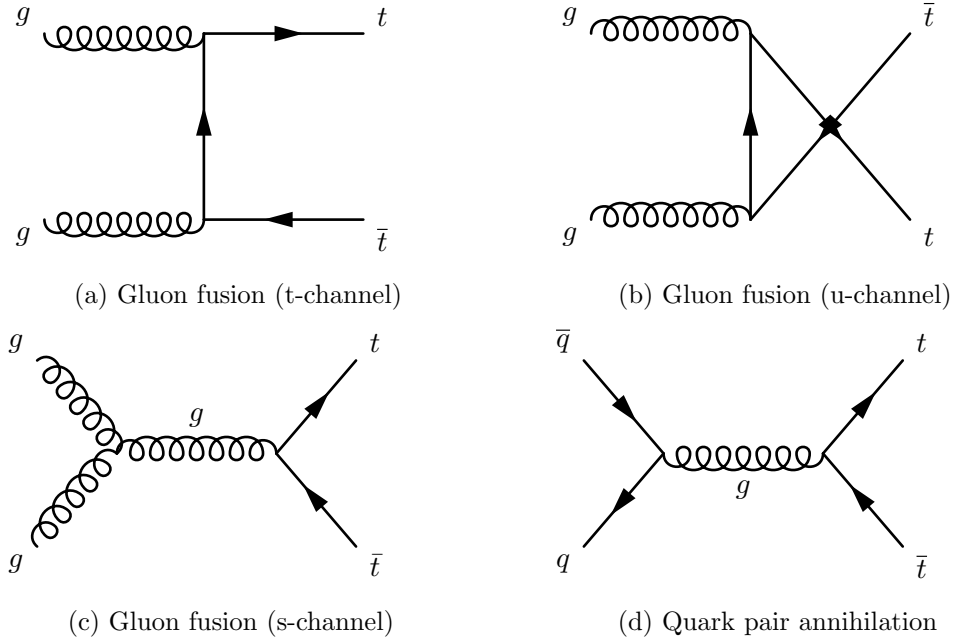


Figure 3.1: The leading order Feynman diagrams for $t\bar{t}$ production.

⁵²¹
⁵²² Single top production occurs via the weak force almost exclusively through the Wtb
⁵²³ vertex since $|V_{tb}| \gg |V_{ts}|, |V_{td}|$. At LO there are several production mechanisms for
⁵²⁴ single-top events:

- ⁵²⁵ • Weak quark-antiquark annihilation forming a W which subsequently decays into
⁵²⁶ a $t\bar{b}$ (Figure 3.2a).
- ⁵²⁷ • The so-called tW production, where a b quark absorbs a gluon and decays to a t
⁵²⁸ and W (Figure 3.2b).
- ⁵²⁹ • b quark scattering off a W boson, where the b comes from gluon splitting (Fig-
⁵³⁰ ure 3.2c) or from the proton (Figure 3.2d)³.

³There is a none zero probability that b quark will be emitted from a proton.

As top quark pair production can proceed via the strong force it occurs overwhelmingly more often than single top production. The inclusive cross-sections for $pp \rightarrow t\bar{t}$ and $pp \rightarrow t + X$ at the LHC have been estimated at NLO [2, 3]. As can be seen from Table 3.1 the production cross section of $t\bar{t}$ is approximately two times larger than the single-top cross-section.

Process	$\sqrt{s} = 7$ TeV	$\sqrt{s} = 8$ TeV
Single top $\sigma(t\text{-chan})$ [pb]	66 ± 2	87 ± 3
Single top $\sigma(Wt)$ [pb]	15.6 ± 1.2	22.2 ± 1.5

Table 3.1: Summary of the predicted SM single top production [2] and top pair production [3] cross sections at the LHC for $\sqrt{s}=7$ and 8 TeV.

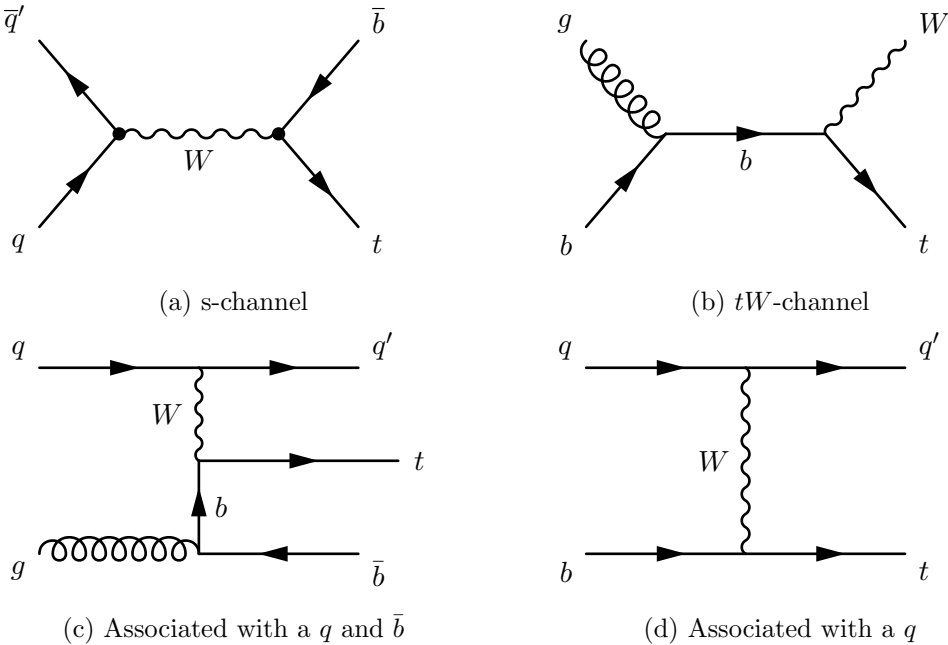


Figure 3.2: Example Feynman diagrams for single top quark at leading order.

535

3.2 Top quark decay modes

The top quark decays almost exclusively into a W boson and a b -quark. The ratio of branching ratios $\Gamma(t \rightarrow Wb)/\Gamma(t \rightarrow Wq(q = b, s, d))$ is 0.91 ± 0.04 [1].

As the LHC collides proton-proton beams, the overwhelming majority of events produced will feature multiple hadronic *jets*, a stream of particles resulting from the

Decay	Branching ratio
$W \rightarrow e + \nu$	$(10.75 \pm 0.13)\%$
$W \rightarrow \mu + \nu$	$(10.57 \pm 0.15)\%$
$W \rightarrow \tau + \nu$	$(11.25 \pm 0.20)\%$
hadrons	$(67.60 \pm 0.27)\%$

Table 3.2: Branching ratios for the decay of W boson. Note that the “hadrons” refers to a possible combination of $q\bar{q}'$ where \bar{q}' denotes the antiquark of a flavour different to that of the first quark.

hadronization of quarks in the detector, most of which will originate from “light” quarks⁴. Unlike these light quarks, b quarks leave a distinct signature in the detector as they travel a certain distance within a B hadron before producing a jet. Additional features such as the semi-leptonic decay of b quarks can be exploited to determine the presence of such a quark in the detector. Collectively analysis techniques that permit the detection of b -jets are known as *b-tagging*. Top quark events will produce two b quarks, making b-tagging techniques a central part of any $t\bar{t}$ analysis.

The other part of the top decay, the W boson is used to classify $t\bar{t}$ events. As discussed in Section 2, W bosons can decay leptonically ($\ell\nu_\ell$) or hadronically ($W \rightarrow q\bar{q}'$) driven by the CKM vertex element, since $\Gamma \propto |V_{ij}|^2$. The various branching ratios of W decays are presented in Table 3.2.

Thus $t\bar{t}$ events are labelled as “dilepton”, “all-hadronic” or “lepton + jets” depending on the combination of W decays present. The probability for $t\bar{t}$ event to be of a given type is dependent on the branching-ratios of W decays shown a priori. As can be seen from Figure 3.3 the all-hadronic events dominate, followed by the lepton plus jets and dilepton. Each of these types requires a very different analysis approach due to their distinct backgrounds, branching-ratio, detector signature and reconstruction requirements.

The all-hadronic final state includes four light quarks which will hadronize to form four Light Flavour (LF) jets and two b quarks leading to two b jets. Due to the large hadronic activity the all-hadronic channel is very challenging. As mentioned before, hadronic collisions produce events with a large number of quarks – and thus jets – in the final state. The background to the all-hadronic channel are therefore very high. As

⁴The term light quarks usually refers to quarks in the first two generations. Light jets are those originating from those quarks

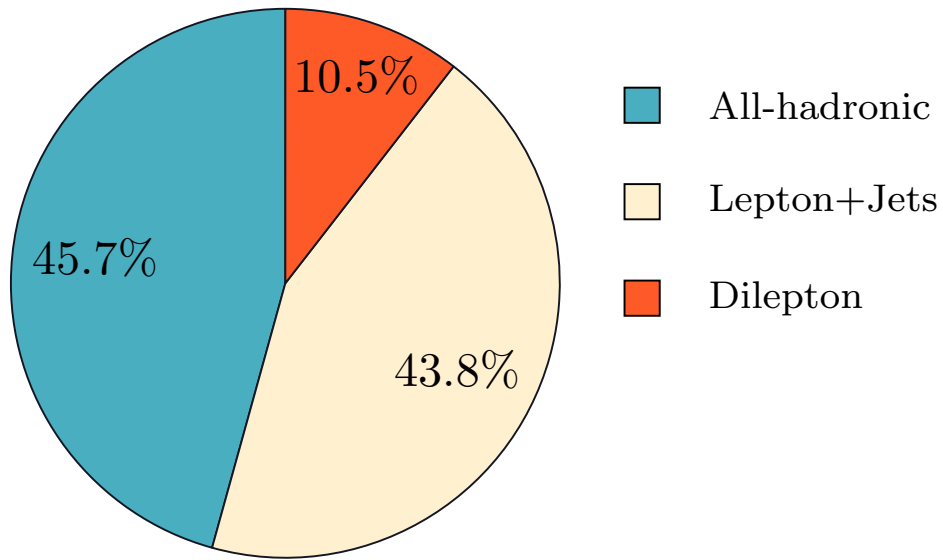


Figure 3.3: Branching ratios of all possible $t\bar{t}$ decays. These probabilities are based on the branching-ratios of W decay shown in Table 3.2.

563 shown in Figure 3.3, the all-hadronic channel has the largest branching ratio of the three.

564 The dilepton final state includes two leptons, large \cancel{E}_T from two neutrinos which
 565 escape the detector and two b jets. In contrast to the all-hadronic channel, dilepton
 566 events are very clean due to the presence of leptons and \cancel{E}_T , however the branching
 567 ratio is very small and reconstruction of the top is challenging due to the presence of two
 568 neutrinos which escape the detector without interacting.

569 Finally, the lepton plus jets channel has a large branching ratio while having a distinct
 570 signature with an isolated lepton⁵ and \cancel{E}_T as well as LF and b jets. Note that leptons
 571 in this case refers to e and μ . The τ lepton is unstable and sufficiently heavy to decay
 572 baronically via the weak force producing two quarks, losing the advantageous distinct
 573 signature of a lepton plus jets event. An example of the full lepton plus jets chain is
 574 shown in Figure 3.5.

⁵A lepton produced far from other physics objects (jets, leptons, etc...)

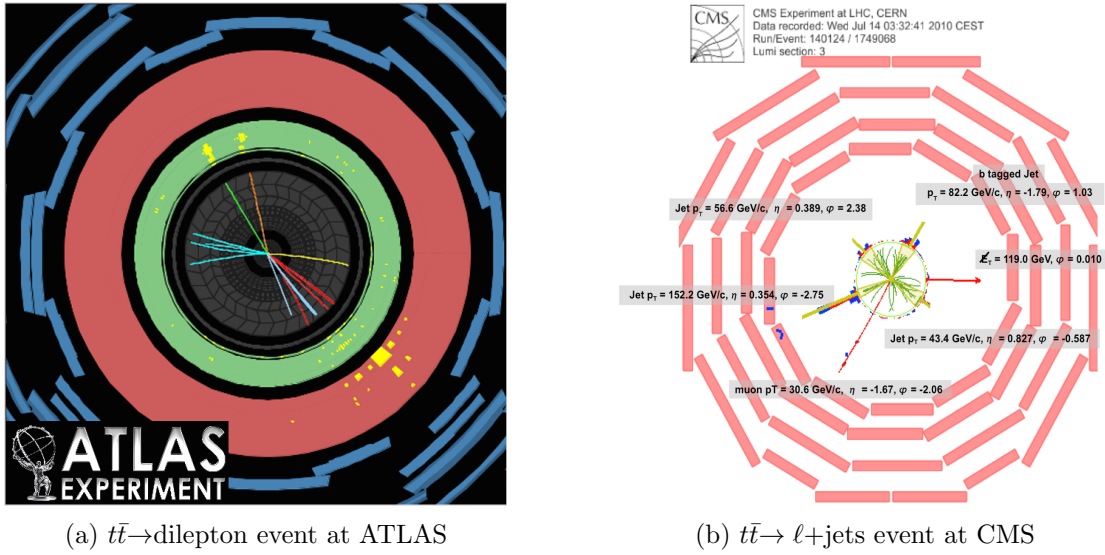


Figure 3.4: Example event displays of (a) a dilepton $t\bar{t}$ event recorded by ATLAS and (b) a $\ell+jets$ event recorded at CMS.

575 3.2.1 Motivations for selecting the $\ell+jets$ channel

576 Due to its distinct signature and high branching ratio the lepton plus jets channel was
 577 chosen as the focus for the analyses presented in this thesis. Additionally the presence
 578 of only one neutrino allows for a reconstruction of the mass of the leptonic top (the
 579 top whose associated W decays leptonically) in the transverse plane and a full mass
 580 reconstruction of the top mass on the hadronic side⁶.

581 3.3 Latest developments in top physics

582 This section discusses a few of the latest measurements in the area of top quark pair
 583 production with a focus on LHC results.

584 As discussed top quark decays provide the only probe to study the properties of a
 585 bare quark. Measurements of its properties provide a stringent test of the SM and could
 586 show hints of new physics from BSM theories. Moreover due to its final state signature,
 587 top quark pair production particularly in the lepton + jets channel, form the background
 588 to many searches for new physics. Additionally all parts of the detector are utilized in
 589 the reconstruction of $\ell+jets$ events and as such it is possible to use these events to tune

⁶The methods used for this mass reconstruction is complex and not discussed in this thesis

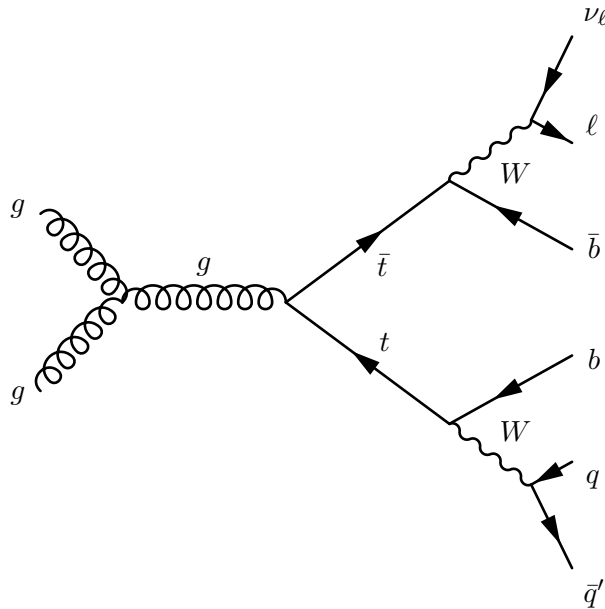


Figure 3.5: The feynman diagram of lepton plus jets channel including $t\bar{t}$ production via gluon fusion and decay with a leptonically decaying W^+ . Note that all other production mechanisms are also considered and the final state where the W^- is decayed leptonically is also taken into account.

590 or *calibrate* many analysis and reconstruction techniques.

591 **Cross-section measurement**

592 Measurement of the cross-section of the top quark is a benchmark test of the SM. Any
 593 statistically significant deviation from the predicted value could point to the presence of
 594 new physics. Some BSM theories posit the existence of particles which could decay to
 595 produce a $t\bar{t}$ pair. If such theory is correct this would be observed in an increase in the
 596 cross section measured away from the predicted SM value.

597 Experimentally measurement of the cross-section is vital when attempting to reduce
 598 and estimate the amount of top quark background present in other analyses. Searches
 599 for the Higgs boson, exploit many different channels, many of which include $t\bar{t}$ events as
 600 a background. The type of events predicted by the BSM theory, Supersymmetry (SUSY)
 601 include a large amount of \cancel{E}_T , leptons and jets in the final state. Top quark pair events
 602 mimick these processes and constitute a large background.

603 A summary of all $t\bar{t}$ cross section measurements from the LHC is shown in Figure 3.6

and a comparison against the Tevatron measurement at $\sqrt{s} = 1.96$ TeV is shown in Figure 3.7.

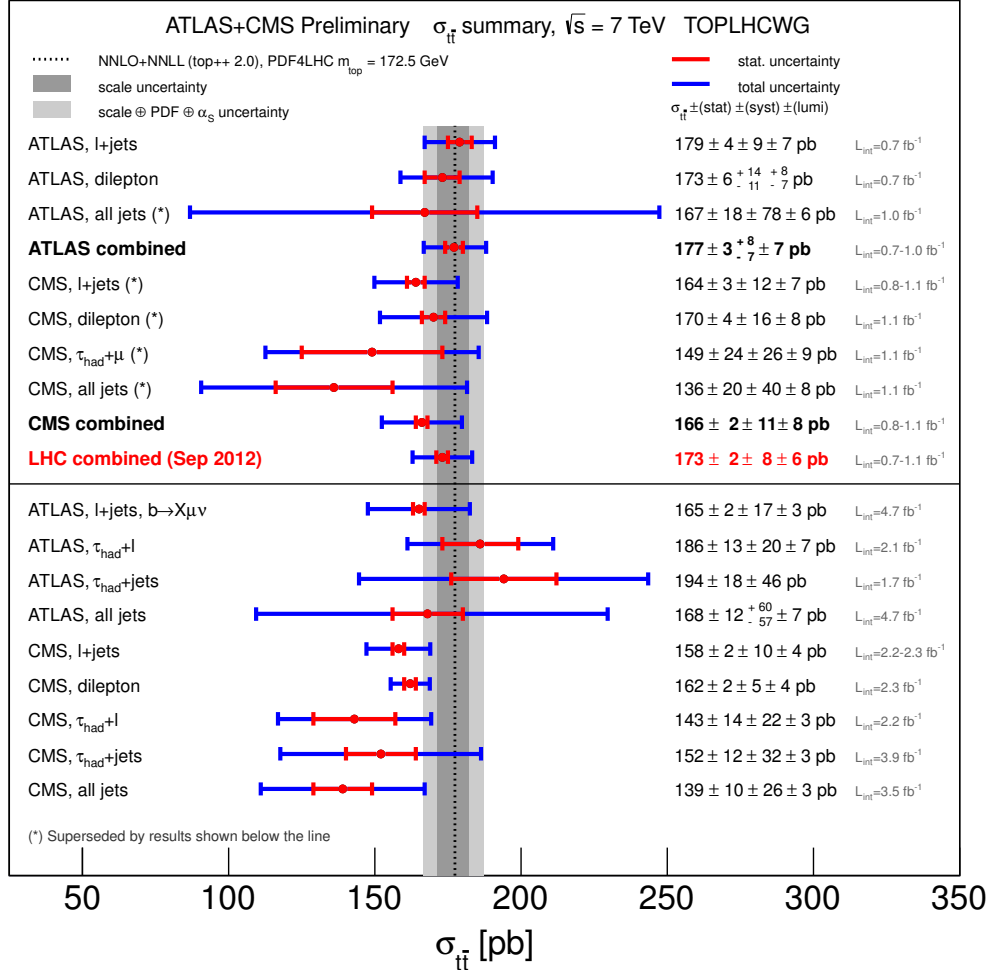


Figure 3.6: A summary of all $t\bar{t}$ production cross section measurements performed at the LHC at $\sqrt{s} = 7$ TeV. Note the theory prediction shown as a dotted black line with its associated uncertainties as grey bands. The results shown above the black line have been statistically combined, producing the results labelled as **combined**. Many of these analyses have been superseded and the results are shown below the line. Other analyses performed but not included in the combination are also shown below the line.

606 Top mass measurement

607 The mass of the top m_t is a fundamental parameter of the SM. The

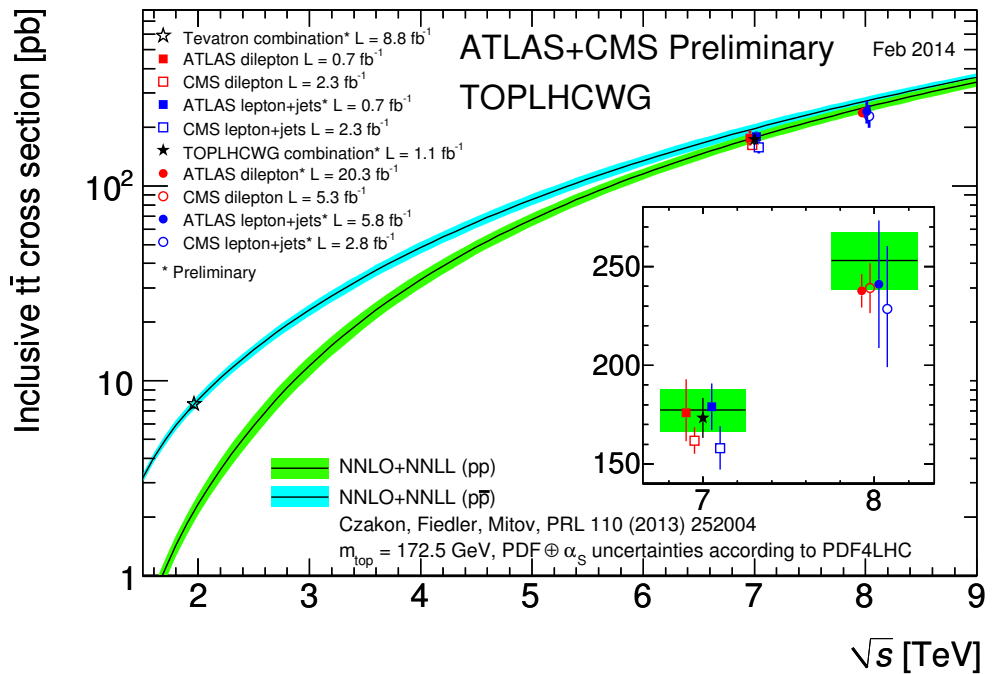


Figure 3.7: A summary of the most precise $t\bar{t}$ production cross section measurements performed at the LHC at $\sqrt{s} = 7$ and 8 TeV and the Tevatron at $\sqrt{s} = 1.96$ TeV compared to the theoretical prediction. Note that the Tevatron results should be compared against the prediction for $p\bar{p}$ collisions while the LHC against the pp collision predictions.

608 **Mass asymmetry measurement**

609 As discussed in Section 2.3, the charge (C) and parity (P) symmetries are both violated
 610 in weak interactions. The CPT symmetry which includes time reversal (T) is the last
 611 remaining symmetry which no interaction appears to violate. Any deviations from this
 612 symmetry would have major implications on particles physics [19] and could manifest
 613 itself as differences between matter and antimatter particles. As the only quark which
 614 can be studied directly, measurement of $\Delta m \equiv m_t - m_{\bar{t}}$ could hint at any such deviation
 615 produced by new physics. Such a measurement was conducted by the ATLAS [20]
 616 experiment yielding the result:

$$\Delta m_t = -0.44 \pm 0.46 \text{ (stat.)} \pm 0.27 \text{ (syst.) GeV} \quad (3.4)$$

617 and by the CMS [21] experiment yielding the result:

$$\Delta m_t = 0.67 \pm 0.61 \text{ (stat.)} \pm 0.41 \text{ (syst.) GeV} \quad (3.5)$$

618 which are both consistent with the SM prediction and imply CPT invariance.

619 **Charge asymmetry**

620 Many BSM theories can affect the charge symmetry between top and antitop quarks.
 621 Once again any deviations from the SM prediction would point to the existence of new
 622 BSM physics. The charge asymmetry as measured by the ATLAS experiment [22] is

$$A_c = 0.006 \pm 0.010 \quad (3.6)$$

623 and as measured by CMS [23]

$$A_c = -0.010 \pm 0.017 \text{ (stat.)} \pm 0.008 \text{ (syst.)} \quad (3.7)$$

624 which once again are consistent with the SM prediction.

625 **Boosted top searches**

626 **Chapter 4**

627 **The LHC and the ATLAS
628 Detector**

629 **4.1 The Large Hadron Collider**

630 The Large Hadron Collider (LHC) [24] is a proton ring collider located at the European
631 Centre for Nuclear Research (CERN). The main LHC ring is housed in the tunnel which
632 previously contained the Large Electron-Positron collider. The LHC ring is 27km in cir-
633 cumference and located approximately 175m underground. The LHC services four dif-
634 ferent experiments located at four interaction points around the beam-pipe (Figure 4.1).
635 A toroidal LHC apparatus (ATLAS, the experiment used for this thesis), the compact
636 muon solenoid (CMS), a large ion collider (ALICE) experiment and the LHC beauty
637 (LHCb) experiment.

638 ATLAS and CMS are general purpose detectors designed to support a varied physics
639 programme, from SM physics like top quark measurements to BSM searches such as
640 supersymmetry. ALICE and LHCb are more specialized experiments which focus on
641 heavy ions and b physics, respectively.

642 The LHC accelerates two beams of protons in opposite directions and then collides
643 the two beams at the four interaction points where the experiments are located. The
644 protons come from hydrogen gas where the orbiting electron is removed by an electric
645 field, leaving behind a bare proton. The beam acceleration occurs in several stages

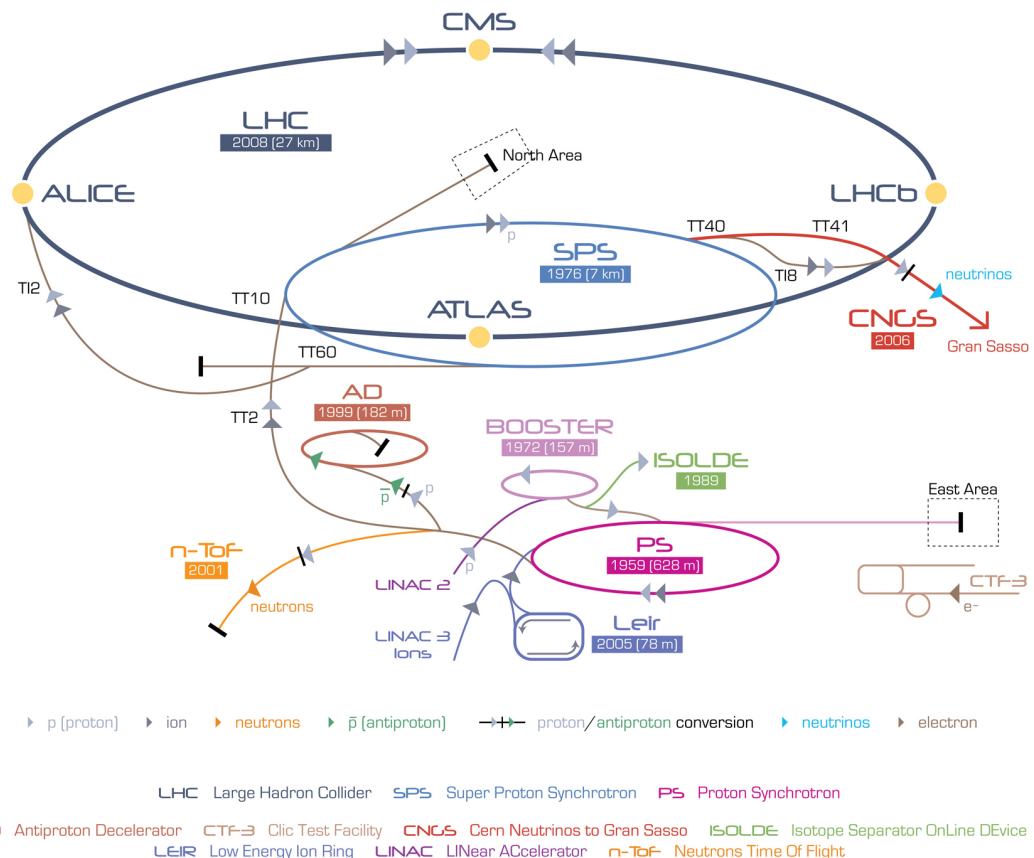
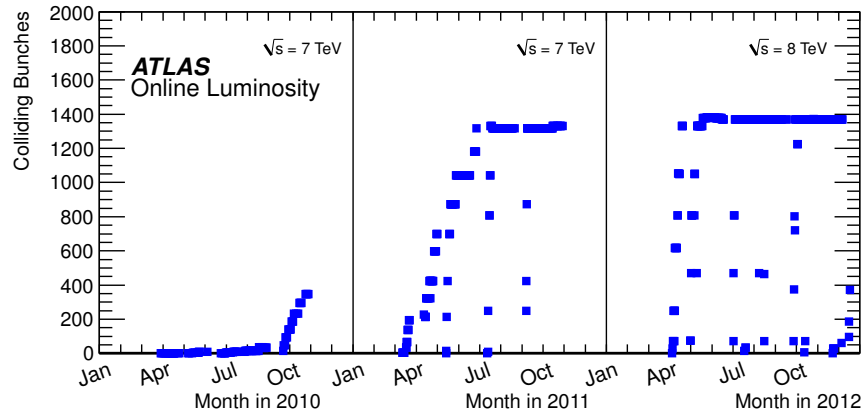
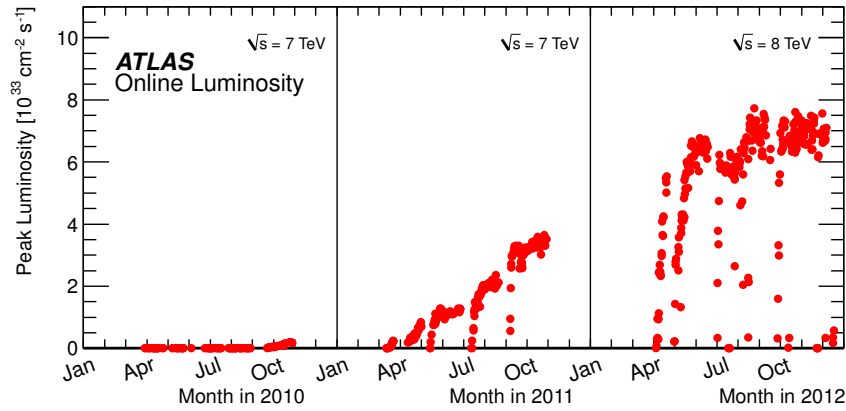


Figure 4.1: The layout of CERN complex of experiments, note the main four LHC experiments located at different points around the ring.

exploiting smaller experiments present at CERN. During 2010 and 2011 protons were accelerated to a beam energy of 3.5 TeV, creating a centre-of-mass energy of 7 TeV and then 4 TeV per beam in 2012 for a centre-of-mass energy of 8 TeV. Each beam is made of multiple bunches of protons, with as many as hundreds of billions of protons in each bunch. Bunches are grouped into *bunch trains* with a designed *bunch spacing* of 25 ns between each of the bunches that compose a single train. Note that the bunch spacing and size of the bunch can be altered to adjust the amount of collisions and the time between collisions. The variation in the number of colliding bunches is shown in Figure 4.2a.



(a) The number of bunches colliding per unit time at the LHC for the 2010, 2011 and 2012 pp collision periods.



(b) The peak luminosity per unit time at the LHC for the 2010, 2011 and 2012 pp collision periods.

Figure 4.2: Shown in (a) is the number of bunches colliding at the LHC and (b) the peak luminosity per unit time.

655 The acceleration of the proton beams occurs in several stages, within several different
 656 accelerators. The beams are first accelerated in a linear collider (LINAC 2) to an energy
 657 of 50 MeV before being injected into the proton synchotron booster (PSB). The beams
 658 are then boosted to 1.4 GeV by a varying magnetic field in the circular PSB. The beams
 659 are then passed into the proton synchrotron (PS) and then the super proton syncrotron
 660 (SPS) where the beam energy increases to 26 GeV and then 450 GeV. At this stage the
 661 beam is injected into the LHC and then accelerated to the final desired energy. The
 662 design energy is 7 TeV per beam for a total of 14 GeV centre-of-mass energy. From
 663 injection of the protons into LINAC 2 to stable beam conditions in the LHC, the whole
 664 process can take a couple of hours.

665 As bunches overlap the protons that make up the bunches interact, these interac-
 666 tions are known as events. The number of events is proportional to the instantaneous
 667 luminosity \mathcal{L} of the collider. \mathcal{L} is a measure of the flux of particles per unit area per unit
 668 time can be defined as:

$$\mathcal{L} = f n_b \frac{N_1 N_2}{A} \quad (4.1)$$

669 where f is the frequency of revolution of the beam, n_b the number of colliding pairs of
 670 bunches in the beam, N_1 and N_2 are the number of particles in each colliding bunch and
 671 A is the cross-section of the beam [25]. The peak luminosity evolution at the LHC is
 672 shown in Figure 4.2b. Note that the operational \sqrt{s} of the LHC was 7 TeV for 2010/11
 673 and 8 TeV for 2012.

674 The total amount of data collected is measured by the integrated luminosity \mathcal{L}_{int}
 675 defined as the time integral of \mathcal{L} . Integrated luminosity has units of inverse area, usually
 676 expressed in terms of barns (b)¹. The probability for a given process to occur is expressed
 677 as the cross-section σ and the total number of events which proceed via said process is
 678 defined as:

$$\sigma \int \mathcal{L} dt \quad (4.2)$$

679 The integrated luminosity delivered by the LHC and collected by the ATLAS detector
 680 in 2011 and 2012 is shown in Figure 4.3. The ATLAS detector does not record all data

¹ $1 b^{-1} = 10^{-28} m^{-2}$

681 delivered by the LHC; approximately 6.5% was not recorded.

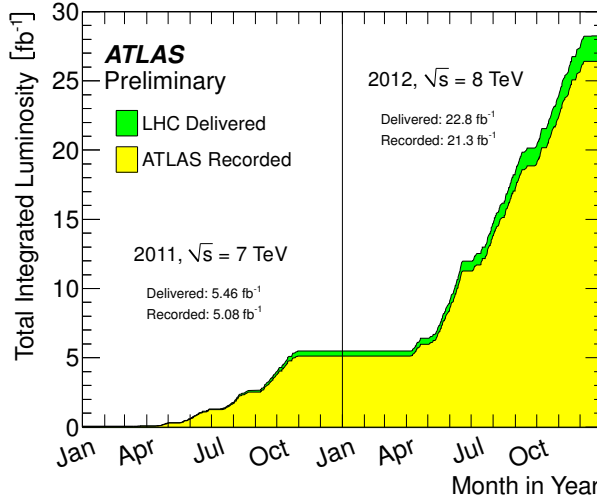


Figure 4.3: Distribution of the total integrated luminosity delivered by the LHC and the recorded by ATLAS for the 2011 and 2012 pp collision period. Note the \sqrt{s} changing from 7 TeV to 8 TeV between 2011 and 2012.

682 4.1.1 Pileup

683 Due to the large number of interactions and the short time between collisions, multiple
 684 events can overlap into a single event. This has detrimental effects on physics analyses
 685 and is a determining factor in setting the instantaneous luminosity with which to perform
 686 data collection. This overlapping effect is collectively known as pileup and is categorized
 687 into two types: in-time pileup, where multiple pp collisions occur during the same bunch
 688 crossing; and out-of-time pileup, where the electric signals produced by a previous colli-
 689 sion is still present in the detector. The number of interactions per crossing μ is shown in
 690 Figure 4.4, note that on average approximately thirty interactions occurred per bunch
 691 crossing in 2012. In comparison, in 2011 the average interactions per bunch crossing
 692 $\langle \mu \rangle$ varied from $\langle \mu \rangle = 5$ in early 2011 to $\langle \mu \rangle = 15$ at the end of the year. The
 693 large number of overlapping events has a detrimental effect on physics analyses and thus
 694 is an important factor when setting the operational \mathcal{L} of the collider.

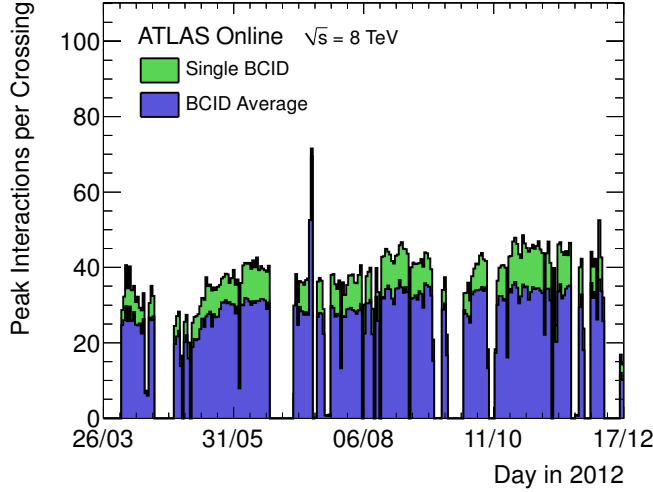


Figure 4.4: Number of interactions per bunch for the 2012 pp data-taking period at ATLAS per day. Note that both the average number of interactions for all bunches and the maximum number of interactions are shown.

695 4.2 The ATLAS detector

696 The ATLAS [26] experiment is a general-purpose detector which wraps around the IP
 697 providing large angular coverage. ATLAS is approximately cylindrical with a diameter
 698 of 25m, a total length of 44m and weighs 7000 tonnes. The detector is made of several
 699 layers of instrumentation located at successively increasing radii as shown in Figure 4.5:

700 1. **Inner Detector:** Located nearest to the beam-pipe and designed to measure the
 701 track of charged-particles.

702 2. **EM Calorimeter:** Used for identification and measurement of electrons and pho-
 703 tons.

704 3. **Hadronic Calorimeter:** Used for the measurement of hadronic activity from
 705 hadronizing partons and missing transverse energy.

706 4. **Muon Spectrometer:** The outermost detection layer, used for muon identifica-
 707 tion and measurement.

708 Between these detection layers are magnets responsible for bending the path of the
 709 charged particles for the purpose of momentum measurement and particle identification.

710 Additionally triggering and data acquisition (DAQ) systems form part of the detector
 711 for the purposes of recording the data signals coming from the aforementioned tracking
 712 and measurement systems. A brief description of these systems is provided in the coming
 713 sections. For a more detailed technical description of the detector and all subsystems
 714 see [27].

715 Semi-leptonic $t\bar{t}$ events produce a final state that includes hadronic activity, elec-
 716 trons, muons and missing energy and thus all elements of the detector are used in the
 717 reconstruction of such events. Additionally the match χ^2_{match} -tagger which is central to
 718 this thesis relies on the reconstruction and fitting of inner detector tracks and muon
 719 spectrometer tracks. A detailed description of this algorithm is provided in the Chap-
 720 ter 6.

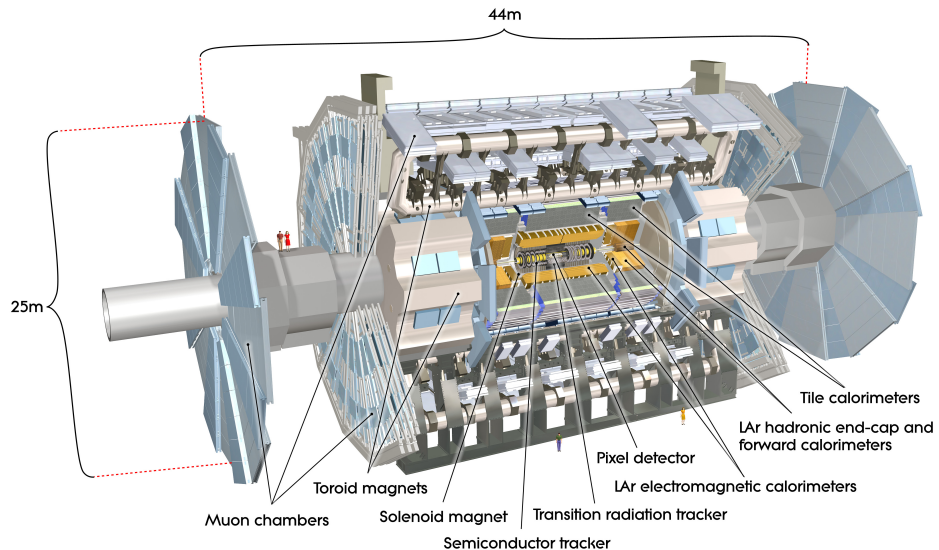


Figure 4.5: An overview diagram of the ATLAS experiment. Shown are all detection and tracking systems and the toroid magnet which encompasses them. Note also the muon system on the outside of the detector.

721 A cylindrical coordinate system as used by all ATLAS publications has been adopted
 722 here. The coordinate system is constructed so that the z -axis is parallel to the beam
 723 axis. The x -axis is positive in the direction going from the IP to the centre of the
 724 LHC ring, and the positive y -axis points upwards. Thus the $x - y$ plane is transverse
 725 to the beam direction. All transverse variables such as the transverse momentum p_T ,
 726 transverse energy E_T and missing transverse energy \cancel{E}_T are measured along this plane.

727 The azimuthal angle ϕ is measured around the beam axis, and the polar angle θ is
 728 the angle from the beam axis. The pseudorapidity is defined as $\eta = -\ln \tan(\theta \div 2)$.
 729 The distance in the ϕ - η plane between two objects is denoted by ΔR and defined as
 730 $\Delta R = \sqrt{\Delta\phi^2 + \Delta\eta^2}$. Finally side A of the detector is defined as the positive z side and
 731 side C is the negative z .

732 4.2.1 Inner Detector

733 The inner detector (ID) is a tracking detector located closest to the beam-pipe and used
 734 for momentum and impact parameter measurement, vertex and track reconstruction and
 735 particle identification. The ID is designed to provide hermetic, high-resolution tracking
 736 in the range $|\eta| < 2.5$. All components of the ID subsystem are shown in Figure

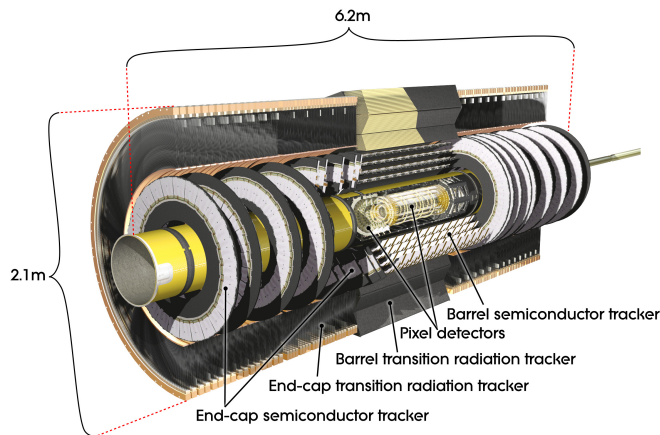


Figure 4.6: caption

737 The entire ID is contained within the central solenoid (CS) that generates a 2 T
 738 magnetic field for the purpose of momentum measurement. The trajectory of a charged
 739 particle is bent in the presence of a magnetic field. The str by a magnitude dependent
 740 on the momentum of the particle. By reconstructing this trajectory the momentum can
 741 be measured.

742 The reconstruction of interaction vertices is of paramount importance, particularly
 743 when considering the large amount of pile-up observed at ATLAS. Interaction vertecies
 744 are reconstructed by fitting all reconstructed tracks to a point. The primary vertex
 745 (PV) is then defined as the vertex with the largest amount of momentum associated

746 with it. In addition the reconstruction of secondary interaction vertexes is used for the
 747 identification of short-lived particles such as B -hadrons and τ .

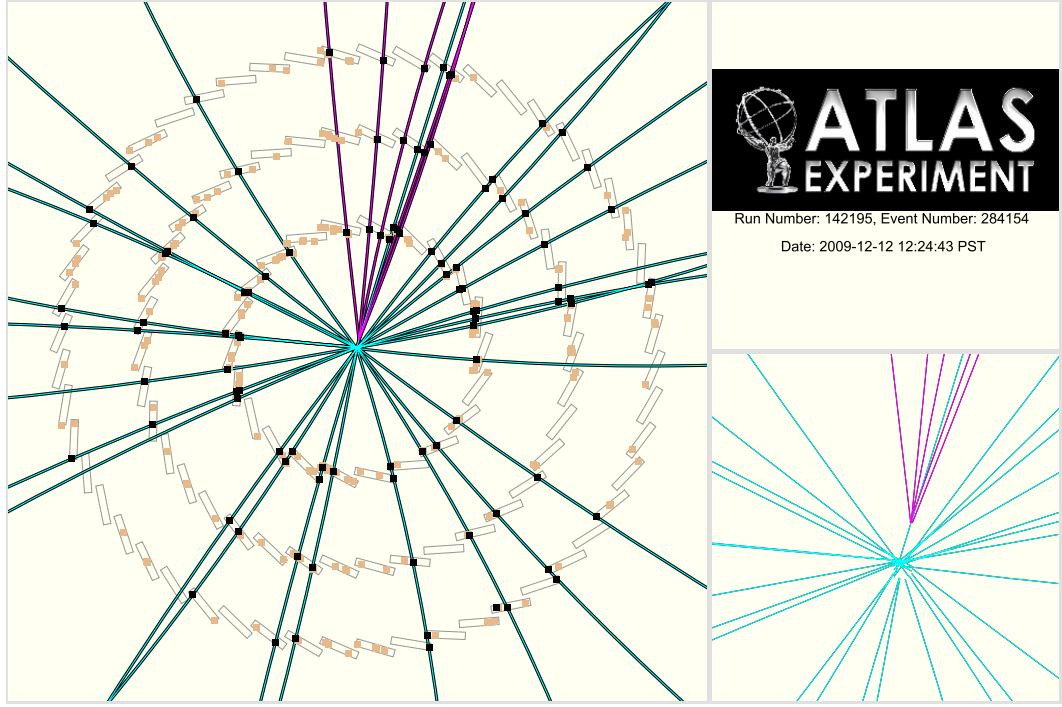


Figure 4.7: An event-display of an event as reconstructed by the ATLAS inner detector. Shown are the results of the vertexing algorithm where each line represents a track. the purple tracks have been fitted to a secondary vertex.

748 The ID is made of three separate tracking and detection systems located at increasing
 749 radii away from the beam-pipe, the full arrangement can be seen in Figure 4.8 and a
 750 plane-view is shown in Figure 4.9.

751 Pixel detector

752 The pixel detector is located nearest to the beam-pipe and provides high-granularity and
 753 precision for secondary vertex reconstruction. It consists of three silicon pixel sensors
 754 layers in the barrel region located at approximately 5cm, 9cm and 12cm from the IP,
 755 and three disks at each side located at constant R providing coverage up to $|\eta| < 2.5$.
 756 The barrel modules are overlapped in a turbine pattern to provide hermetic coverage. In
 757 the barrel region the modules provide an intrinsic resolution of $10\mu m$ in $R-\phi$ and $115\mu m$
 758 in z . The disk sections have an intrinsic resolution of $10\mu m$ ($R-\phi$) and $115\mu m$ (R).

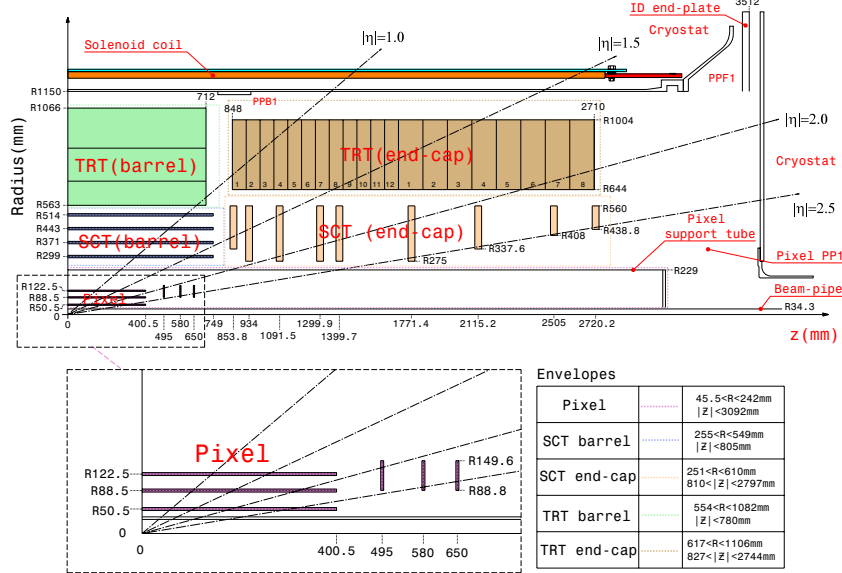


Figure 4.8: Plan-view of a quarter-section of the ATLAS ID showing the major detector elements with its active dimensions and envelopes. Note also the η markers showing the maximum coverage up to $\eta = 2.5$.

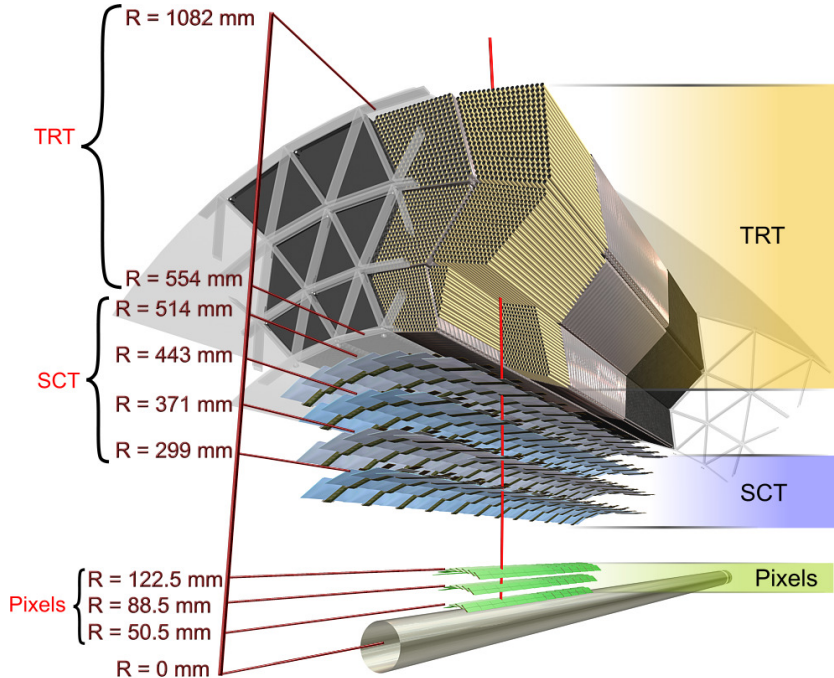


Figure 4.9: A drawing of in the transverse plane of the ATLAS ID showing all major detection elements in the barrel regions. Note the charged particle track marked in red traversing all the detector elements.

759 **Semiconductor tracker**

760 The semiconductor tracker (SCT) located in the intermediate radius range is designed
 761 to provide eight hits per track contributing to the measurement of momentum, impact
 762 parameter and vertex position. The SCT is made of four layers of stereo-pair silicon
 763 micro-strip sensors in the barrel region at increasing radii with an intrinsic resolution of
 764 $17\mu\text{m}$ ($R\text{-}\phi$) and $580\mu\text{m}$ (z). At the end-caps nine disks of silicon microstrip modules
 765 provide large η coverage with a resolution of $17\mu\text{m}$ ($R\text{-}\phi$) and $580\mu\text{m}$ (R).

766 **Transition radiation tracker**

767 The transition radiation tracker (TRT) is the outermost tracking layer that forms the
 768 inner detector. The TRT is designed to provide up to 36 hits per track using straw-
 769 tube sensors. In the barrel the 144cm long straw-tubes are arranged in modules which
 770 contain between 329 and 793 straws. The end-cap disks are made of radially distributed
 771 36cm long straw-tubes. Each straw-tube provides an intrinsic resolution of $130\mu\text{m}$ along
 772 its length. The combination of a large number of hits over a large radius allows for
 773 measurements in the TRT to be made with an accuracy that can complement those
 774 made by the pixel detector.

775 **4.2.2 Calorimetry**

776 The ATLAS calorimeter is responsible for the measurement of the energy of particles
 777 that emerge from the event. Sampling calorimeters are used for this purpose, layers
 778 of absorber material (passive) are placed in the path of the particles forcing them to
 779 interact and shower. The amount of energy lost by the incident particle depends on
 780 the type of material the particle traverses, the energy of the particle and the type. At
 781 high energies electrons lose energy predominantly via Bremsstrahlung, while photons
 782 lose energy via pair production. The characteristic length associated with this energy
 783 loss is a material characteristic known as the radiation length X_0 .

784 For electrons the energy as a function of material traversed is

$$E = E_0 e^{-x/X_0} \quad (4.3)$$

785 where E is the energy of the incident particle, E_0 is the original energy and x is the
 786 distance traversed. As an electron traverses one X_0 of material, its energy is reduced
 787 by a factor of $1/e$. For photons the average number of photons traversing through a
 788 material length x is reduced exponentially by a factor of $\frac{7}{9}X_0$.

789 The energy of the resulting shower is then measured by some sampling material
 790 (active) located behind the absorbers, this energy is proportional to the energy of the
 791 incident particle.

792 The type and thickness of material used is varied through the pseudorapidity range
 793 to improve energy measurement and reduce punch-through of particles into the muon
 794 systems behind. Due to the large amount of intense radiation produced during collisions,
 795 radiation hardness is also a driving factor in material choice.

796 The ATLAS calorimeter consists of the electromagnetic (EM) calorimeter, designed
 797 to measure photons and electrons covering the pseudorapidity region $|\eta| < 3.2$; the
 798 hadronic calorimeter (HCal), designed to measure hadronic activity covering the pseu-
 799 dorapdity region $|\eta| < 3.2$; and the forward calorimeter (FCal) which provides energy
 800 measurement capability in the very high pseudorapidity region $3.1 < |\eta| < 4.9$. As
 801 can be seen in Figure 4.10 the calorimetry envelopes the ID and CS providing hermetic
 802 coverage symmetric in ϕ . This is particularly important for the measurement of E_T
 803 resulting from weakly interacting particles escaping the detector.

804 **Electromagnetic calorimeter**

805 The EM calorimeter is made of a barrel section ($|\eta| < 1.475$) and two end-caps ($1.375 <$
 806 $|\eta| < 3.2$). The EM barrel consists of two half-barrels separated by a 4mm gap at $z = 0$.
 807 The end-caps consist of two coaxial wheels, the outer ring covering the pseudorapidity
 808 range $1.375 < |\eta| < 2.5$ and the inner ring covering the range $2.5 < |\eta| < 3.2$. The
 809 pseudorapidity region $1.37 < |\eta| < 1.52$ is not used for precision physics due to the large
 810 amount of material, this is known as the “crack” region.

811 The EM calorimeter employs liquid Argon (LAr) as the active material due to its
 812 intrinsic radiation hardness and response over time, and lead as the passive material
 813 arranged in an accordion geometry for full ϕ symmetry. Particles interact with the lead
 814 absorbers creating a shower which ionizes the layers of liquid Argon. A potential is ap-

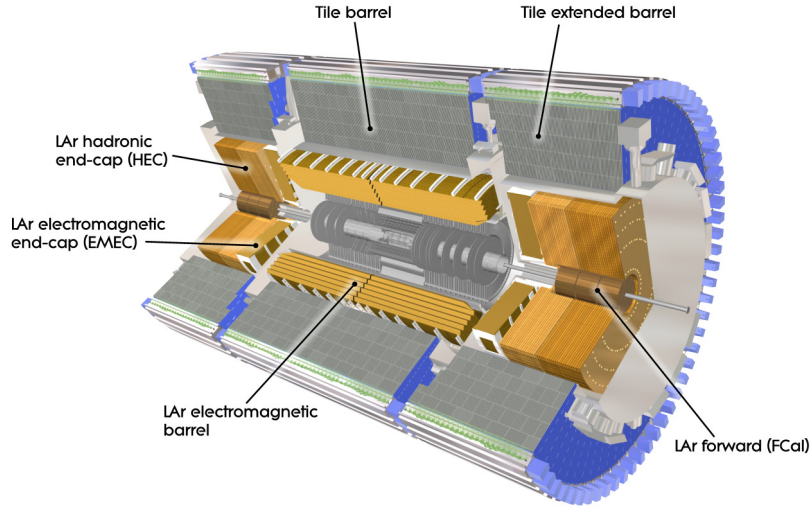


Figure 4.10: A cut-away diagram of the ATLAS detector highlighting the calorimetry system. Shown are the ECal barrel and end-cap, the HCal barrel and end-cap and the FCal end-cap.

Table 4.1: Design energy resolution of all ATLAS calorimeter components. The resolution is made of a sampling term ($1/\sqrt{E}$) associated with the choice of passive and active materials and construction of the layers and a constant term associated with the depth of the detector, cracks and dead material.

Section	Resolution
EM Barrel	$\frac{10\%}{\sqrt{E}} \oplus 0.7\%$
EMEC	$\frac{10\%}{\sqrt{E}} \oplus 0.7\%$
HEC	$\frac{100\%}{\sqrt{E}} \oplus 10\%$
FCAL	$\frac{100\%}{\sqrt{E}} \oplus 10\%$

plied across the LAr material allowing for signal readout via Kapton/copper electrodes.
 The total thickness of the EM calorimeter is $> 24X_0$ in the barrel and $> 26X_0$ in the end-caps. The amount of material is optimized in pseudorapidity to enhance energy resolution.

In the region devoted to precision physics the EM calorimeter is divided into three segments as shown in Figure 4.11, the strip layer is designed to improve particle identification and pseudorapidity position measurement. The design energy resolution for all components of the calorimeter are shown in Table 4.1.

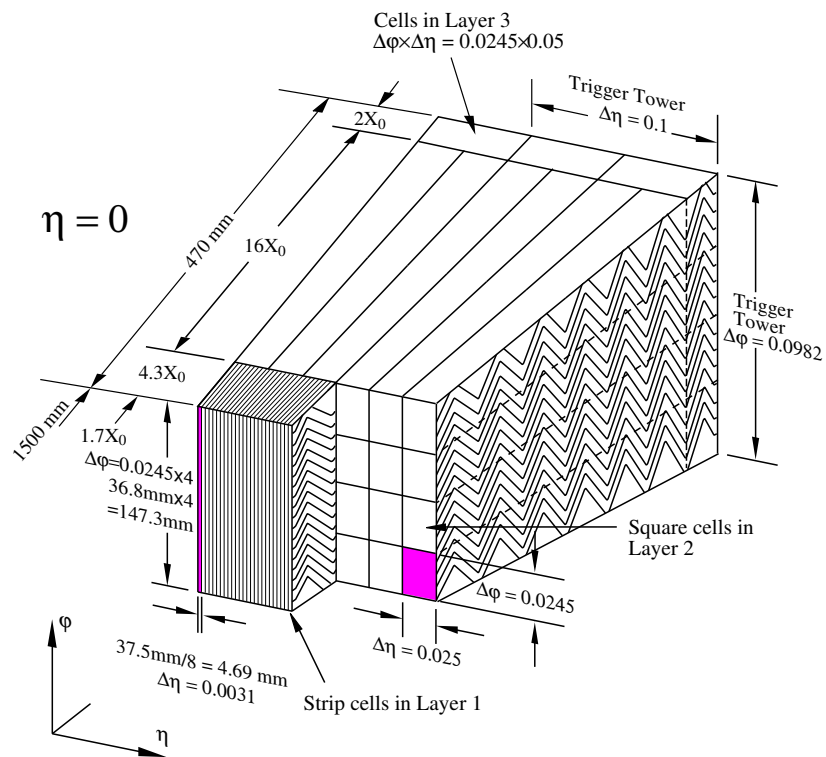


Figure 4.11: Cut-away diagram of the EM calorimeter barrel at $\eta = 0$. Shown are the three different layers with varying cell structures. The strip section is designed to enhance particle identification and position measurement in η .

823 **Hadronic calorimeter**

824 The hadronic calorimeter uses different types of passive and active material to accom-
825 modate for the varying conditions in different regions of the detector. The materials
826 used and structure of the detector must provide good energy resolution, full symmetric
827 coverage for the purpose of E_T measurement, full containment of all hardonic activity
828 to prevent punch-through to the muon system and be sufficiently radiation hard.

829 The hadronic calorimeter consists of two parts a scintillator tile calorimeter in the
830 barrel region, and a LAr calorimeter in the end-cap.

831 The tile calorimeter is located directly outside the EM calorimeter. The barrel por-
832 tion of the calorimeter covers the region $|\eta| < 1.0$ and the two extended barrels cover
833 the range $0.8 < |\eta| < 1.7$. The tile calorimeter uses steel as the passive material and
834 scintillating tiles as the active material. The resulting hadronic showers enter the scin-
835 tillating tiles and produce photons which are passed to photomultiplier tubes (PMTs).
836 The total detector thickness which is tile-instrumented is 9.7 interaction lengths (λ) at
837 $\eta = 0$.

838 The hadronic end-cap (HEC) uses LAr technology due to its radiation-hardness in
839 this challenging high pseudorapidity region. The HEC consists of two independent wheels
840 per end-cap covering the range $1.5 < \eta < 3.2$ overlapping the tile calorimeter at low
841 pseudorapidity range and the forward calorimeter located at high pseudorapidity.

842 **Forward calorimeter**

843 The forward calorimeter (FCal) is responsible for energy measurement in the very-high
844 pseudorapidity range $3.1 > |\eta| > 4.9$ of both electromagnetic and hadronic activity. Due
845 to the large amount of radiation in this η region, LAr is employed as the active material.
846 The FCal consists of three layers, the first made primarily of copper, designed mostly
847 for the measurement of electromagnetic activity while the two outer tungsten layers are
848 responsible for hadronic activity measurement.

849 4.2.3 Muon system

850 The muon system is the outer most layer of the ATLAS detector and is responsible for
851 the measurement of p_T charged-particles that traverse the ATLAS calorimetry.

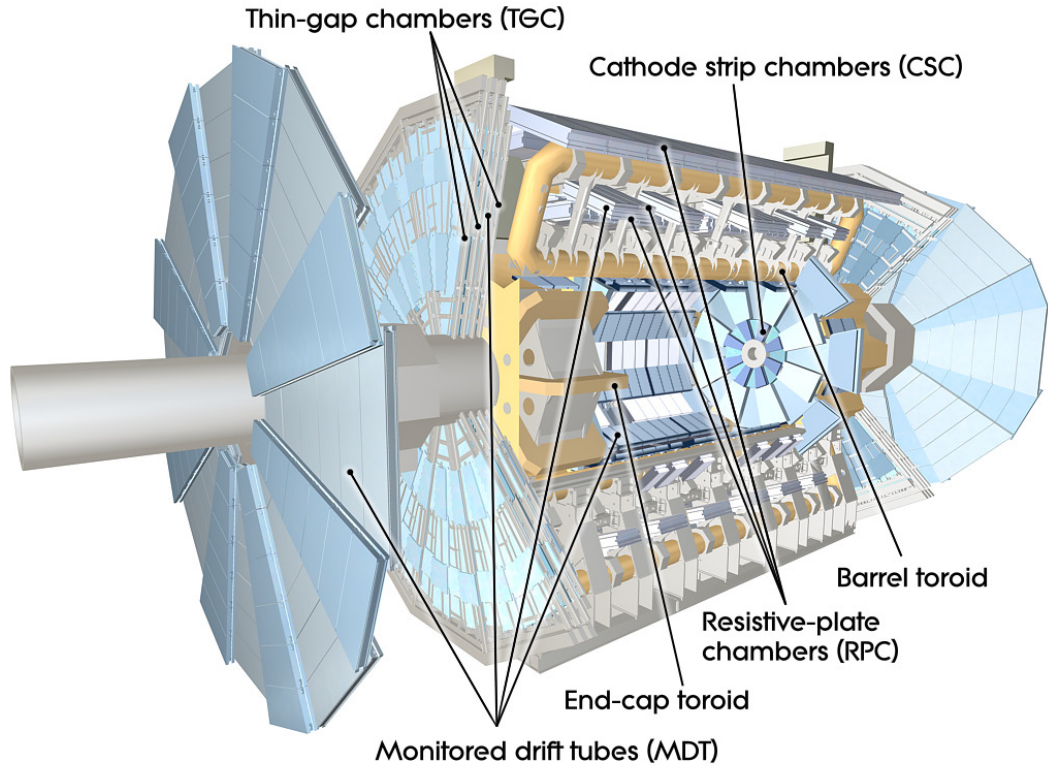


Figure 4.12: Cut-away drawing of the ATLAS muon system.

852 4.2.4 Triggering and DAQ**853 4.3 Athena Control Framework and ROOT Framework**

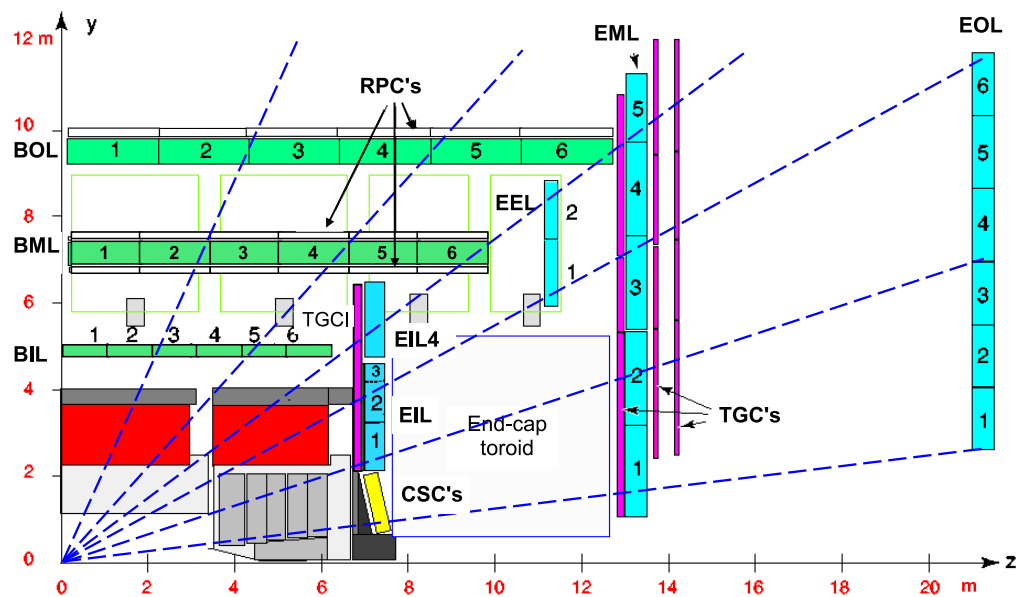


Figure 4.13: Plan view of quarter-section of the ATLAS muon system.

854 **Chapter 5**

855 **Calibration of the Soft Muon
856 Tagger for 2012 ATLAS Data**

857 High-energy physics relies heavily on the use of simulated data to inform the development
858 of analysis techniques. It is thus paramount that the simulation reflect nature as closely
859 as possible. However the simulation does not accurately predict conditions within the
860 detector and the effects on the muon reconstruction and the quality of the fit between the
861 inner detector tracks and muon spectrometer tracks which is represented in the χ^2_{match} .
862 Instead the difference between simulation and data is quantified and taken into account.
863 This process is known as calibration. In the case of the muon reconstruction method
864 and the χ^2_{match} tagger it is important that the difference in efficiency between MC and
865 data be accounted for. This is done by constructing a scale factor, defined in this case
866 by:

$$\kappa_{\chi^2_{\text{match}}} = \frac{\epsilon_{\chi^2_{\text{match}}}^{\text{Data}}}{\epsilon_{\chi^2_{\text{match}}}^{\text{MC}}} \quad (5.1)$$

867 One of the advantages of using the χ^2_{match} tagger over other forms of tagging is that
868 the presence of a jet is not required to measure the χ^2_{match} of a muon. This means that
869 the calibration can be performed on isolated muons such as those from $J/\psi \rightarrow \mu\mu$ or
870 $Z \rightarrow \mu\mu$ using the so called tag and probe method. This calibration relies on muons with
871 low p_T from J/ψ decays. As the χ^2_{match} is a characteristic of combined and therefore

872 reconstructed muons,

873 The tag and probe method used in this calibration is defined as follows. One recon-
874 structed combined muon is designated as the Tag, this muon must pass a stringent set
875 of cuts implying that this is indeed a muon from a J/ψ . The second muon which is des-
876 ignated as the Probe is constructed from an inner detector (ID) only. To ensure that the
877 Probe is the second muon from the J/ψ decay, the invariant mass of the combined tag
878 and probe system is required to be within a mass window centered around the true J/ψ
879 mass. The complete selection used in the calibration is detailed in Section 5.1. These
880 Probes are then used to measure the reconstruction efficiency and the χ^2_{match} tagger
881 efficiency as described in Sections 5.2 and 5.3.

882 The tag and probe method used here is based on a previous calibration of the χ^2_{match}
883 tagger performed on 2011 ATLAS collision data outlined in This analysis differs from
884 the 2011 calibration in several ways these will be highlighted and explained.

885 **5.0.1 Software, Collision Data and Simulated samples**

886 The tag and probe method used here was implemented using the ROOT analysis frame-
887 work.

888 The calibration was performed on a dataset made of those luminosity blocks selected
889 by the recommended standard Good Runs List (GRL) which corresponds to all pp col-
890 lision periods in 2012. The GRL selects only those luminosity blocks where detector
891 conditions are appropriate for physics data-taking. This includes all relevant detector
892 components being operational and that stable beam conditions have been achieved. The
893 datasets are part of the 2013 summer reprocessing (processing tag p1328) corresponding
894 to data taken in periods A through to L, excluding periods F and J.

895 The efficiency scale factor is measured against a sample containing almost 10 million
896 $J/\psi \rightarrow \mu\mu$ events. At event generation filters are applied so the sample only contains
897 events where both muons have a transverse momentum of at least 4 GeV and they
898 must lie within the pseudo-rapidity range $|\eta| < 2.5$. This selection matches the object
899 selection used by most analyses as recommended by the Muon Combined Performance
900 (MCP) group.

5.1 Tag and Probe Selection

A tag and probe method was chosen to measure the efficiency of muon reconstruction and the χ^2_{match} tagger. The tag and probe method allows for the measurement of the performance of selection criteria or algorithms by exploiting well known decays. By creating a sample of objects, in this case muons, on which to apply the aforementioned selection criteria, it is possible to study these algorithms.

The muon reconstruction algorithm examines various Inner Detector (ID) tracks and Muon Spectrometer (MS) tracks and makes a determination as to whether said track is produced by muon or not. To measure the performance of the muon reconstruction algorithm a sample of ID tracks which originate from the J/ψ decay and are thus very likely to be a real muon is constructed. This is done in the following way:

First, require the presence of a combined STACO muon which passes a very stringent selection. This strongly implies that this is a real muon and thus is labelled as the Tag. Additionally a very loose selection is applied to all ID tracks. These are known as candidate Probes. Pairs of tag and probes are then formed by requiring that the combined invariant mass lie within a J/ψ mass window and the pair pass additional pairing cuts. This then implies that the Probe is likely the other muon from the J/ψ decay and as such is a suitable test-bed to measure the performance of the muon reconstruction algorithm. Note that all selection criteria are detailed and explained in Section 5.1.2

After selecting a sample of probes the performance of the algorithm is estimated by measuring the proportion of probe candidates which are selected by the algorithm. In other words the performance is estimated by counting the number of muons which are reconstructed given that the ID track is very likely to be a real muon. Probes which are reconstructed into combined STACO muons are labelled as muon probes. The performance of the χ^2_{match} tagger is estimated in a similar manner, by measuring the proportion of combined muon probes which pass the SMT selection.

928 **5.1.1 Trigger requirements**

929 In order for an event to be included in the analysis it must pass at least one of the
 930 trigger chains listed in Appendix A. For the sake of brevity only the primary trigger
 931 (`EF_mu6_Trk_Jpsi_loose`) which contributes the majority of events is described here.

932 As stated in the trigger name this is an Event Filter trigger which requires the
 933 presence of a muon with a momentum of at least 6 GeV and an ID track whose combined
 934 invariant mass lies within a J/ψ mass window of $2.6 \text{ GeV} < m_{\text{inv}} < 3.6 \text{ GeV}$. This loose
 935 mass window contains the entirety of the J/ψ peak in all examined p_T and η ranges
 936 as well as additional side bands to allow for background removal. Note the omission of
 937 double muon triggers to avoid introducing a bias by specifically selecting events with
 938 two good muons.

939 Also note that while all triggers are operational in all periods, most are heavily
 940 prescaled and the prescale is period dependent. This does not have a first-order effect
 941 on the measurement since only ratios are compared between collision data and MC.

942 **5.1.2 Selection Cuts**

943 The selection criteria for tags, probes, muon probes and SMT muons are listed and
 944 detailed below. Note that all cuts are applied on the kinematic properties measured
 945 in the ID due to its improved resolution unless it is not possible as in the case of the
 946 χ^2_{DoF} which is a combined MS and ID property. Also note that all objects must pass
 947 a selection criteria collectively referred to as MCP cuts. These are tracking quality cuts
 948 which require a certain number of detector elements be active to ensure good tracking.

949 These cuts are listed in

950 The muon tag selection criteria are defined in the list below:

951 • MCP cuts

952 • STAC0 collection

953 • Combined muon

954 • $p_T > 4 \text{ GeV}$

955 • $|\eta| < 2.5$

- 956 • $|d_0| < 0.3$ mm and $|z_0| < 1.5$ mm
 957 • $|d_0/\sigma_{d_0}| < 3$ and $|z_0/\sigma_{z_0}| < 3$
 958 • Fired at least one of the relevant triggers (see Appendix A)

959 Included are cuts on the muon impact parameter (IP) d_0 and z_0 . These are defined
 960 as the distance of closest approach of the ID track to the primary interaction vertex in
 961 the transverse and longitudinal planes, respectively. Additionally cuts on the absolute
 962 values of IP significances are also implemented. The significance of the impact parameter
 963 is defined as d_0/σ_{d_0} where σ_{IP} is the standard deviation of the impact parameter. These
 964 cuts are designed to ensure that the muon selected originates near the primary vertex
 965 and thus from a prompt J/ψ from the primary collision. Note that non-prompt J/ψ can
 966 be produced in the decay of b hadrons. Finally note that the tag muon must match the
 967 trigger object which selected this event.

968 The probe selection is a subset of the tag selection and only requires an ID track
 969 with $|\eta| < 2.5$ and $p_T < 4$ GeV. The pairing cuts are shown below:

- 970 • $2 \text{ GeV} \leq m_{\text{inv}} \leq 4 \text{ GeV}$
 971 • Probe charge is opposite the tag charge
 972 • $0.4 < \Delta R(\text{tag}, \text{probe}) < 3.5$
 973 • $\Delta z_0(\text{tag}, \text{probe}) < 0.2$ mm

974 The probe and the tag are required to be fairly well separated to avoid the momentum
 975 of the tag from entering the isolation cone of the probe. In the 2011 calibration analysis
 976 the track of the tag and the probe are refit to a common vertex and the quality of
 977 the refit, expressed by the χ^2 is a part of the pairing criteria. This criteria is present
 978 to reduce the effects of pile-up on the measurement, by ensuring both objects have a
 979 common origin. Since the data format used for this analysis is a derived form of that
 980 used in 2011 it is not possible to perform such a refit. Instead the difference between
 981 the z_0 of the tag and the probe is used.

982 The **STAC0** reconstruction efficiency is not measured by applying the algorithm on
 983 the probe collection but rather a probe is said to be a muon probe if it matches a com-
 984 bined muon from the **STAC0** collection. This is done by requiring the angular separation
 985 between the probe and the **STAC0** muon be less than 0.001. Probes which are matched
 986 become the numerator of the reconstruction efficiency and the denominator is defined
 987 as the number of probes:

$$\epsilon = \frac{N_{\text{muon probe}}}{N_{\text{probe}}}$$

988 A muon probe is said to be an SMT muon if it passes the following selection, which
 989 matches the muon cuts defined in Section 6.1. Note in particular the main component
 990 of the soft muon tagger, the cut on $\chi^2_{\text{match}}/N_{\text{dof}} < 3.2$, the distribution of the χ^2_{Dof} is
 991 shown in Fig. 5.1

- 992 • $|d_0| < 3 \text{ mm}$
- 993 • $|z_0 \sin(\theta)| < 3$
- 994 • $\chi^2_{\text{match}}/N_{\text{dof}} < 3.2$

995 Those muon probes which pass the SMT selection are the numerator of the SMT
 996 efficiency and the denominator is defined as the number of muon probes:

$$\epsilon = \frac{N_{\text{SMT}}}{N_{\text{muon probe}}}$$

997 **5.2 Invariant mass fitting**

998 The pairing criteria are very effective at selecting J/ψ events, however non- J/ψ back-
 999 ground events are also pass the selection. These include combinatorial background
 1000 where the wrong tag and probe pair is constructed and Drell-Yan which appears as a
 1001 continuum below the J/ψ peak.

1002 The number of probes is extracted from a fit to the invariant mass of the dimuon
 1003 system using a composite function to accomodate for the background and the gaussian-
 1004 like J/ψ peak.

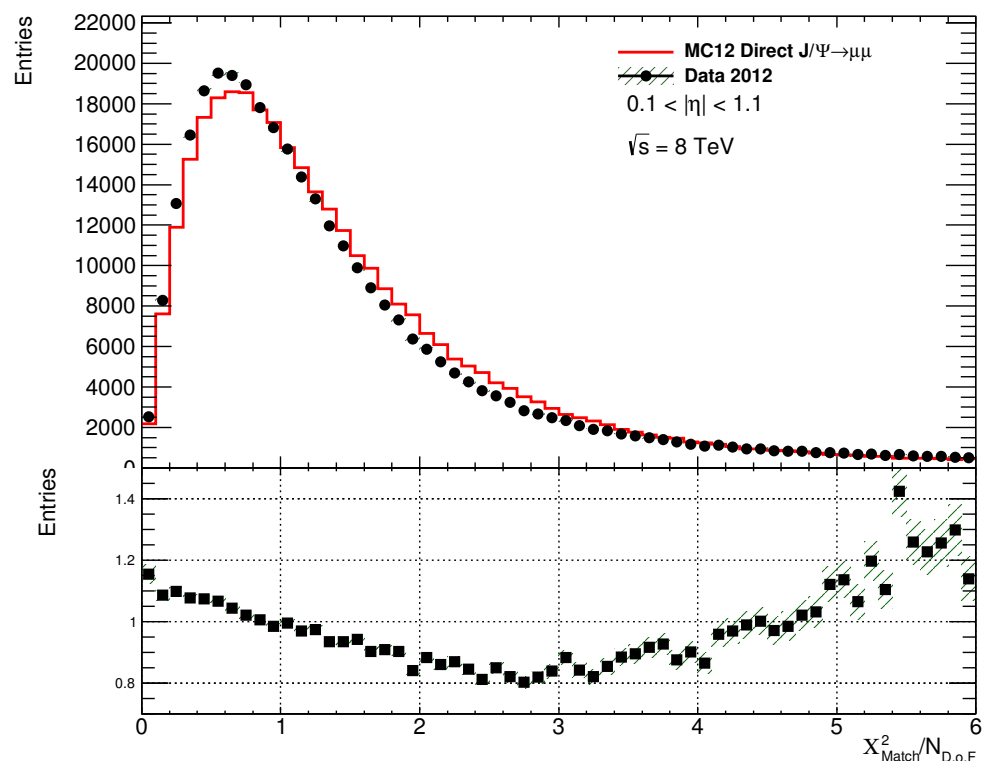


Figure 5.1: The distribution of $\chi^2_{\text{match}} / N_{\text{dof}}$ for all muon probes for ATLAS collision data and prompt J/ψ Monte Carlo simulation.

1005 The invariant mass peak of the J/ψ is modelled by a gaussian distribution while the
 1006 background distribution is modelled by a quadratic. The invariant mass distribution is
 1007 fit by a sum of the two functions.

1008 To avoid the first-order effects of signal mis-modelling from the fit of the J/ψ peak,
 1009 the yield is obtained from the integral of the measured invariant mass distribution sub-
 1010 tracting the background contribution from the integral of the fit to the background.
 1011 The integration is performed in a window with a width based on the width of the fitted
 1012 J/ψ peak. The integration window marked in Fig. 5.2 corresponds to three times the
 1013 width of the peak or simply 3σ . Additionally note the composite fit line as well as the
 1014 background-only distribution and the implied signal gaussian peak.

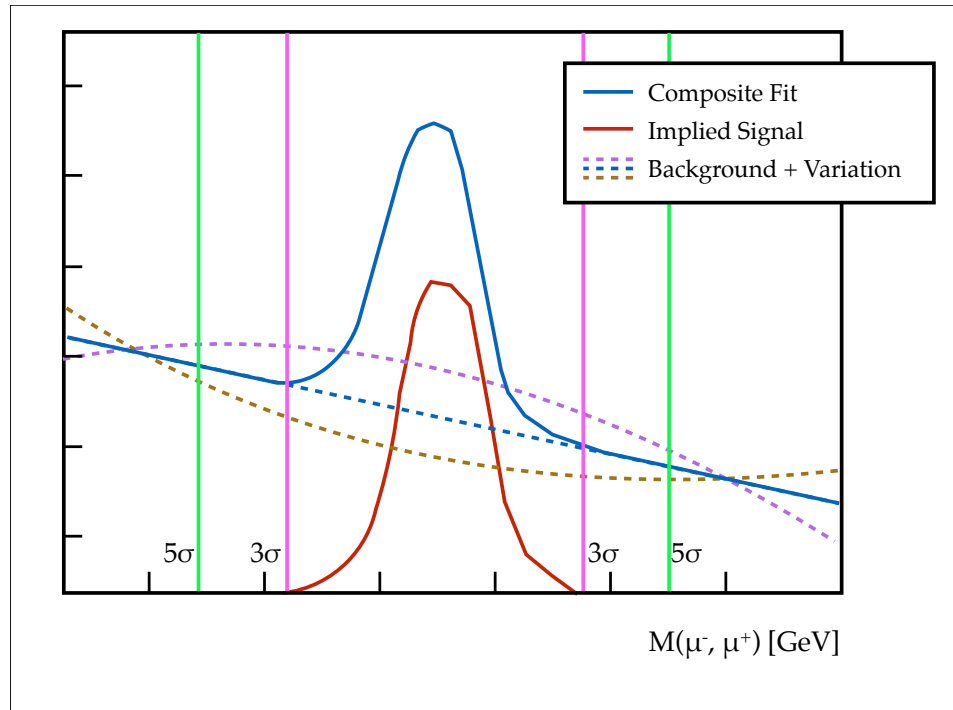


Figure 5.2: A diagram of the various components of the fit procedure. The composite fit is shown along with the corresponding implied signal and background. The two variations of the background shape are also shown.

1015 **5.2.1 Uncertainty Measurement**

1016 The uncertainty on the efficiency is made of three components. First, the statistical
 1017 uncertainty on the efficiency is estimated as a Binomial error:

$$\delta\epsilon = \sqrt{\frac{\epsilon \times (1 - \epsilon)}{N}} \quad (5.2)$$

1018 Where ϵ is the measured efficiency and N is, in this case the denominator of the
 1019 efficiency measured.

1020 Secondly, an uncertainty is associated with the fit to the background. This is done
 1021 by taking the largest upward and downward fluctuations of the background by the un-
 1022 certainty on the fit parameters of the background, and obtaining the maximum upward
 1023 and downward effects on the efficiency. After the fit of the composite function is carried
 1024 out, a downward variation of the background is defined as:

$$f(x) = a_{\min}x^2 + b_{\max}x + c_{\min}, \text{ where } p_{\max/\min} = p_{\text{central}} \pm \sigma_p \quad (5.3)$$

1025 Here the maximum and minimum of a parameter is obtained by varying the central
 1026 value by the uncertainty obtained from the fit. The upward variation of the background
 1027 fit is thus the opposite, defined as:

$$f(x) = a_{\max}x^2 + b_{\min}x + c_{\max} \quad (5.4)$$

1028 These background variation then result in the maximum deviation from the nominal
 1029 integral. Again Fig. 5.2 shows these two variations¹. The uncertainty on the efficiency is
 1030 then determined by obtaining the maximum efficiency in both directions. If the nominal
 1031 efficiency is defined as:

$$\epsilon_{\text{nominal}} = \frac{N_{\text{numerator}}}{N_{\text{denominator}}} \quad (5.5)$$

1032 Then the variations are defined as follows:

$$\epsilon_{\text{up}} = \frac{N_{\text{numerator}}^{\text{down}}}{N_{\text{denominator}}^{\text{nominal}}}, \quad \epsilon_{\text{down}} = \frac{N_{\text{numerator}}^{\text{nominal}}}{N_{\text{denominator}}^{\text{up}}} \quad (5.6)$$

1033 Finally the uncertainty on the background is given by adding the differences between
 1034 ϵ_{up} and ϵ_{down} and the nominal efficiency, in quadrature:

¹The variation shown in the diagram is very exaggerated and meant for illustration purposes

$$\sigma_{\text{bkg}} = \sqrt{|\epsilon_{\text{up}} - \epsilon|^2 + |\epsilon_{\text{down}} - \epsilon|^2} \quad (5.7)$$

1035 The final component of the uncertainty is constructed by varying the integration
 1036 window. The nominal value is defined as 3σ away from the center of the fitted gaussian,
 1037 where again σ is the FWHM of the same fitted gaussian. An uncertainty is constructed
 1038 by measuring the efficiency with a wide integration window corresponding to 5σ . The
 1039 integration window uncertainty is defined as:

$$\sigma_{\text{window}} = |\epsilon_{5\sigma} - \epsilon_{3\sigma}| \quad (5.8)$$

1040 Finally, the total uncertainty on the efficiency is given by the sum in quadrature of
 1041 the all uncertainty components. The uncertainty on the efficiency is then carried over
 1042 to the scale factor determination.

1043 An example of the fitting procedure applied is shown in Fig. 5.3 for both tag and
 1044 probes at probe level and at muon probe level. Note that as expected the muon probe
 1045 contains far less background.

1046 5.3 Efficiencies

1047 The efficiency is monitored as a function of a variety of kinematic variables, including
 1048 isolation variables, transverse momentum and angular position of the probe.

1049 5.3.1 Isolation dependence

1050 The muons from J/ψ used in this calibration are produced in isolation, there is very little
 1051 energetic activity surrounding them in the detector. In contrast muons from semileptonic
 1052 decay of b -quarks in $t\bar{t}$ events are produced amongst the numerous components of the
 1053 b -jets. Thus it is important to ensure that the performance of the χ^2_{match} tagger is not
 1054 affected by the isolation of the muon for a calibration on J/ψ events to be applicable.
 1055 In this calibration as, in the 2011 analysis nine isolation variables are considered. The
 1056 so-called etcone20, 30 and 40 correspond to the transverse energy surrounding the muon
 1057 in a cone of size $\Delta R = 0.2, 0.3, 0.4$ respectively. Additionally ptcone20, 30 and 40

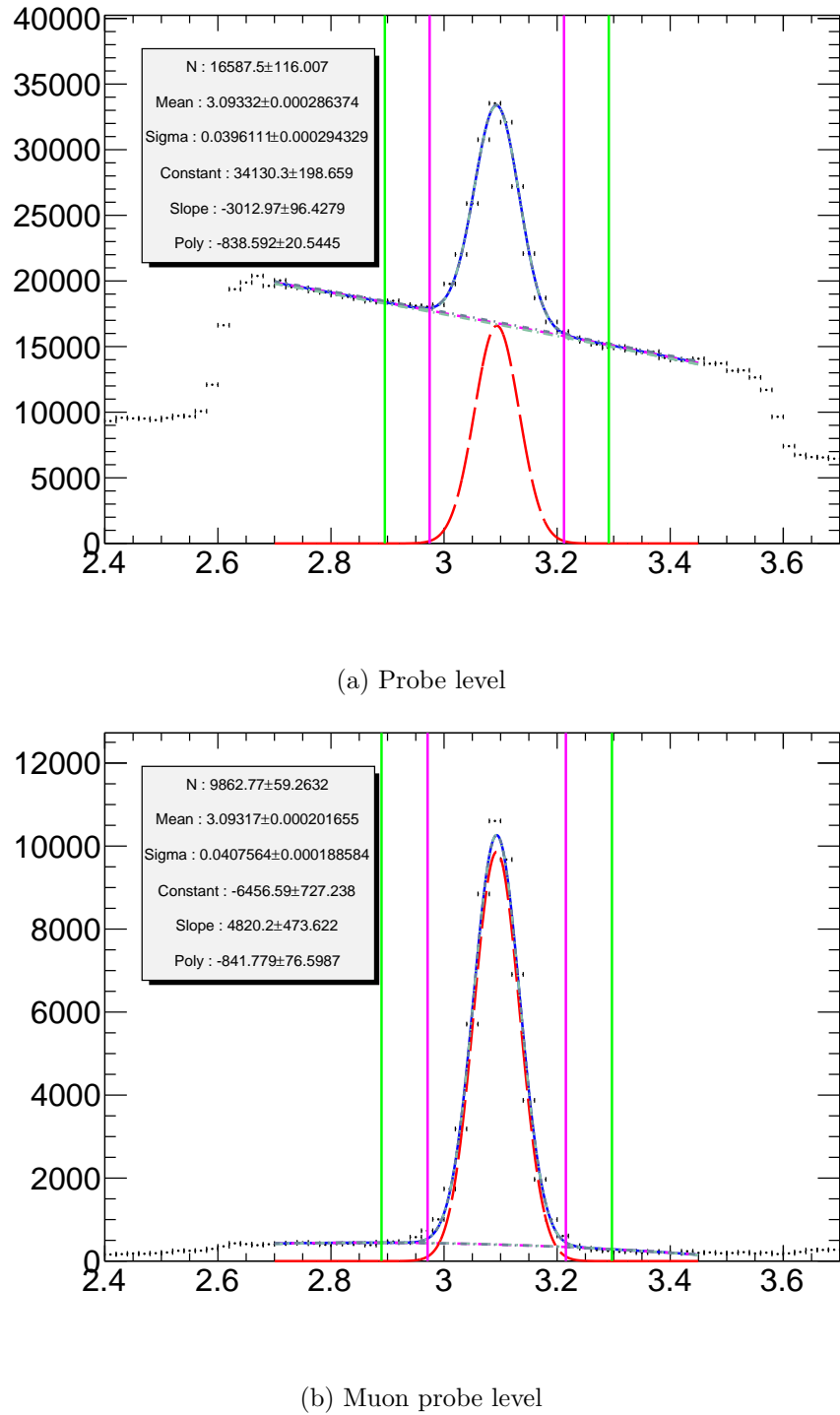


Figure 5.3: Invariant mass distributions of tag and probe pairs at a) probe level and at b) muon probe level in collision data. Note the various components of the fit as well as the variations on the background fits and the 3σ and 5σ integration windows used for systematics. Note the fit parameters and their respective uncertainties

and nucone20, 30, 40 correspond to the sum of transverse momentum and the number of tracks surrounding the muon, respectively. All nine isolation variables exclude the muon itself in a cone of size 0.1 and include various corrections for known energy losses, momentum leakages between adjacent clusters in the detector and the effects of pile-up.

As in the 2011 analysis there appears to be no dependence of the scale factor on any of the isolation variables examined as can be seen from Figures 5.4, 5.5 and 5.6.

The dependence on each isolation variable is measured in a range dictated by the available statistics. Given the isolated nature of muons in J/ψ events limits the number of muons available at higher p_T/et /nucone values.

5.3.2 2011 Calibration

5.3.3 Efficiency Binning

The efficiencies are measured with respect to pseudorapidity and across the $|\eta|$ range of the ATLAS detector in regions defined in Table 5.1. Note that the η regions are labeled A and C to denote the positive and negative η sections of the detector. The binning in other variables is determined by the amount of statistics available to allow for the fitting procedure to produce good and stable results. The binning in p_T was chosen as: 4-5, 5-6, 6-7, 7-8, 8-10, 10-12, 12-14, 14-16 and 16-20 GeV.

Table 5.1: Pseudorapidity regions of the ATLAS detector

$ \eta $ range	Name
$0.0 < \eta < 0.1$	Crack
$0.1 < \eta < 1.1$	Barrel
$1.1 < \eta < 1.3$	Transition
$1.3 < \eta < 2.0$	Endcap
$2.0 < \eta < 2.5$	Forward

5.3.4 Results

The efficiency is presented as a function of η , ϕ and p_T . Figure 5.7 shows the χ^2_{match} efficiency with respect to the spatial variables of the probe. Note that as with the 2011 analysis the efficiency exhibits no dependence on ϕ and an asymmetric dependence on η particularly in the Forward regions of the detector. Note that as expected there is a

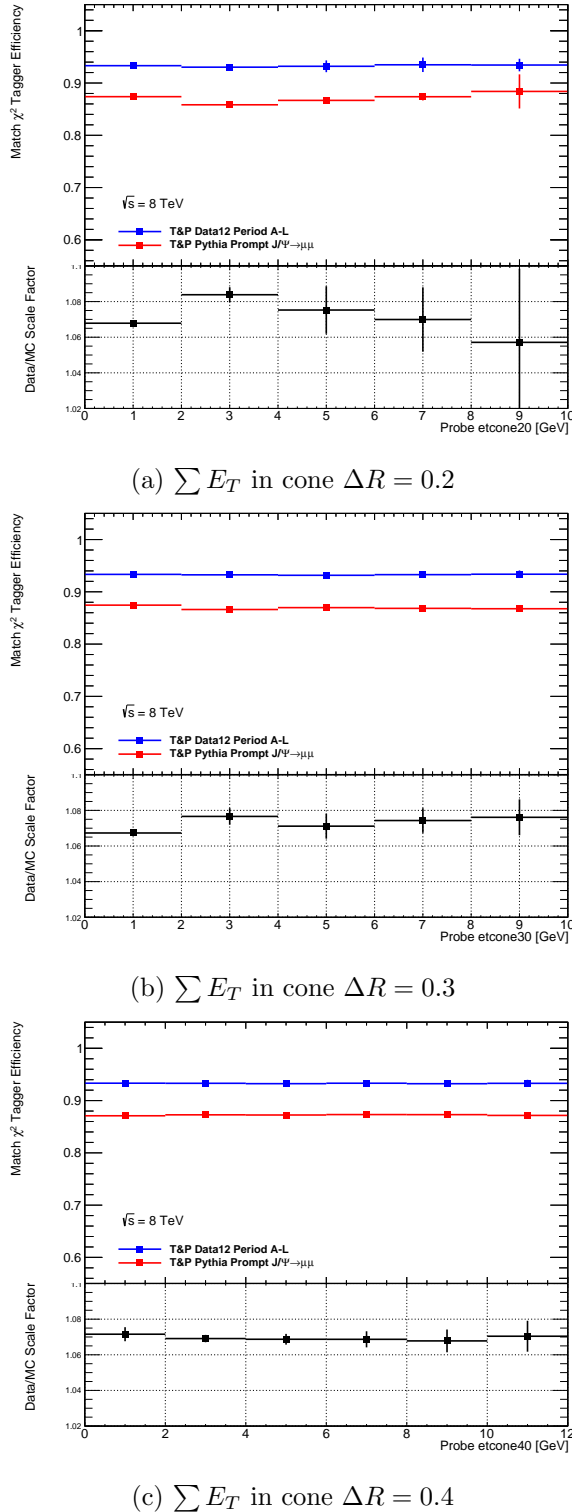


Figure 5.4: χ^2_{DoF} efficiencies and scale factor with respect to $\sum E_T$.

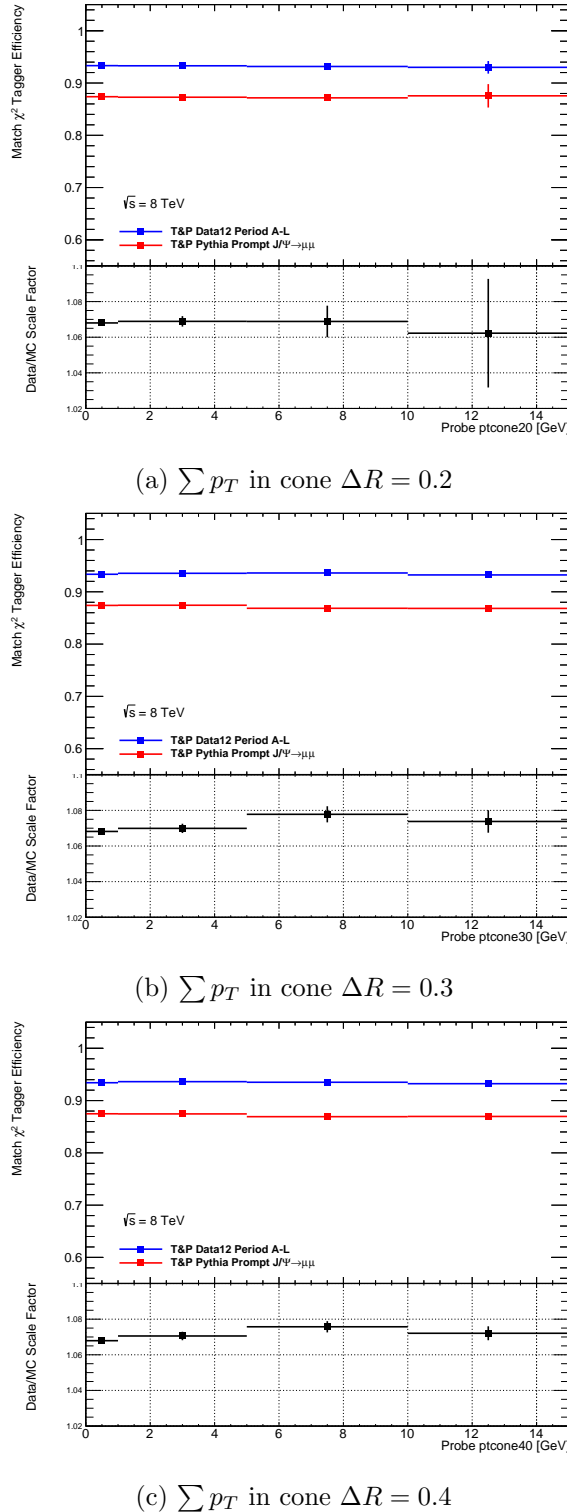


Figure 5.5: χ^2_{DoF} efficiencies and scale factor with respect to $\sum p_T$.

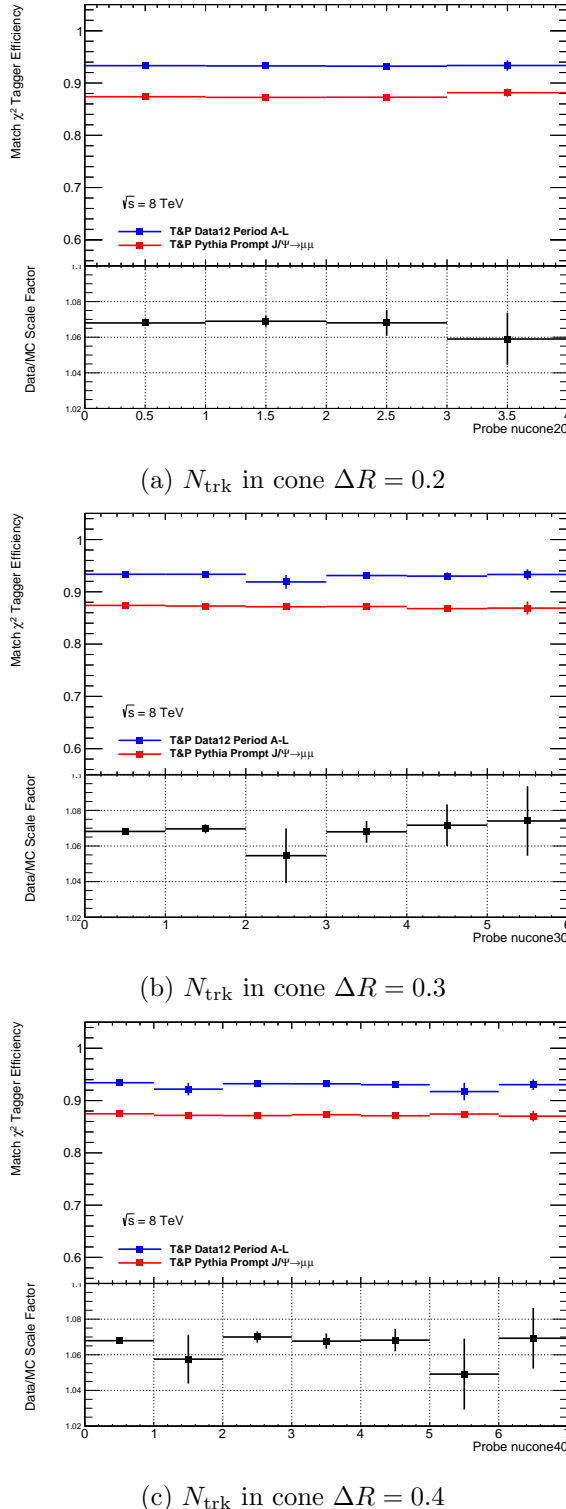


Figure 5.6: χ^2_{DoF} efficiencies and scale factor with respect various isolation variables.

- 1080 strong dependence on the transverse momentum of the muon probe as shown in Fig.5.8.
 1081 As in the 2011 analysis it was decided to bin the scale factor as a function of η and p_T .
 1082 The scale factors and efficiencies are presented in the next pages. The scale factors and
 1083 their uncertainties are summarized in Table 5.2.

Table 5.2: Data/MC Scale Factors for 2012 Data in all five regions of the detector as a function of p_T . The uncertainties include systematic and statistical components as described in Section 5.2.1

Side A (Positive η)					
p_T range	Crack A	Barrel A	Transition A	Endcap A	Forward A
4-5 GeV	1.051 ± 0.016	1.053 ± 0.005	1.046 ± 0.019	1.061 ± 0.011	1.090 ± 0.018
5-6 GeV	1.050 ± 0.007	1.058 ± 0.004	1.057 ± 0.019	1.062 ± 0.011	1.103 ± 0.020
6-7 GeV	1.068 ± 0.008	1.065 ± 0.003	1.070 ± 0.015	1.065 ± 0.008	1.134 ± 0.019
7-8 GeV	1.061 ± 0.018	1.063 ± 0.006	1.064 ± 0.017	1.061 ± 0.010	1.140 ± 0.024
8-10 GeV	1.061 ± 0.014	1.063 ± 0.007	1.068 ± 0.016	1.052 ± 0.014	1.167 ± 0.023
10-12 GeV	1.060 ± 0.042	1.070 ± 0.006	1.064 ± 0.026	1.058 ± 0.016	1.175 ± 0.038
12-14 GeV	1.061 ± 0.050	1.064 ± 0.010	1.067 ± 0.037	1.057 ± 0.021	1.190 ± 0.057
14-16 GeV	1.062 ± 0.087	1.068 ± 0.015	1.078 ± 0.054	1.067 ± 0.031	1.218 ± 0.064
16-20 GeV	1.062 ± 0.087	1.068 ± 0.015	1.078 ± 0.054	1.067 ± 0.031	1.218 ± 0.064

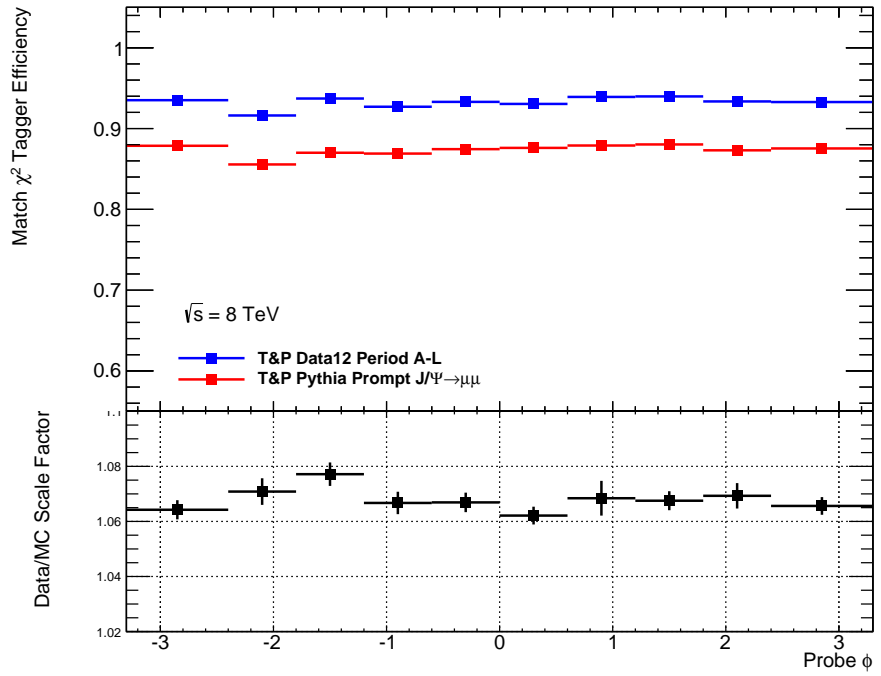
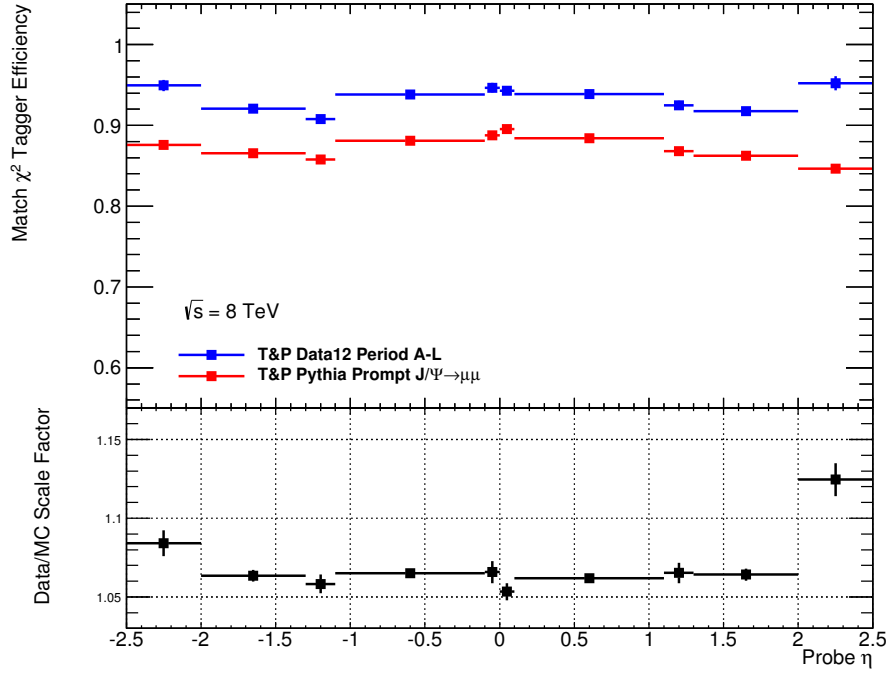
(a) For the positive η regions

Side C (Negative η)					
p_T range	Crack	Barrel	Transition	Endcap	Forward
4-5 GeV	1.044 ± 0.016	1.055 ± 0.005	1.054 ± 0.017	1.056 ± 0.009	1.068 ± 0.018
5-6 GeV	1.069 ± 0.013	1.057 ± 0.004	1.050 ± 0.016	1.062 ± 0.010	1.084 ± 0.020
6-7 GeV	1.080 ± 0.016	1.068 ± 0.004	1.065 ± 0.008	1.066 ± 0.008	1.089 ± 0.018
7-8 GeV	1.064 ± 0.021	1.068 ± 0.004	1.063 ± 0.016	1.066 ± 0.010	1.095 ± 0.022
8-10 GeV	1.071 ± 0.015	1.067 ± 0.005	1.045 ± 0.015	1.061 ± 0.009	1.107 ± 0.022
10-12 GeV	1.084 ± 0.030	1.073 ± 0.007	1.085 ± 0.022	1.061 ± 0.015	1.113 ± 0.036
12-14 GeV	1.098 ± 0.067	1.069 ± 0.010	1.059 ± 0.031	1.040 ± 0.024	1.108 ± 0.055
14-16 GeV	1.063 ± 0.101	1.073 ± 0.015	1.076 ± 0.046	1.061 ± 0.030	1.099 ± 0.057
16-20 GeV	1.073 ± 0.149	1.088 ± 0.006	1.099 ± 0.028	1.054 ± 0.012	1.117 ± 0.043

(b) For the negative η region

1084 Dependence on d_0

- 1085 The dependence on the impact parameter d_0 was examined and no direct dependence
 1086 is observed. From Fig. 5.14 the scale factor shows no structure with respect to d_0 when
 1087 binned in p_T . Since the scale factors are already binned in η and p_T the correlation of
 1088 d_0 and p_T is already taken into account.

(a) χ^2_{match} efficiency and scale factor as a function ϕ of the probe muon(b) χ^2_{match} efficiency and scale factor as a function η of the probe muonFigure 5.7: χ^2_{match} efficiencies and scale factor with respect to the (a) ϕ and (b) η

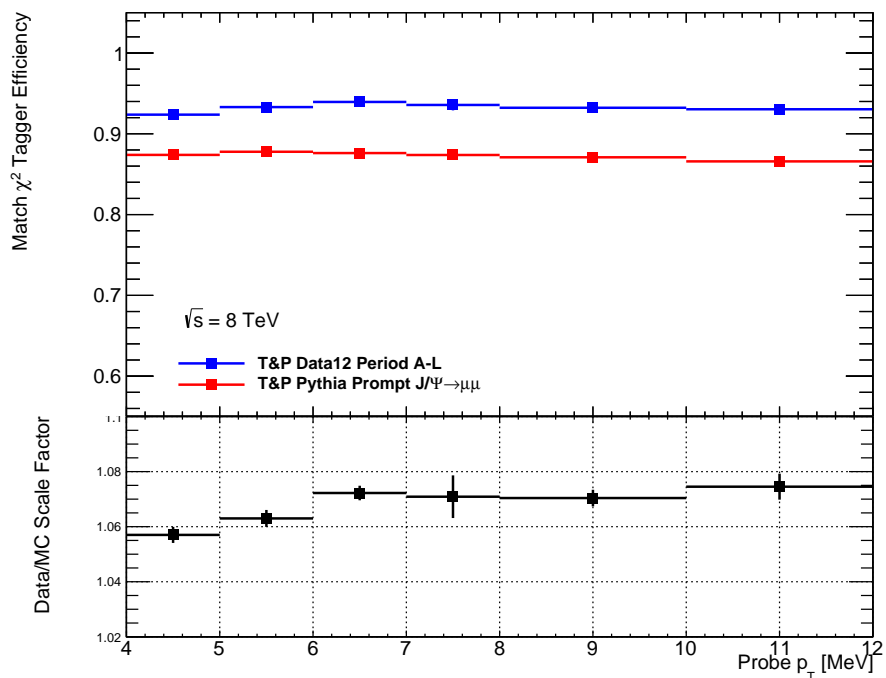


Figure 5.8: χ^2_{match} efficiencies and scale factor with respect to the transverse momentum of the muon probe

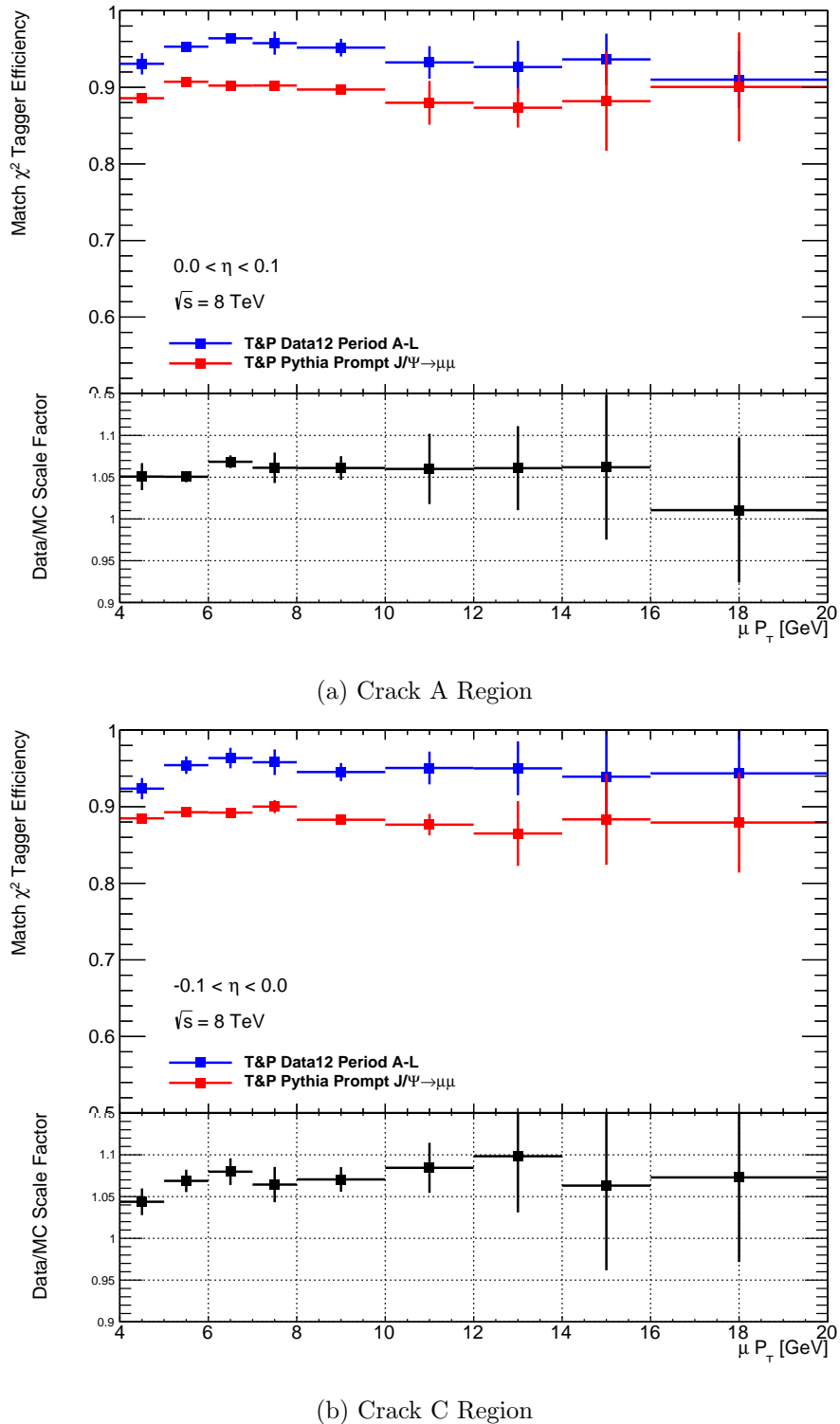


Figure 5.9: χ^2_{match} efficiencies and scale factors in the crack region of the detector for side (a) A and (b) C

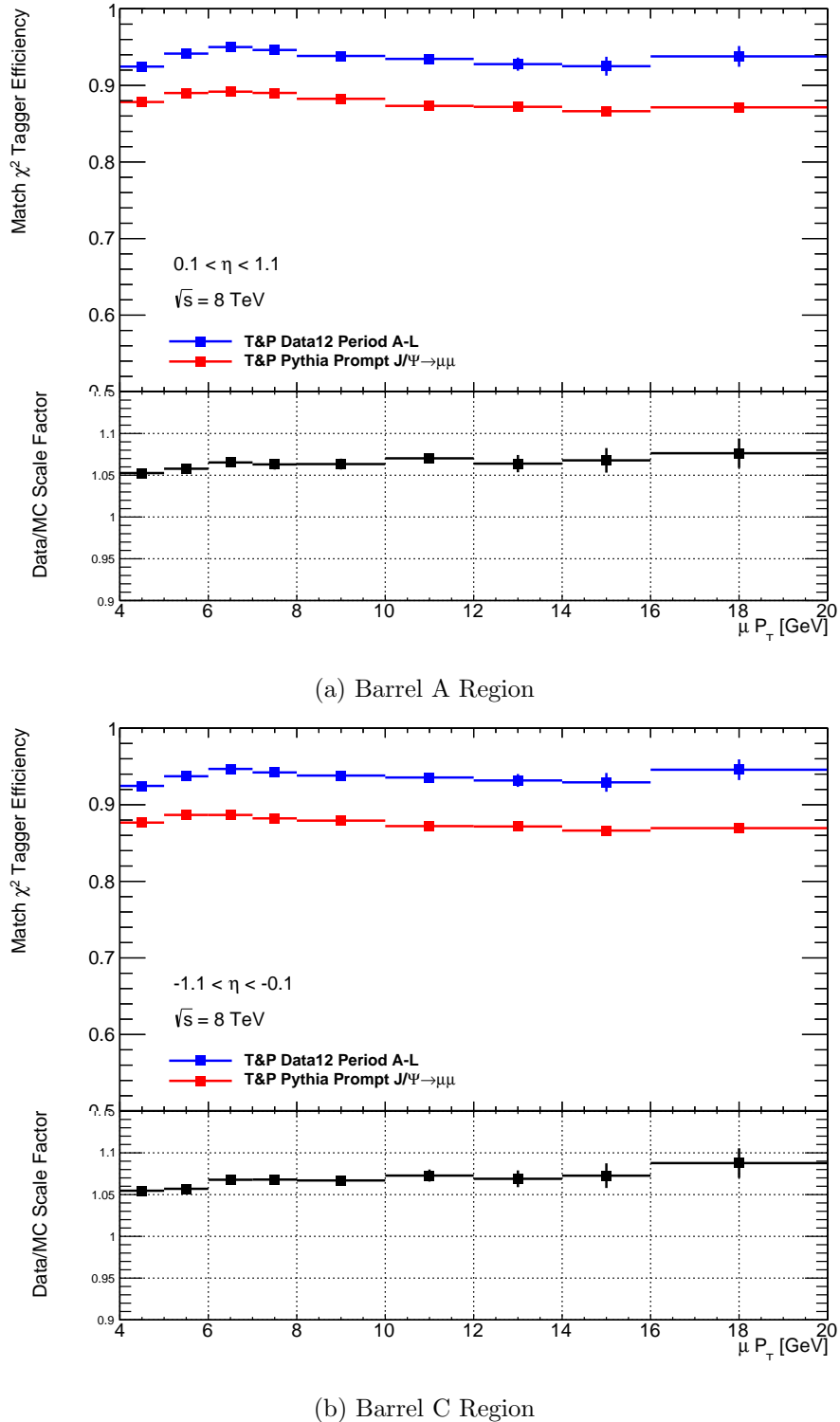


Figure 5.10: χ_{match}^2 efficiencies and scale factors in the barrel region of the detector for side (a) A and (b) C

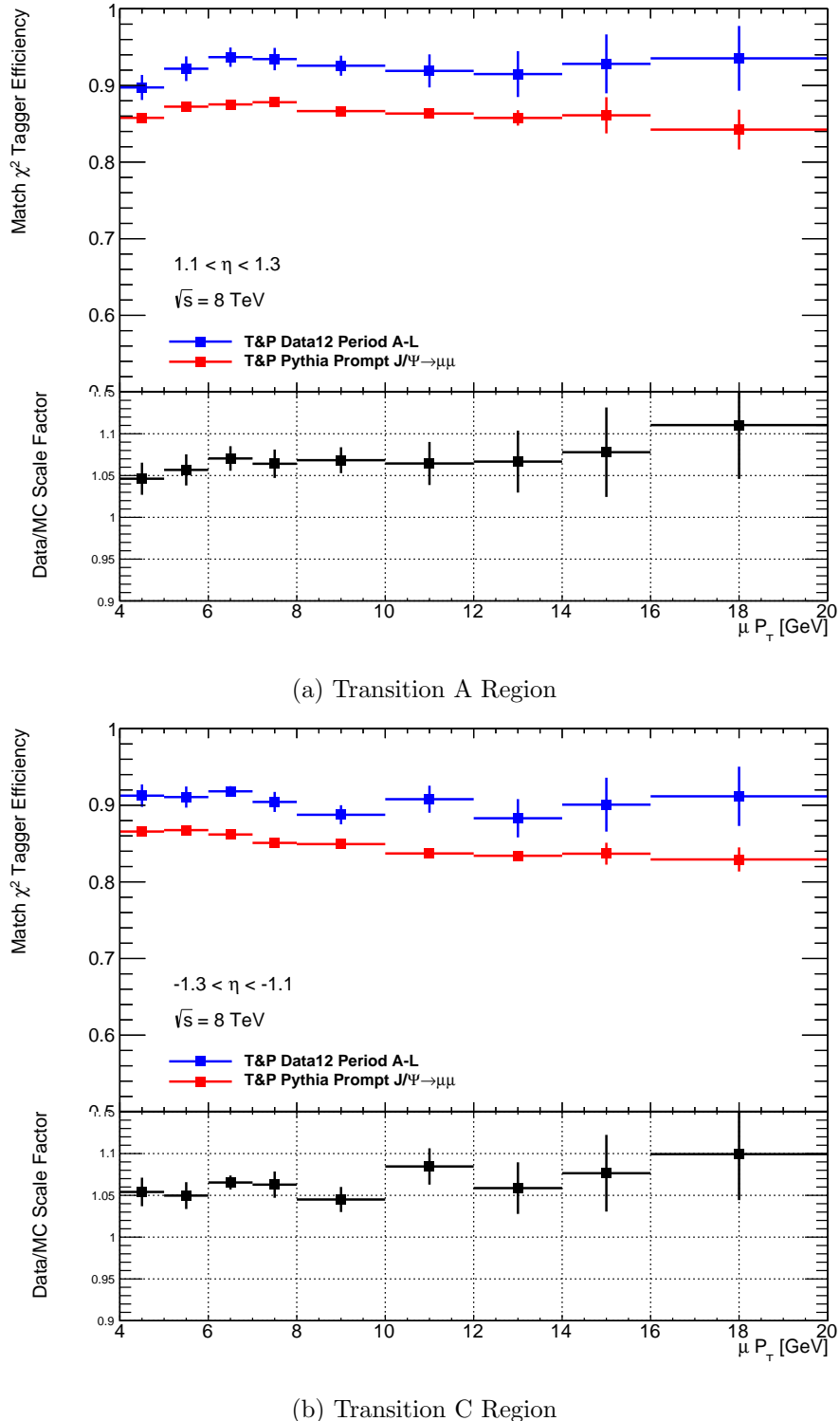


Figure 5.11: χ^2_{match} efficiencies and scale factors in the transition region of the detector for side (a) A and (b) C

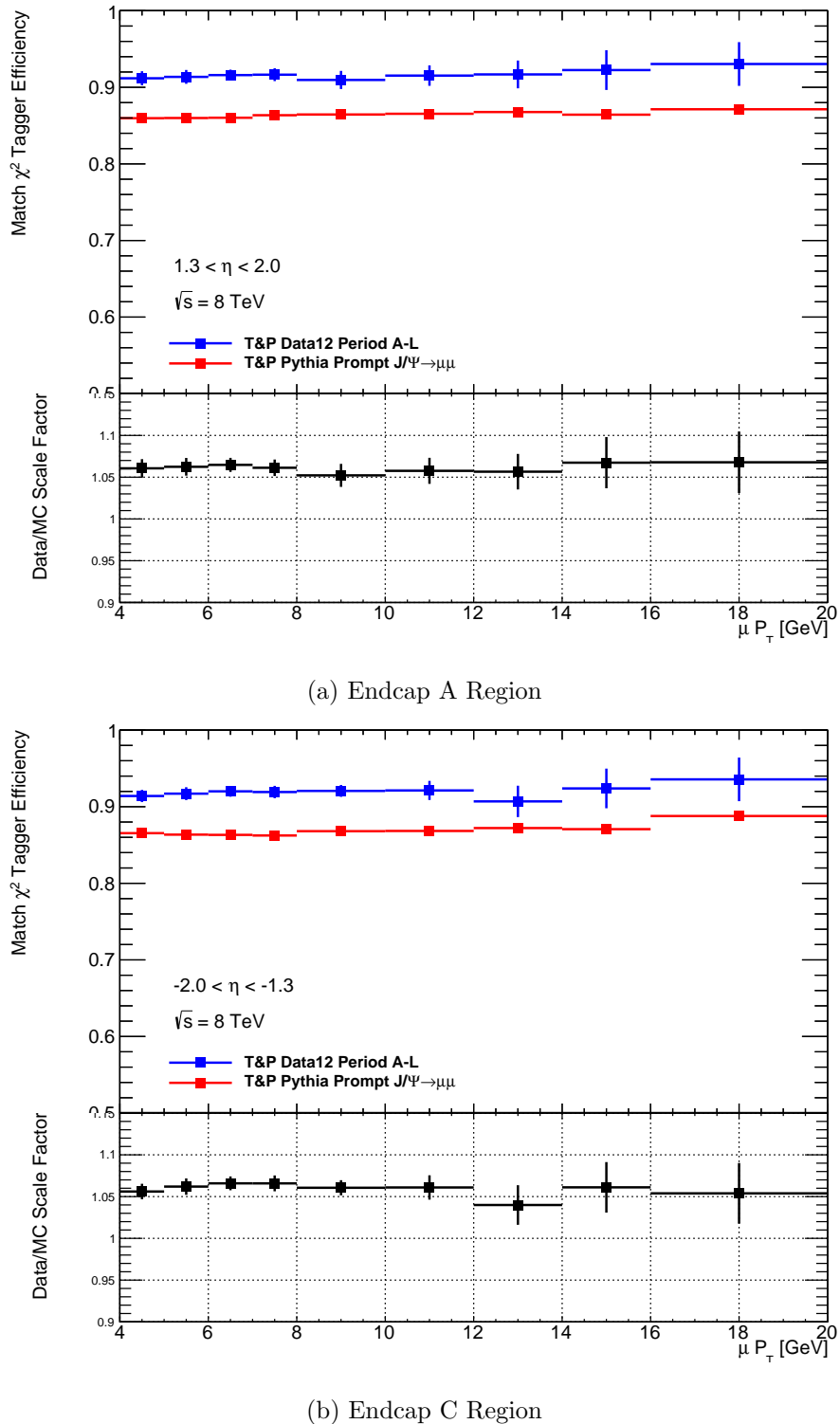


Figure 5.12: χ^2_{match} efficiencies and scale factors in the endcap region of the detector for side (a) A and (b) C

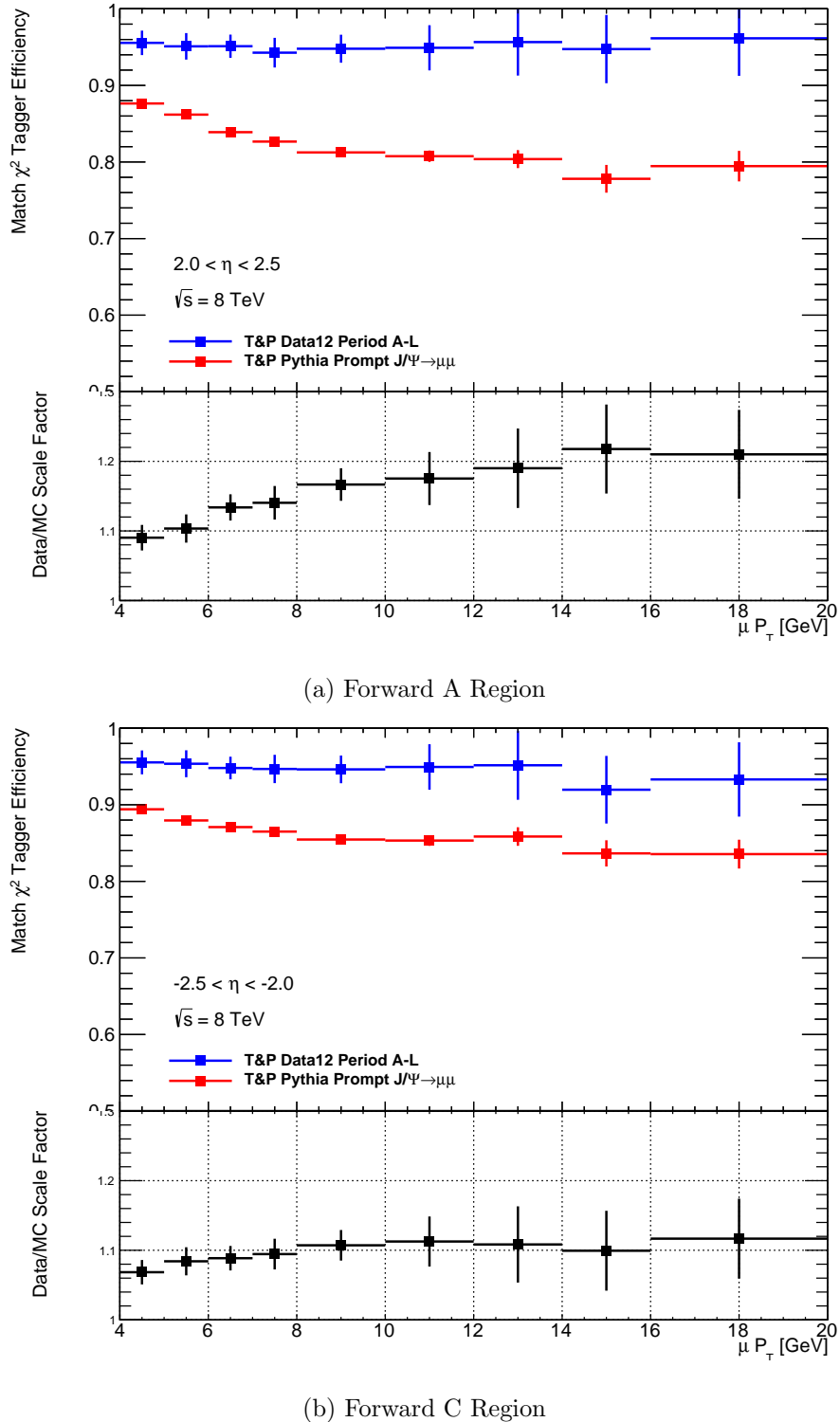


Figure 5.13: χ^2_{match} efficiencies and scale factors in the forward region of the detector for side (a) A and (b) C

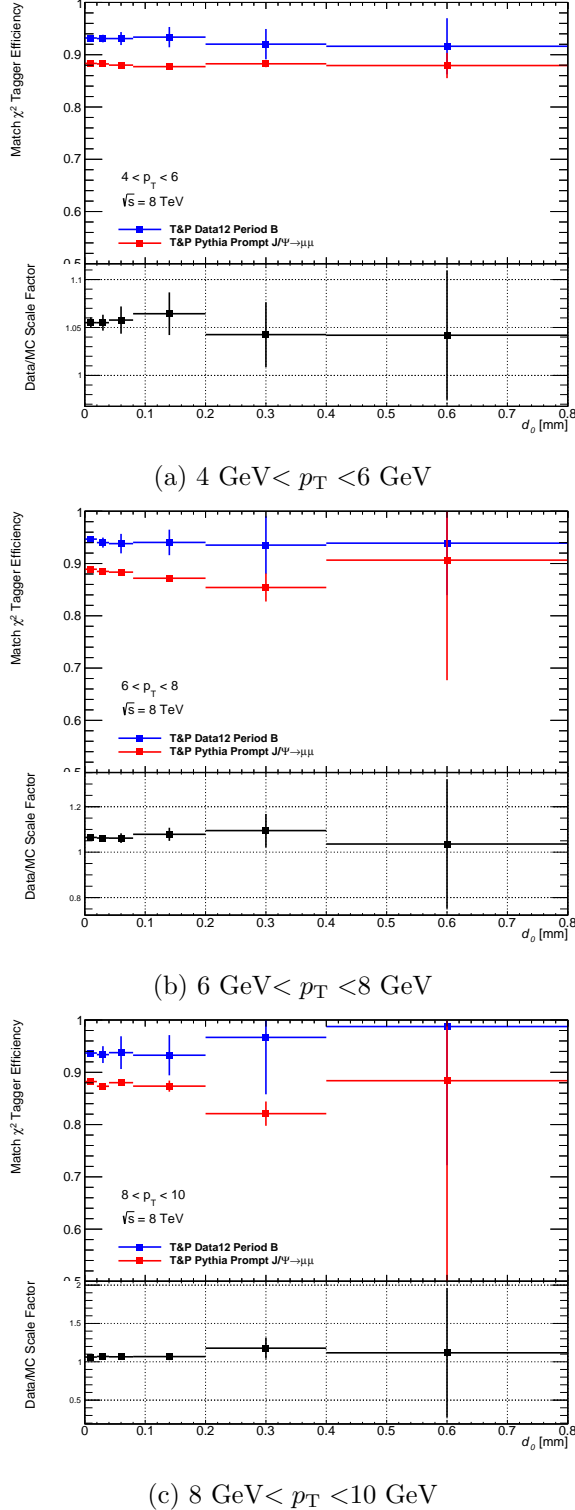


Figure 5.14: χ^2_{match} efficiencies and scale factor with respect to impact parameter d_0 for muon probes with p_T in the range (a) 4-6 GeV, (b) 6-8 GeV and (c) 8-10 GeV. The measurement was carried out only on Period B of 2012 ATLAS collision data.

1089 **Chapter 6**

1090 **$t\bar{t}$ cross-section measurement in
1091 the $\ell+$ jets channel using SMT**

1092 This section describes a $t\bar{t}$ cross-section measurement carried out the joint RHUL-QMUL
1093 SMT group.

1094 Measurement of the $t\bar{t}$ production cross-section is important for two reasons. First,
1095 the value of the $t\bar{t}$ cross-section is a powerful test of the SM and perturbative QCD.
1096 Additionally, $t\bar{t}$ events constitute a background to other analyses such as SUSY searches
1097 and Higgs boson searches and properties studies. Presented here is a measurement of
1098 the top-pair production cross-section at $\sqrt{s} = 7$ TeV in the lepton plus jets channel,
1099 with at least one of the b -quarks in the event decaying semileptonically producing a soft
1100 muon.

1101 **6.1 Soft Muon Tagger**

1102 **6.2 Data and Monte Carlo samples**

1103 **6.3 Object selection and event selection**

1104 The selection criteria used in this analysis are based on the nominal $\sqrt{s} = 7$ TeV selec-
1105 tions constructed by the ATLAS top group. Some alterations have been implemented
1106 to adapt to the usage of the χ^2_{match} -tagger instead of the standard MV1 method for b -jet

1107 tagging.

1108 6.4 Background estimation

1109 Semi-leptonic $t\bar{t}$ events have a varied final state signature that includes a lepton, mul-
1110 tiple jets including b -jets and missing energy. As a result $t\bar{t}$ analyses must take into
1111 account many different types of background including diboson, $W+\text{jets}$, $Z+\text{jets}$, single-
1112 top and multijet. Data-driven methods are used for the dominant multijet and $W+\text{jets}$
1113 backgrounds while MC is used to estimate the smaller $Z+\text{jets}$, diboson and single-top.

1114 6.4.1 Multijet in the electron channel

1115 The multijet background is a difficult background to reduce and estimate. Measure-
1116 ment of multijet events depends very strongly on detector conditions, which in turn
1117 depend on external factors which cannot be simulated. Multijet events that pass the
1118 event selection include non-isolated or misidentified electrons from photon conversion or
1119 charged hadrons. As a result, data-driven methods must be employed when estimating
1120 the amount of multijet background. This analysis makes use of two different method-
1121 ologies, The so-called matrix method is used for the central value of the estimate and
1122 the ABCD method for verification and use as a systematic.

At pretag level the multijet content in the signal region is estimated by using the matrix method. In addition to the standard electron selection a looser selection is defined. Events are categorized by whether they pass the loose or standard selection. The number of events in each category is the sum of events with “real” electrons and “fake” electrons as follows:

$$N^{\text{loose}} = N_{\text{real}}^{\text{loose}} + N_{\text{fake}}^{\text{loose}} \quad (6.1)$$

$$N^{\text{std}} = rN_{\text{real}}^{\text{loose}} + fN_{\text{fake}}^{\text{loose}} \quad (6.2)$$

1123 where r and f are the “real” and “fake” efficiencies for the loose event to also pass
1124 the standard selection. Given a measured N^{std} and N^{loose} and if f and r are known
1125 the number of events with a fake electron that passes the standard selection can be

1126 calculated as

$$N_{\text{fake}}^{\text{std}} = f N_{\text{fake}}^{\text{loose}} = f \frac{N^{\text{std}} - r N^{\text{loose}}}{(f - r)} \quad (6.3)$$

1127 The relative efficiency r is measured from an inclusive sample of $Z \rightarrow ee$ events and
 1128 f is measured from a sample of events with exactly one loose electron, at least one jet
 1129 with a $p_T > 25$ GeV and $\cancel{E}_T < 20$ GeV. An uncertainty of 50% is assigned to the pretag
 1130 estimate to cover the respective uncertainties on f and r .

1131 To derive the tagged estimate the pretag estimates are scaled by the probability of
 1132 SMT tagging an event. The tagging probability of multijet events $R_{\text{SMT}}^{\text{multijet}}$ is derived
 1133 from control regions defined by the isolation of the electron and the \cancel{E}_T cut that forms
 1134 part of the event selection, as shown in Figure 6.1.

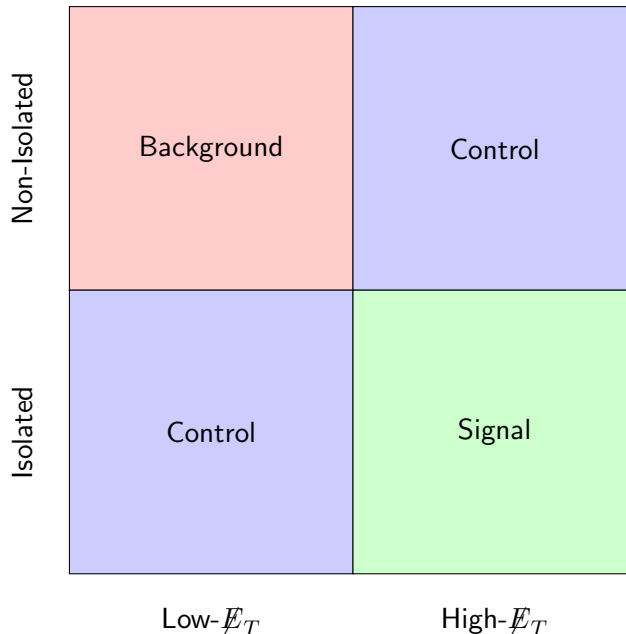


Figure 6.1: A diagram of the \cancel{E}_T -isolation phase space. Shown are the four regions as defined by the event selection.

1135 These four regions can be identified as a background-dominated region, containing
 1136 events with low- \cancel{E}_T and a non-isolated electron; a signal region, with events that pass
 1137 the event selection; and two control regions, containing events with high- \cancel{E}_T or an iso-
 1138 lated electron. The events in each of the regions then represents a different type of

1139 phenomenon. The tagging rate is simply defined as

$$R_{\text{SMT}} = \frac{N_{\text{Tagged}}}{N_{\text{Pretag}}} \quad (6.4)$$

1140 where N is the number of events in the region. Contributions from other processes
 1141 such as $W+\text{jets}$, $Z+\text{jets}$, $t\bar{t}$, single-top and diboson events are subtracted using MC
 1142 simulation. The contribution from $t\bar{t}$ is initially based on the theoretical cross-section,
 1143 an estimate for the multijet contribution is determined using this cross-section and a
 1144 new measured cross-section is obtained. The measured cross-section is used to rescale
 1145 the $t\bar{t}$ contribution and a new cross-section is obtained. This process is repeated until
 1146 the measured cross-section stabilizes, which in this case occurred after two iterations.

1147 The uncertainty on the tagging-rate contains statistical and a systematic contribu-
 1148 tions. The systematic uncertainty includes the uncertainty on the cross-section of the $t\bar{t}$
 1149 and $W+\text{jets}$ samples, uncertainty arising from the SMT tagger and finally uncertainties
 1150 arising from the BR re-weighting described a priori.

1151 The final tagging-rate is the unweighted average of all the regions. The uncertainty
 1152 is the difference between regions A and C, as this is larger than any regional uncer-
 1153 tainty. The tagging-rate and subsequently the tagged multijet background estimate is
 1154 measured on a per-jet bin basis. The tagging-rates per region for each jet-bin are shown
 1155 in Table 6.1.

Jet-bin	R_A^{SMT}	R_B^{SMT}	R_C^{SMT}	$R_{\text{AVG}}^{\text{SMT}}$
1	0.91 ± 0.03	0.82 ± 0.10	0.51 ± 0.05	0.64 ± 0.07
2	1.8 ± 0.1	2.0 ± 0.2	1.3 ± 0.1	1.5 ± 0.1
3	2.8 ± 0.1	2.5 ± 1.1	2.5 ± 0.5	2.6 ± 1.0
≥ 3	3.84 ± 0.09	3.7 ± 1.3	3.0 ± 0.8	3.2 ± 1.2
≥ 4	3.2 ± 0.1	3.7 ± 1.3	3.0 ± 0.8	3.2 ± 1.2

Table 6.1: Multijet SMT event taggin-rate(in percent) in regions A) inverted- \cancel{E}_T , non-isolated, B) High- \cancel{E}_T , non-isolated and C) low- \cancel{E}_T , isolated.

1156 **The ABCD method**

1157 The ABCD method relies on a pair of uncorrelated variables to extrapolate the amount
 1158 of multijet events from a set of control regions into the signal region. First a two-

Jet-bin	Pretag	Tagged
1	51000 ± 26000	330 ± 160
2	26000 ± 13000	400 ± 200
3	8100 ± 4100	210 ± 130
≥ 3	10800 ± 5400	330 ± 210

Table 6.2: Multijet estimates in the e+jets obtained by the jet-electron method. The uncertainties are combined statistical and systematics. A systematic uncertainty of 50% is used on the jet-electron pretag event yields [] in addition to e uncertainties obtained on $R_{\text{WGT}}^{\text{SMT}}$.

dimensional phase-space is constructed, in this case the same two variables, missing energy and isolation are used. If these two variables are uncorrelated then the following relation holds

$$N_{\text{D}}^{\text{multijet}} = \frac{N_{\text{B}}^{\text{multijet}} * N_{\text{C}}^{\text{multijet}}}{N_{\text{A}}^{\text{multijet}}} \quad (6.5)$$

where N_X^{multijet} is the number of multijet events in region X.

This allows for an estimation of the number of multijet events that pass the event selection by extrapolating from the background region into the signal region. Contributions of other processes such as $W/Z+\text{jets}$, single-top, diboson and $t\bar{t}$ to regions A,B and C are removed using MC data. Thus, the number of events in each region is measured as

$$N^{\text{multijet}} = N^{\text{data}} - N^{W+\text{jets}} - N^{Z+\text{jets}} - N^{\text{diboson}} - N^{t\bar{t}} - N^{\text{single-top}} \quad (6.6)$$

6.5 Systematic uncertainties

6.6 Results and conclusion

The final cross-section is determined by a cut-and-count method. Finally the cross-section is calculated as

$$\sigma_{t\bar{t}} = \frac{N_{\text{data}} - N_{\text{bkg}}}{\int L \, dt \times \epsilon \times \text{BR}(\text{noFullHad})} \quad (6.7)$$

The cross-section measured in the electron

₁₁₇₃ **Chapter 7**

₁₁₇₄ **Muon Tagging in a boosted $t\bar{t}$
₁₁₇₅ environment**

₁₁₇₆ The large center-of-mass energies at which collisions occur at the LHC allows for the
₁₁₇₇ production of very high mass particles. Several Beyond the SM (BSM) theories predict
₁₁₇₈ the existence of high mass particles which decay primarily top quark pairs. An example
₁₁₇₉ of hypothetical model which predict high mass $t\bar{t}$ resonances is the topcolor assisted
₁₁₈₀ technicolor model (TC2), which predicts the existence of a leptophobic Z' boson. The
₁₁₈₁ resultant top quark pair provides a well understood probe to search for such hypothetical
₁₁₈₂ particles.

₁₁₈₃ The Z' could potentially have a mass on the order of several TeV. As a result their
₁₁₈₄ decay product would be produced in the detector with very large momentum. These
₁₁₈₅ top quarks are said to be boosted. In terms of the subsequent top decay, the resultant
₁₁₈₆ bottom quark and W boson are expected to emerge in a collimated cone. The events
₁₁₈₇ thus appear as two large back-to-back jets. If the W decays leptonically, the W lepton
₁₁₈₈ is expected to lie very close to or within the b -jet. If the W decays hadronically all three
₁₁₈₉ jets will appear to merge into a single *fat* jet.

₁₁₉₀ In this chapter the results of a feasibility study conducted to determine the viability
₁₁₉₁ of using the χ^2_{match} tagger to tag W muons from boosted top-quark decays is presented
₁₁₉₂ and discussed. Note that this is in contrast to the cross-section analysis detailed in a
₁₁₉₃ previous chapter where the muon tagged came from the semileptonic decay of b -quarks.

1194 The boost is expected to be related to the mass of the Z' produced, so a higher mass Z'
1195 would decay into more collimated jets. The environment that results is thus very similar
1196 to that of a semileptonic b -decay, a muon buried inside of a b -jet.

1197 No evidence for such a resonance has been observed and limits have been placed on
1198 the production rate of these resonance for various benchmark models. A leptophobic
1199 topcolor Z' of mass less than 1.74 TeV has been excluded using 4.7 fb^{-1} of pp collision
1200 data collected by ATLAS with a center-of-mass energy $\sqrt{s} = 7 \text{ TeV}$ [28]. Additionally a
1201 more recent analysis using 14.3 fb^{-1} of $\sqrt{s} = 8 \text{ TeV}$ data collected at ATLAS excluded
1202 a Z' with a mass less than 1.8 TeV at 95% confidence level [29]. The analysis detailed
1203 here is based on the 7 TeV analysis. Similar analyses performed with data collected by
1204 CMS have excluded Z' candidates for similar benchmark models [30–32].

1205 The performance of SMT is compared to the contemporary method for selecting
1206 muons known as mini-isolation. In addition a short performance study to determine the
1207 viability of using SMT to tag b -jets in boosted top events is also presented. Firstly, a
1208 short examination of the topology of a boosted event is presented.

1209 7.1 Data samples

1210 This measurement is based on simulated data generated for a Z' with a mass of 1.0,
1211 1.3, 1.6, 2.0, 2.5 and 3.0 TeV. All Monte Carlo (MC) samples were generated using
1212 PYTHIA [?] with CTEQ6LI [?] PDFs¹. The width of the generated Z' is 3% of the
1213 mass.

1214 The analysis is based on the underlying event information created by the simulation
1215 software. This includes the kinematic information of particles in the event as well as
1216 the child-parent connection between particles. For example the Z' has two daughter
1217 particles associated with it, the top and antitop. The decay chain continues with the W
1218 bosons and b quarks. By navigating up or down this chain it is possible to ascertain the
1219 origin of a given particle. The truth information represents the state of various particles
1220 without the effects of the detector, that is the p_T of a given truth particle is not affected
1221 by detector resolution for example.

¹Parton Distribution Function which describes the relative density of gluon and quarks in the colliding hadrons.

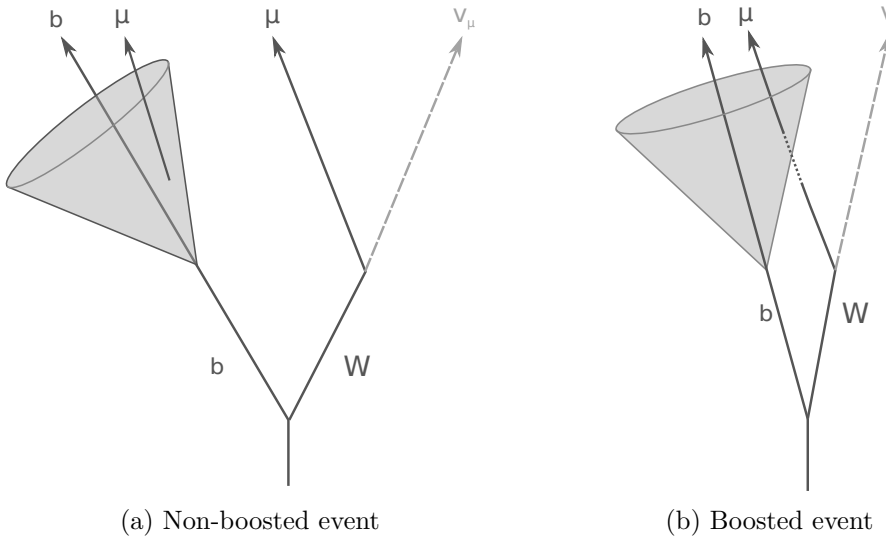


Figure 7.1: This figure shows a simple diagram for the possible configuration of final-state objects in a (a) boosted and (b) non-boosted events. Note that in both cases a muon is embedded within the b -jet

1222 7.2 Boosted event topology

1223 In order to perform an effective feasibility study, it is important to understand the
1224 signature left by boosted events in the detector. There are certain expectations regarding
1225 the momentum distribution of the various product particles from the decay of the top
1226 as well as their angular separation. As with the cross-section analysis presented in
1227 Chapter ??, this study focuses on the semileptonic decays of top quark pairs.

1228 It is expected for events where the momentum of the top quarks higher to exhibit
1229 stronger collimation between the W muon and the b -quark. This results in a situation
1230 very similar to that exploited for muon tagging in Section ?? where a muon from the
1231 semileptonic decay of a b -quark emerges from within the b -jet. Figure 7.1 illustrates the
1232 similarity of both scenarios. It is thus possible to use the χ^2_{match} -tagger² to tag W muons
1233 in boosted events. As the tagger is designed to work in energetically “busy” sectors of
1234 the detector, it is ideally suited to probe highly boosted events where the decay products
1235 are collimated.

2As signal muons are very hard, the tagger is now referred to as the χ^2_{match} -tagger not soft muon tagger to reflect this difference

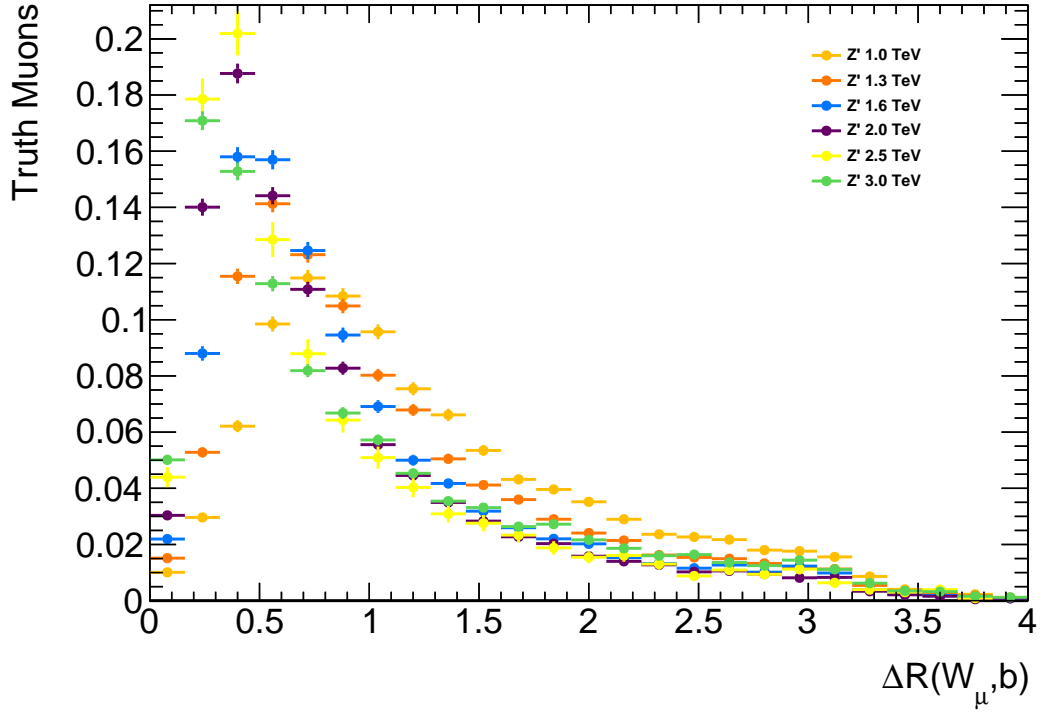


Figure 7.2: The angular separation (ΔR) between the truth W muon and the corresponding b -quark for all examined Z' mass points.

As can be seen from Figure 7.2 the increase in boost does result in the W muon and b -quark emerging closer. Note that the fraction of events below the SMT requirement of $\Delta R(\mu, jet) < 0.5$ increases with increased top-quark p_T . Additionally Figure 7.3 shows that the top p_T distribution peaks at just below half of the mass of the Z' boson, thus the large portion of the candidate muons in the sample will pass the aforementioned separation requirement. The decay products of the top quark appear to emerge primarily back to back as seen in Figure 7.4. c..

7.3 Signal muon selection

7.3.1 Muon selection

The nominal muon object selection includes an isolation requirement, which normally removes events where the signal lepton is found in a region of the calorimeter with large amounts of activity. Cutting on the amount of energy deposited in the calorimeter

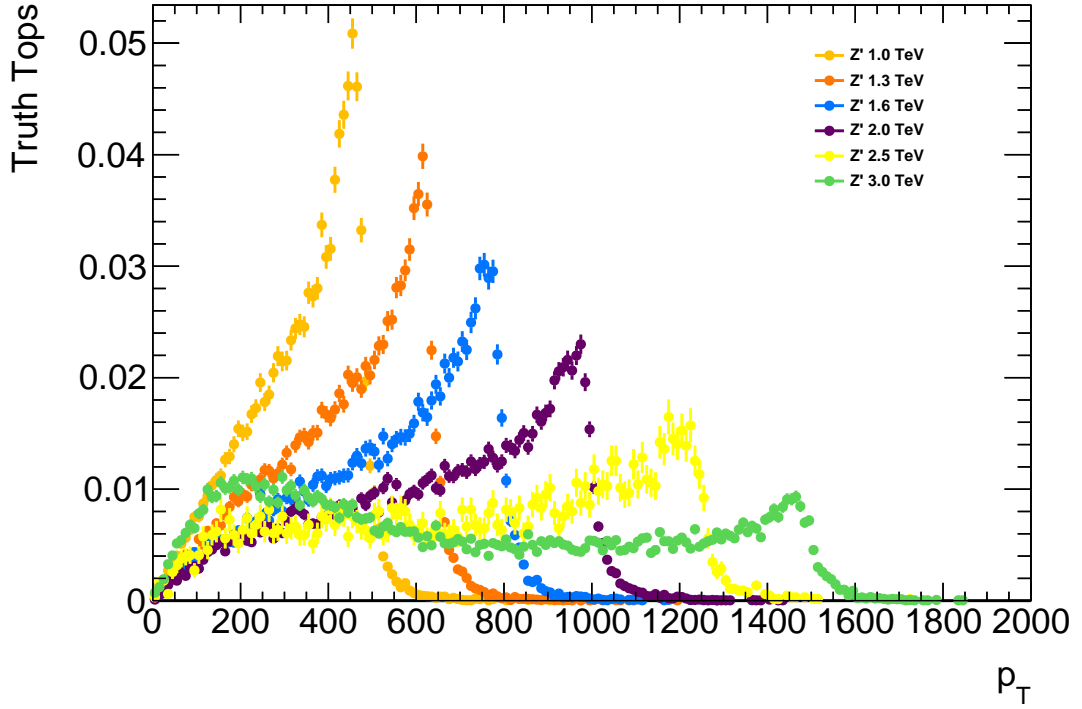


Figure 7.3: The transverse momentum of the top/anti-top quarks in the event for all examined Z' mass points.

1248 around the lepton is an example of one such requirement. Such a cut forms part of the
 1249 object selection used in the top cross-section measurement described in Part 5.

1250 However, as described a priori, boosted top events result in large collimated jets
 1251 which include the products of the two top quarks. Thus the signal lepton can emerge
 1252 within the cone of the reconstructed jet from the b -quark.

1253 Note that the muon is not required to be isolated, instead the muon is tagged by the
 1254 χ^2_{match} tagger. Selecting isolated muons would reduce significantly the number of muons
 1255 available for tagging. Additionally, as explained a priori, events which exhibit stronger
 1256 collimation are more likely to emerge from particles with higher masses. By requesting
 1257 the muons be isolated, the ability to probe those higher mass events is diminished.

1258 Another candidate to replace the traditional isolation selection is the so-called mini-
 1259 isolation. This variable takes into account the strong collimation of the top products
 1260 with increasing boost. Mini-isolation is defined as the sum of the measured transverse
 1261 momenta of all tracks in a cone of size of size $\Delta R = k_T/p_T^\ell$ around the lepton, where

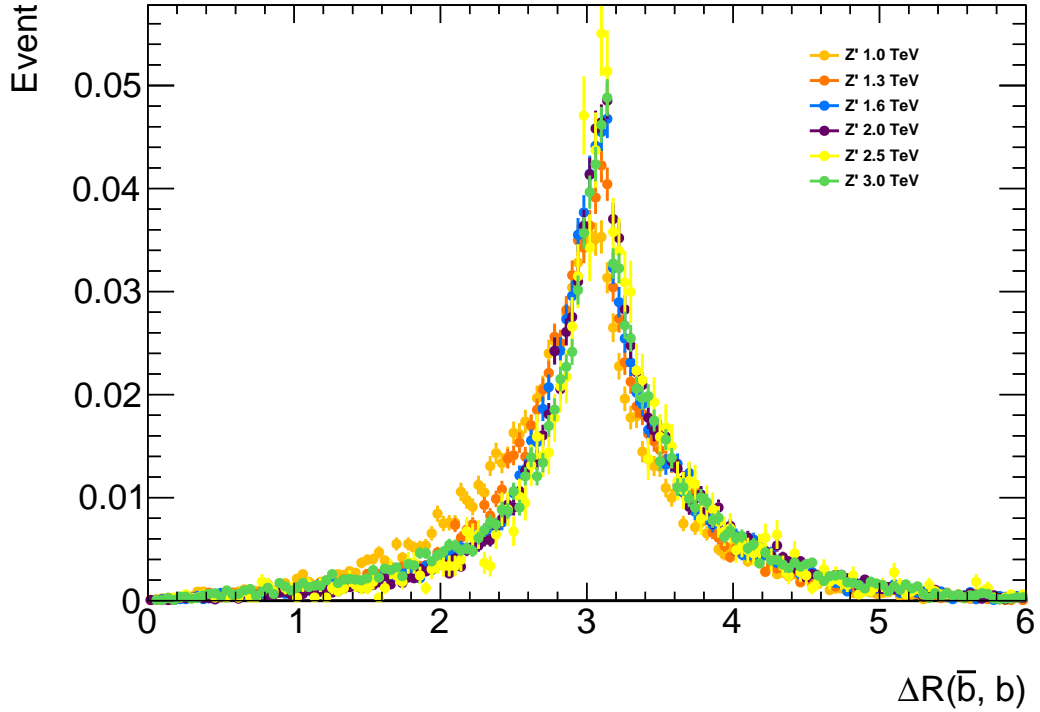


Figure 7.4: The angular separation (ΔR) between the b and \bar{b} in the event for all examined Z' mass points.

1262 k_T is an adjustable scale and p_T^ℓ is the momentum of the lepton in question. This is
1263 known as the absolute mini-isolation. This study uses the relative mini-isolation where
1264 the absolute value is scaled by the momentum of the lepton (MI/p_T^ℓ).

1265 In this analysis the performance of the χ^2_{match} tagger is measured against mini-
1266 isolation using a $k_T = 10$ and a lepton is deemed isolated if the p_T in the MI cone
1267 is less than 5% that of the lepton. The Muon Tagger operates with the same selection
1268 as used in Part 5, the cuts are $|z_0| < 3.0$ mm, $|d_0| < 3.0$ mm and finally $\chi^2_{\text{DoF}} < 3.2$.

1269 Thus two separate selections are applied, one for mini-isolation and one for SMT.
1270 Note that both methodologies have different muon reconstruction criteria, these are
1271 detailed in Table 7.1.

1272 The performance of both methodologies are then compared by measuring their effi-
1273 ciency.

Table 7.1: Muon reconstruction selection used by Mini-Isolation and by Muon Tagging

Mini-Isolation	Muon-Tagging
MCP Cuts	
$p_T > 20 \text{ GeV}$	
$ \eta < 2.5$	
MUID	STACO
$z_0 < 3.0 \text{ mm}$	Is Combined Muon
IsEM Tight	

1274 7.4 Efficiency definition

1275 The efficiency measurement was designed to provide an accurate representation of the
 1276 performance of the soft muon tagger and a valid comparison with mini-isolation. Ad-
 1277 ditional sources of inefficiency such as muon reconstruction are separated out into an
 1278 additional efficiency which is also quoted. See Figure 7.7 for a summary of the efficiency
 1279 measurement.

1280 Firstly, events where a W decays into a muon are selected, this becomes the pool
 1281 of events from which the efficiency is measured. The selections then diverge and the
 1282 two sets of reconstruction cuts described in Table 7.1 are applied independently. The
 1283 efficiency of each sets of reconstruction cuts are measured as:

$$\epsilon_{\text{reco}} = \frac{\text{Muons which pass selection}}{\text{All reconstructed muons}}$$

1284 These good reconstructed muons are then truth-matched to the truth μ from the
 1285 W if the angular separate (ΔR) between them is less than 0.01. This has an efficiency
 1286 associated with it, defined as:

$$\epsilon_{\text{match}} = \frac{\text{Muons matched to truth } W \text{ muon}}{\text{Muons which pass selection}}$$

1287 Note that at each stage the denominator is the numerator of the previous efficiency.
 1288 This allows for a combination of all the efficiencies to obtain an inclusive measure which
 1289 can used to approximate the number of W muons which would be selected from collision
 1290 data assuming that the simulation describes the data well.

1291 Next the muons are required to be within $\Delta R < 0.5$ from a jet. The Muon Tagger

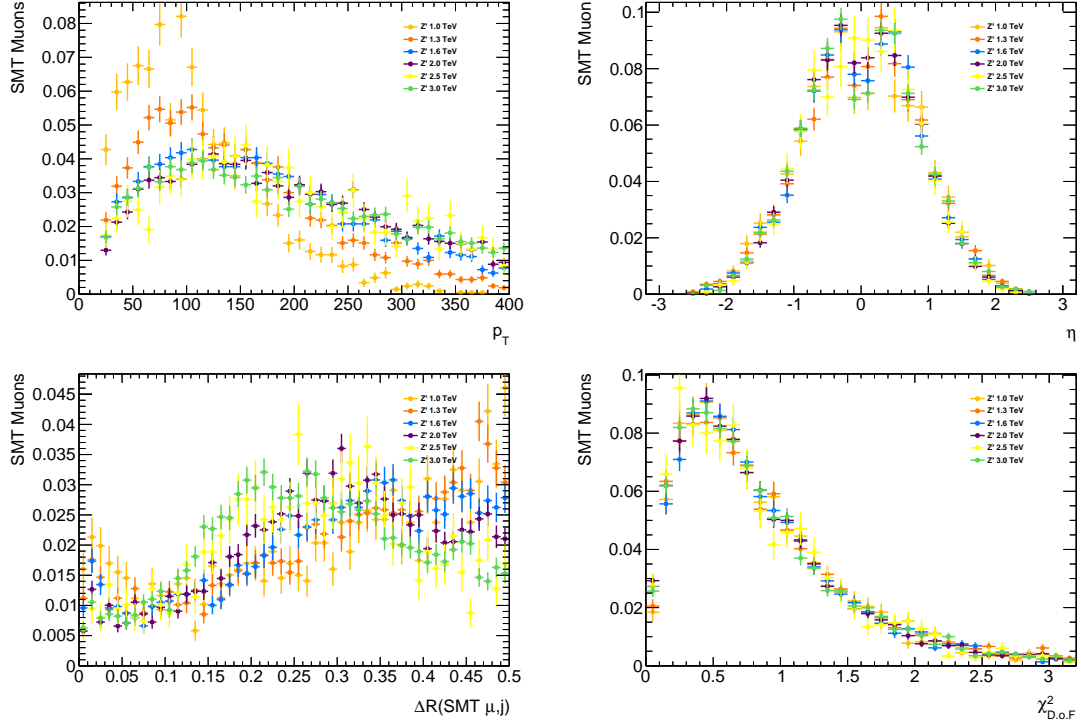


Figure 7.5: This figure shows the distribution of (a) transverse momentum and (b) pseudo-rapidity of muons which pass the SMT selection, the (c) angular separation between those muons and the nearest jet in the event and (d) the χ^2_{match} used in the selection for all tested Z' mass points.

1292 requires that jets be near a jet, in addition the impetus behind the analysis is to probe
 1293 highly boosted events exploiting the capabilities of χ^2_{match} tagging. This selection ensures
 1294 that the muons available for χ^2_{match} tagging are indeed close to a jet. This selection also
 1295 has an efficiency associated with it defined as:

$$\epsilon_{\text{non-iso}} = \frac{\text{Muons with } \Delta R(\mu, \text{jet}) < 0.5}{\text{Muons matched to truth } W \text{ muon}}$$

1296 The final step is the application of both the mini-isolation selection and the muon
 1297 tagging selection discussed a priori. These selections are associated with the final and
 1298 most interesting sets of efficiencies, defined as:

$$\epsilon_{\text{MT/MI10}} = \frac{\text{Muons which pass MT/MI10 selection}}{\text{Muons with } \Delta R(\mu, \text{jet}) < 0.5}$$

1299 Please note that the denominator in every efficiency is a subset of the previous

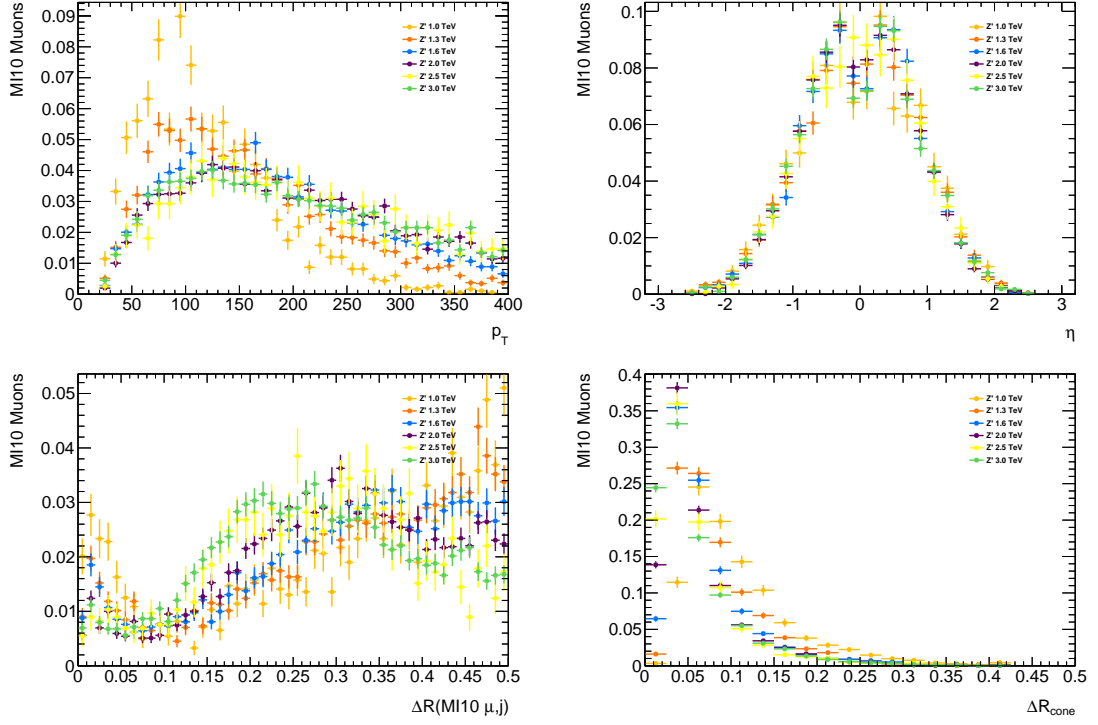


Figure 7.6: This figure shows the (a) transverse momentum and (b) pseudo-rapidity of muons which pass the MI10 selection, the (c) angular separation between those muons and the nearest jet in the event and (d) the cone size used in the selection for all tested Z' mass points.

denominator. In other words each selection is applied in sequence and the efficiencies are calculated out of the remaining muons which passed the previous selection criteria.

Note that in the nominal analysis described in [28] muons which are within ΔR of 0.1 of the jet would be removed. The impetus behind the analysis is to exploit the χ^2_{match} tagger to accept additional events where the signal muon emerges very close to the jet axis, thus overlap removal is not part of the χ^2_{match} tagging selection. In order to provide an accurate performance comparison between the χ^2_{match} tagger and mini-isolation, the overlap removal is applied only for the mini-isolation selection at the end of the chain. The additional acceptance gained by using χ^2_{match} tagger is compared to the mini-isolation selection with overlap included:

$$\epsilon = \frac{\text{Muons that pass } \chi^2_{\text{match}} \text{ tagger} - \text{MI muons } \Delta R < 0.1}{\text{Total } W \mu} \quad (7.1)$$

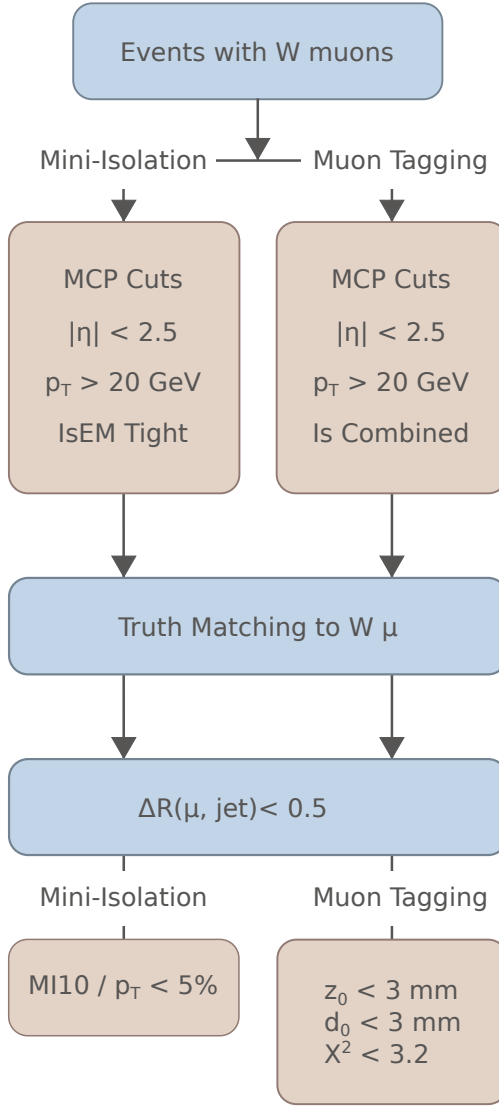


Figure 7.7: Structure of the efficiency measurement.

1310 7.5 Results

1311 Mini-isolation is a very efficient method for selecting muons. Table 7.2 shows the effi-
1312 ciency for the χ_{match}^2 tagger, mini-isolation and mini-isolation including overlap removal.
1313 Across the used mass range, the efficiency of selection remains above 80% and in fact
1314 increases with a increased Z' mass. When the Z' has a mass of 3 TeV the efficiency of
1315 selection with mini-isolation is 92.5% with no overlap removal. In contrast the efficiency
1316 of the χ_{match}^2 tagger is more consistent across the used mass range and higher than mini-
1317 isolation for a given mass. For a Z' with a mass of 3 TeV the measured efficiency of

Z' Mass [TeV]	χ^2_{match}	MI10	MI10 + Overlap
1.0	94.9%	83.1%	67.0%
1.3	95.8%	89.0%	79.2%
1.6	95.9%	90.4%	81.9%
2.0	96.0%	92.4%	85.7%
2.5	95.8%	92.8%	85.1%
3.0	96.2%	92.5%	85.0%

Table 7.2: Efficiency of selecting a muon by using the χ^2_{match} tagger against mini-isolation. Note that ‘MI10 + Overlap’ is the efficiency of applying both the mini-isolation cut and overlap removal.

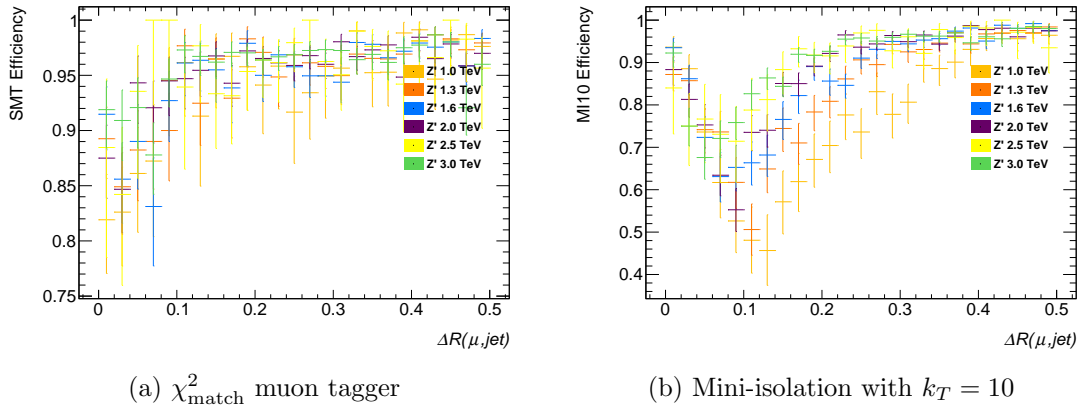


Figure 7.8: Efficiency of mini-isolation ($k_T = 10$) and χ^2_{match} muon tagger as a function of the angular separation between the reconstructed muon and the nearest reconstructed jet. Note the dip in the mini-isolation efficiency at low ΔR . In the nominal analysis an overlap removal between the jet and the muon is applied.

the χ^2_{match} tagger is 96.2%. When applying the overlap removal the efficiency of mini-isolation falls to 85.0%. As can be seen from Figure 7.8 the efficiency of mini-isolation dips for muons which are close to a jet however this occurs below the threshold of the overlap removal. Finally the additional acceptance gained as defined in 7.1 is 4.03%. The additional acceptance gained in all mass points is also included in Table 7.2.

7.5.1 Background

A preliminary examination of the amount of background was performed. This was done on the same sample of events but instead of selecting semileptonic events, the all-hadronic events are used as background. While these events do not perfectly mimic the true background, namely $b\bar{b}$, the lack of any real signal muons can provide a suitable

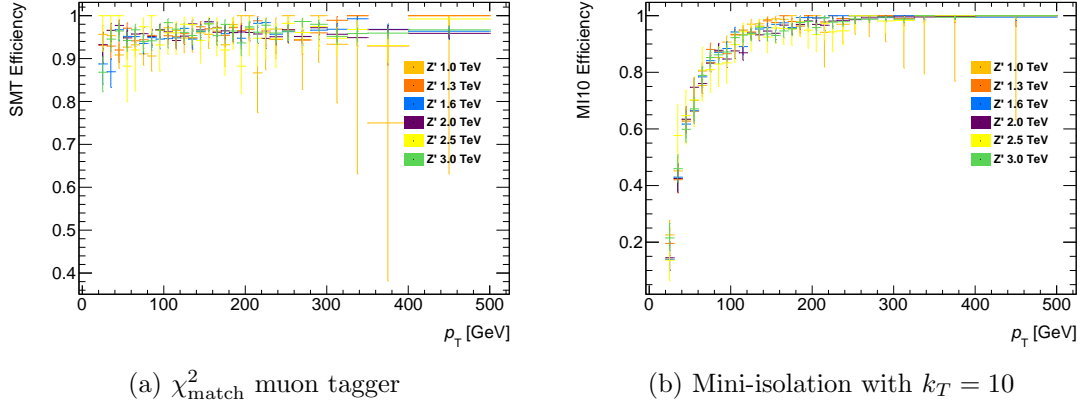


Figure 7.9: Efficiency of mini-isolation ($k_T = 10$) and χ^2_{match} muon tagger as a function of the transverse momentum of the muon.

1328 preliminary substitute.

1329 The lack of an isolation requirement is expected to result in a substantial increase
1330 in the amount of background selected. Additionally the semileptonic b -decays in $b\bar{b}$
1331 would result in muons that the χ^2_{match} tagger will select. The analysis chain described
1332 in Section 7.4 is repeated on the same sample used a priori however the truth level
1333 selection of events with a W muon is reversed, thus at truth level both W bosons decay
1334 hadronically.

1335 The results of this selection are presented in Table 7.3. As expected mini-isolation re-
1336 moves a substaintial amount of background while maintaining very high signal efficiency.
1337 In comparison, removing the isolation requirement greatly increases the background ac-
1338 ceptance when using the χ^2_{match} tagger. A full treatment of the background would be
1339 required to account for the background present.

1340 The increase in signal acceptance does not make this methodology sufficiently advan-
1341 tageous particularly when considering the large increase in fake rate. An examination
1342 of the b -tagging potential of the χ^2_{match} tagger is presented in the next section.

1343 7.6 B-tagging potential in boosted events

1344 As with the non-boosted $t\bar{t}$ analysis, b -tagging is used to select boosted $t\bar{t}$ events. By
1345 following a similar methodology a sample of muons which likely come from the semilep-
1346 tonic decay of b quarks was constructed. This pool of muons was then used to estimate

Table 7.3: Fake rate of χ^2_{match} tagger, mini-isolation and mini-isolation including overlap removal as measured using all Z' mass points.

Z' Mass [TeV]	χ^2_{match}	MI10	MI10 + Overlap
1.0	92.8%	4.10%	2.39%
1.3	92.4%	4.77%	3.66%
1.6	91.8%	5.46%	4.55%
2.0	91.1%	7.07%	6.09%
2.5	90.0%	6.40%	5.57%
3.0	90.1%	6.59%	5.68%

¹³⁴⁷ the efficiency of the χ^2_{match} tagger in selecting this soft muon.

¹³⁴⁸ The analysis chain is designed to compensate for the lack of hadron truth information
¹³⁴⁹ and the necessary navigation information³ to correctly select the truth muon from $b \rightarrow \mu$
¹³⁵⁰ or $b \rightarrow c \rightarrow \mu$.

¹³⁵¹ Firstly jets are matched to the truth b-quarks in the event. The matching is done
¹³⁵² by a simple ΔR requirement of 0.3. These jets are likely emerging from the b -quark.

Next the requirement that the muon be not isolated is applied. The nearest STACO muon within a $\Delta R=0.5$ is selected as the possible soft muon candidate. Finally the SMT selection is applied and the efficiency of this selection is defined as

$$\epsilon_{SMT} = \frac{\text{Number of muons that pass the SMT selection}}{\text{Number of muons within } \Delta R(\mu, j) < 0.5}$$

¹³⁵³ The efficiency of χ^2_{match} -tagger appears to decrease by 2% across the Z' mass range as
¹³⁵⁴ can be seen from Table 7.4. Despite this small decrease in efficiency, the overall selection
¹³⁵⁵ is very efficient across the range. Note that the relative number of muons closer to the
¹³⁵⁶ jet increases with increasing Z' mass.

³The relationship between parent and child particles

Table 7.4: Summary of the number of muons remaining after each selection cut and the efficiency.

Z' Mass [TeV]	CB Muons	Good Muons	$\Delta R(\mu, jet) < 0.5$	χ^2_{match} -tagged
1.0	74551	25011 (33.5%)	10061 (40.2%)	9472 (94.2%)
1.3	92983	30452 (32.8%)	14995 (49.2%)	14083 (93.9%)
1.6	88722	28041 (31.6%)	15677 (55.9%)	14696 (93.7%)
2.0	108924	32252 (29.6%)	19951 (61.9%)	18572 (93.1%)
2.5	25696	7063 (27.5%)	4580 (64.8%)	4252 (92.8%)
3.0	113702	30959 (27.2%)	19240 (62.1%)	17832 (92.7%)

1357 Chapter 8

1358 Conclusions

Appendices

1359

1360 **Appendix A**

1361 **List of triggers used in calibration**

1362 The calibration analysis makes use of an OR of the triggers listed below. The triggers fire
1363 based on a set of criteria summarized in the trigger name following the ATLAS trigger
1364 naming convention. The list includes generic single low- p_T muon triggers such as `EF_mu6`
1365 and `EF_mu15`, single high- p_T muons & jets triggers such as `EF_mu24_j65_a4tchad` and
1366 the specialized J/ψ trigger `EF_mu6_Trk_Jpsi_loose`.

- 1367 ● `EF_mu24_j65_a4tchad_EFxe40_tclcw`
- 1368 ● `EF_mu4T_j65_a4tchad_xe60_tclcw_loose`
- 1369 ● `EF_mu24_j65_a4tchad`
- 1370 ● `EF_mu18_tight_e7_medium1`
- 1371 ● `EF_mu4T_j65_a4tchad_xe70_tclcw_veryloose`
- 1372 ● `EF_mu24_j65_a4tchad_EFxe60_tclcw`
- 1373 ● `EF_mu24_tight_b35_mediumEF_j35_a4tchad`
- 1374 ● `EF_mu20i_tight_g5_loose_TauMass`
- 1375 ● `EF_mu6_Trk_Jpsi_loose`
- 1376 ● `EF_mu24i_tight`
- 1377 ● `EF_mu24i_tight_MuonEF`

- 1378 ● EF_mu24i_tight_MG
- 1379 ● EF_mu24i_tight_l2muonSA
- 1380 ● EF_mu24_tight_3j35_a4tchad
- 1381 ● EF_mu24_g20vh_loose
- 1382 ● EF_mu40_MSonly_barrel_tight
- 1383 ● EF_mu50_MSonly_barrel_tight
- 1384 ● EF_mu24_tight_EFxe40
- 1385 ● EF_mu24_tight_L2StarB
- 1386 ● EF_mu18_medium
- 1387 ● EF_mu24_medium
- 1388 ● EF_mu24_tight
- 1389 ● EF_mu24_tight_MuonEF
- 1390 ● EF_mu24_tight_MG
- 1391 ● EF_mu24_tight_L2StarC
- 1392 ● EF_mu36_tight
- 1393 ● EF_mu40_tight
- 1394 ● EF_mu20it_tight
- 1395 ● EF_mu24_g20vh_medium
- 1396 ● EF_mu18_2g10_medium
- 1397 ● EF_mu24_muCombTag_NoEF_tight
- 1398 ● EF_mu10i_loose_g12Tvh_medium
- 1399 ● EF_mu10i_loose_g12Tvh_medium_TauMass

- 1400 ● EF_mu18_2g10_loose
- 1401 ● EF_mu10i_g10_medium_TauMass
- 1402 ● EF_mu20i_tight_g5_medium_TauMass
- 1403 ● EF_mu24_tight_3j45_a4tchad
- 1404 ● EF_mu24_tight_4j45_a4tchad
- 1405 ● EF_mu24_tight_4j35_a4tchad
- 1406 ● EF_mu4T
- 1407 ● EF_mu6
- 1408 ● EF_mu15
- 1409 ● EF_mu40_slow_tight
- 1410 ● EF_mu60_slow_tight1
- 1411 ● EF_mu22_IDTrkNoCut_tight
- 1412 ● EF_mu8_4j45_a4tchad_L2FS
- 1413 ● EF_mu6_Trk_Jpsi_loose_L2StarB
- 1414 ● EF_mu6_Trk_Jpsi_loose_L2StarA
- 1415 ● EF_mu24_j65_a4tchad_EFx40wMu_tclcw
- 1416 ● EF_mu24_j65_a4tchad_EFx60wMu_tclcw
- 1417 ● EF_mu6T_2b55_medium_2j55_a4tchad_L1J20_matched
- 1418 ● EF_mu24i_tight_muFast
- 1419 ● EF_mu4T_L2StarB
- 1420 ● EF_mu6_L2StarB
- 1421 ● EF_mu15_vbf_L1TAU8_MU10

¹⁴²² **Appendix B**

¹⁴²³ **List of combined muon
performance (MCP) cuts**

¹⁴²⁵ Bibliography

- ¹⁴²⁶ [1] J. Beringer et al. (Particle Data Group). The Review of Particle Physics. *Physical Review D*, 86:010001+, 2012.
- ¹⁴²⁷
- ¹⁴²⁸ [2] Nikolaos Kidonakis. NNLL threshold resummation for top-pair and single-top production. 2012.
- ¹⁴²⁹
- ¹⁴³⁰ [3] Micha Czakon, Paul Fiedler, and Alexander Mitov. Total top-quark pair-production cross section at hadron colliders through $O(\frac{4}{S})$. *Phys.Rev.Lett.*, 110(25):252004, 2013.
- ¹⁴³¹
- ¹⁴³²
- ¹⁴³³ [4] B. Odom, D. Hanneke, B. D'Urso, and G. Gabrielse. New measurement of the electron magnetic moment using a one-electron quantum cyclotron. *Phys. Rev. Lett.*, 97:030801, Jul 2006.
- ¹⁴³⁴
- ¹⁴³⁵
- ¹⁴³⁶ [5] et. al. G. Aad. Observation of a new particle in the search for the standard model higgs boson with the {ATLAS} detector at the {LHC}. *Physics Letters B*, 716(1):1 – 29, 2012.
- ¹⁴³⁷
- ¹⁴³⁸
- ¹⁴³⁹ [6] Serguei Chatrchyan et al. Observation of a new boson at a mass of 125 GeV with the CMS experiment at the LHC. *Phys.Lett.*, B716:30–61, 2012.
- ¹⁴⁴⁰
- ¹⁴⁴¹ [7] D.H. Perkins. *Introduction to High Energy Physics*. Cambridge University Press, 2000.
- ¹⁴⁴²
- ¹⁴⁴³ [8] D. Griffiths. *Introcution to Elementary Particles*. "John Wiley & Sons, Inc", 1987.
- ¹⁴⁴⁴
- ¹⁴⁴⁵ [9] Nicola Cabibbo. Unitary symmetry and leptonic decays. *Phys. Rev. Lett.*, 10:531–533, Jun 1963.

- ¹⁴⁴⁶ [10] Makoto Kobayashi and Toshihide Maskawa. Cp-violation in the renormalizable
¹⁴⁴⁷ theory of weak interaction. *Progress of Theoretical Physics*, 49(2):652–657, 1973.
- ¹⁴⁴⁸ [11] Lincoln Wolfenstein. Parametrization of the kobayashi-maskawa matrix. *Phys. Rev.
¹⁴⁴⁹ Lett.*, 51:1945–1947, Nov 1983.
- ¹⁴⁵⁰ [12] S. W. Herb, D. C. Hom, L. M. Lederman, J. C. Sens, H. D. Snyder, J. K. Yoh, J. A.
¹⁴⁵¹ Appel, B. C. Brown, C. N. Brown, W. R. Innes, K. Ueno, T. Yamanouchi, A. S. Ito,
¹⁴⁵² H. Jöstlein, D. M. Kaplan, and R. D. Kephart. Observation of a dimuon resonance
¹⁴⁵³ at 9.5 gev in 400-gev proton-nucleus collisions. *Phys. Rev. Lett.*, 39:252–255, Aug
¹⁴⁵⁴ 1977.
- ¹⁴⁵⁵ [13] CDF Collaboration. Observation of top quark production in $p\bar{p}$ collisions with the
¹⁴⁵⁶ collider detector at Fermilab. *Phys. Rev. Lett.*, 74:2626–2631, Apr 1995.
- ¹⁴⁵⁷ [14] D0 Collaboration. Search for high mass top quark production in $p\bar{p}$ collisions at
¹⁴⁵⁸ $\sqrt{s}=1.8$ tev. *Phys. Rev. Lett.*, 74:2422–2426, Mar 1995.
- ¹⁴⁵⁹ [15] The ATLAS Collaboration. Search for top pair candidate events in ATLAS at $\sqrt{s}=7$
¹⁴⁶⁰ TeV. Technical Report ATLAS-CONF-2010-063, CERN, Geneva, Jul 2010.
- ¹⁴⁶¹ [16] Selection of top-like events in the dilepton and lepton-plus-Jets channels in early 7
¹⁴⁶² TeV Data. Technical Report CMS-PAS-TOP-10-004, CERN, 2010. Geneva, 2010.
- ¹⁴⁶³ [17] Johann H. Kuhn, A. Reiter, and Peter M. Zerwas. Z Decays to Top Quarks.
¹⁴⁶⁴ *Nucl.Phys.*, B272:560, 1986.
- ¹⁴⁶⁵ [18] M. Aliev, H. Lacker, U. Langenfeld, S. Moch, P. Uwer, et al. HATHOR: HAdronic
¹⁴⁶⁶ Top and Heavy quarks crOss section calculatoR. *Comput.Phys.Commun.*, 182:1034–
¹⁴⁶⁷ 1046, 2011.
- ¹⁴⁶⁸ [19] O.W. Greenberg. Cpt violation implies violation of lorentz invariance.
¹⁴⁶⁹ *Phys.Rev.Lett.*, 89:231602, 2002.
- ¹⁴⁷⁰ [20] Georges Aad et al. Measurement of the mass difference between top and anti-top
¹⁴⁷¹ quarks in pp collisions at $\sqrt(s) = 7$ TeV using the ATLAS detector. *Phys.Lett.*,
¹⁴⁷² B728:363–379, 2014.

- ¹⁴⁷³ [21] Serguei Chatrchyan et al. Measurement of the mass difference between top and
¹⁴⁷⁴ antitop quarks. *JHEP*, 1206:109, 2012.
- ¹⁴⁷⁵ [22] Georges Aad et al. Measurement of the top quark pair production charge asymmetry
¹⁴⁷⁶ in proton-proton collisions at $\sqrt{s} = 7$ TeV using the ATLAS detector. *JHEP*,
¹⁴⁷⁷ 1402:107, 2014.
- ¹⁴⁷⁸ [23] Serguei Chatrchyan et al. Measurements of the $t\bar{t}$ charge asymmetry using the
¹⁴⁷⁹ dilepton decay channel in pp collisions at $\sqrt{s} = 7$ TeV. 2014.
- ¹⁴⁸⁰ [24] Lyndon Evans and Philip Bryant. LHC machine. *Journal of Instrumentation*,
¹⁴⁸¹ 3(08):S08001, 2008.
- ¹⁴⁸² [25] The ATLAS Collaboration. Luminosity determination in pp collisions at $\text{sqrt}(s)=7$
¹⁴⁸³ tev using the atlas detector at the lhc. *The European Physical Journal C*, 71(4),
¹⁴⁸⁴ 2011.
- ¹⁴⁸⁵ [26] The ATLAS Collaboration. The ATLAS experiment at the CERN Large Hadron
¹⁴⁸⁶ Collider. *Journal of Instrumentation*, 3(08):S08003, 2008.
- ¹⁴⁸⁷ [27] *ATLAS detector and physics performance: Technical Design Report, 1.* Technical
¹⁴⁸⁸ Design Report ATLAS. CERN, Geneva, 1999.
- ¹⁴⁸⁹ [28] Georges Aad et al. Search for $t\bar{t}$ resonances in the lepton plus jets final state with
¹⁴⁹⁰ ATLAS using 4.7 fb^{-1} of pp collisions at $\sqrt{s} = 7$ TeV. *Phys.Rev.*, D88(1):012004,
¹⁴⁹¹ 2013.
- ¹⁴⁹² [29] A search for $t\bar{t}$ resonances in the lepton plus jets final state with ATLAS using
¹⁴⁹³ 14 fb^{-1} of pp collisions at $\sqrt{s} = 8$ TeV. Technical Report ATLAS-CONF-2013-052,
¹⁴⁹⁴ CERN, Geneva, May 2013. Not published in the proceedings.
- ¹⁴⁹⁵ [30] Serguei Chatrchyan et al. Search for Z' resonances decaying to $t\bar{t}$ in dilepton+jets
¹⁴⁹⁶ final states in pp collisions at $\sqrt{s} = 7$ TeV. *Phys.Rev.*, D87:072002, 2013.
- ¹⁴⁹⁷ [31] Serguei Chatrchyan et al. Search for anomalous $t\bar{t}$ production in the highly-boosted
¹⁴⁹⁸ all-hadronic final state. *JHEP*, 1209:029, 2012.

- ¹⁴⁹⁹ [32] The CMS Collaboration. Search for $t\bar{t}$ resonances in semileptonic final state. Technical Report CMS-PAS-B2G-12-006, CERN, Geneva, 2013.
- ¹⁵⁰⁰